INTERNATIONAL UNIVERSITY LIAISON INDONESIA

BACHELOR'S THESIS

NUMERICAL INVESTIGATION OF MOMENTS OF INERTIA'S UNCERTAINTY EFFECTS ON LAPAN RX-200C ROCKET

By

Faisal Tri Mulyawan

11201701014

Presented to the Faculty of Engineering and Life Sciences
In Partial Fulfilment Of the Requirements for the Degree of

SARJANA TEKNIK
In
AVIATION ENGINEERING

FACULTY OF ENGINEERING AND LIFE SCIENCES

BSD City 15345
Indonesia
January 2022

APPROVAL PAGE

NUMERICAL INVESTIGATION OF MOMENTS OF INERTIA'S UNCERTAINTY EFFECTS ON LAPAN RX-200C ROCKET

FAISAL TRI MULYAWAN
11201701014
Presented to the Faculty of Engineering
In Partial Fulfillment of the Requirements for the Degree of

SARJANA TEKNIK
In
AVIATION ENGINEERING

FACULTY OF ENGINEERING AND LIFE SCIENCES

Triwanto Simanjuntak, PhD	______
Thesis Advisor	Date
Dipl.-Ing. Sentot Wahjoe Goeritno, MSi	______
Dean of Faculty of Engineering and Life Sciences	Date

EXAMINERS APPROVAL PAGE

Dr. Eng. Ressa Octavianty	____________________
Examiner 1	Date
Dr. Erie Sandhita	____________________
Examiner 2	Date
Setyo U. Soekarsono, MSc.	____________________
Examiner 3	Date

STATEMENT BY THE AUTHOR

I hereby declare that this submission is my own work and to the best of my knowledge, it contains no material previously published or written by another person, nor material which to a substantial extent has been accepted for the award of any other degree or diploma at any educational institution, except where due acknowledgement is made in the thesis.

Faisal Tri Mulyawan	
Student	Date

ABSTRACT

Numerical Investigation of Moments of Inertia's Uncertainty Effects on LAPAN RX-200C Rocket

by

Faisal Tri Mulyawan

Triwanto Simanjuntak, PhD, Advisor

In this thesis the sensitivity analysis of LAPAN RX-200C rocket under moments of inertia's uncertainties (I_{xx}, I_{yy}, and I_{zz}) is investigated. The Monte Carlo method is performed to reveal patterns arising from the variations in the moments of inertia.

The dynamical modeling and simulations are done in MATLAB and Simulink while the aerodynamic coefficients are generated using DATCOM. Two types of normally distributed moments of inertia's uncertainty, constant and noise, will be considered. To isolate their individual influences, only one of moments of inertia will be exposed to uncertainty at each run. A step sidewind disturbance will also be applied to the system to induce lateral-directional motions. Nonparametric kernel density estimation and parametric normal distribution approximation will be utilized to interpret the impact point results. The stability of the rocket will also be observed briefly through its angle of attack and sideslip angle trajectories.

The results show that the moments of inertia uncertainty produce various spread characteristics with I_{xx} having the largest spread influence in the impact points relative to the rest of the moments of inertia. The results also show that I_{yy} and I_{zz} uncertainties produce similar indicators' distribution. Further, the constant-type uncertainty will create larger indicators' spread when compared to the noise-type uncertainty. The maximum indicators' spread occurs with the constant, 10% I_{xx} uncertainty and 3 m/s wind disturbance; 34 m, 123 m , and 53 m for final x, final y, and maximum altitude, respectively. Under uncertainty, the rocket is able to maintain zero angle of attack while minimizing sideslip angle in the range of -1 deg and +1 deg. Keyword: *Ballistic Rocket, Monte Carlo, Moments of Inertia*

ACKNOWLEDGEMENTS

In the completion of this thesis, I have gone through many hardships that I certainly would not be able to handle alone. I would like to express my most sincere gratitude for:

- Triwanto Simanjuntak, PhD, the one that has always been supporting and pushing me on my journey through thick and thin. No words can explain how grateful I am to be able to obtain so many valuable insights for science and, in turn, for life;
- My parents and family who have been the biggest driving force for me to push my self harder to reach for my dreams;
- Mr. Idris Eko Putro M.sc, who has provided me with countless helpful knowledge during my internship period in Pustekroket LAPAN;
- All of my friends in AVE17 who are always willing to listen to my stories and providing me with mental support;
- Last but not least, for all of the people that I am regrettably not able to mention who kept on believing in me.

Contents

List of Figures

List of Tables

Dedicated to my family and friends.

CHAPTER 1
INTRODUCTION

1.1 Background

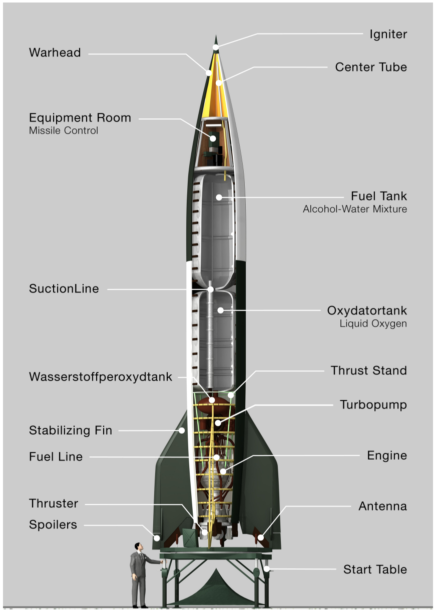

Figure 1.1: German V-2 rocket unveiled the offensive prowess of rocket technology to the world during the World War II (Marx, 2014).

The origin of rocketry can be traced back as far as the 11th century with the growing usage of gunpowder in modern-day China. The primordial rockets were mainly in the form of fireworks and fire arrows. Ever since then, humans have been trying to conceptualize and invent more advanced rockets. In this day and age, rocket technology has been enabling humanity to expand its frontier to outer space; from bringing communication satellites into orbit, deploying probes to other celestial bodies, and even sending humans to space. For the military, rocket technology has undoubtedly a great potential for both offensive and defensive ends. Fig. 1.1, shows German V-2 rocket unveiled the offensive prowess of rocket technology to the world during World War II. This was also a prototype adopted by Von Braun to develop the US space program.

FIGURE 1.2: Soyuz-FG rocket with Soyuz TMA spacecraft (Ingalls, 2006).

Recent and upcoming interest and progress of rocket developments are driven by space-related activities. One of these activities is to bring more humans out to space. NASA and SpaceX are determined to bring humans to the Moon and Mars which requires them to develop larger and more powerful rockets. Amazon's Jeff Bezos and Sir Richard Branson have recently been the first ”space tourists” with their own spacecraft. SpaceX has safely launched and brought back civilians to the Earth's orbit for around 3 days with its Falcon 9 and Dragon spacecraft.

With the growing interest in smart devices that are based on the internet of things (IoT), the demands for companies to have their own satellites have sky-rocketed. Add to that the increase of satellite technology which cut development costs while also improving reliability, the satellite market has now become a very appealing opportunity for investors.

The launch vehicle market will have to fill the increased number of launch demands. By 2027, the launch market is expected to be valued at $26 billion (Bloomberg, 2022) while the whole space industry market is projected to be valued

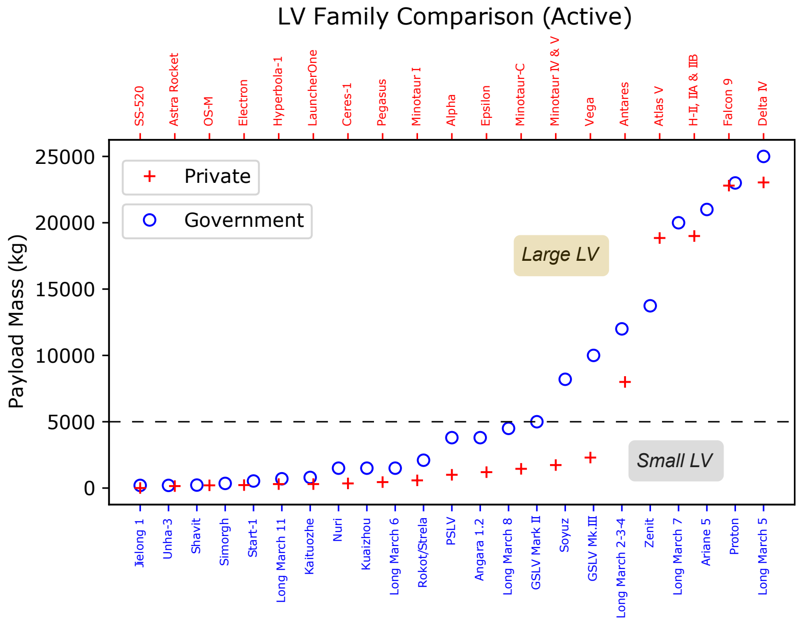

FIGURE 1.3: Comparison of active launch vehicle families (Wikipedia, 2021).

at $1 trillion by 2040 (NYTimes, 2022). Investors are racing and preparing to take their piece of the space industry market. This is reflected by the appearance of more launch vehicle start-ups. For investors, the main attractive points of these launch vehicle startups are:

- Reliability: due to improvement in rocket technology and manufacturing;
- Reusability: providing cost efficiency;
- Availability: providing flexibility to their customers.

Interestingly, these start-ups are mainly targeting the small launch vehicle market. The small launch vehicle market is especially appealing due to "Bus vs Taxi" analogy:

- Not everyone needs large rockets to put their (small) products in space;
- Some companies need their product to be launched as soon as possible;
- Hitch-riding large rockets are ill-suited for unique missions.

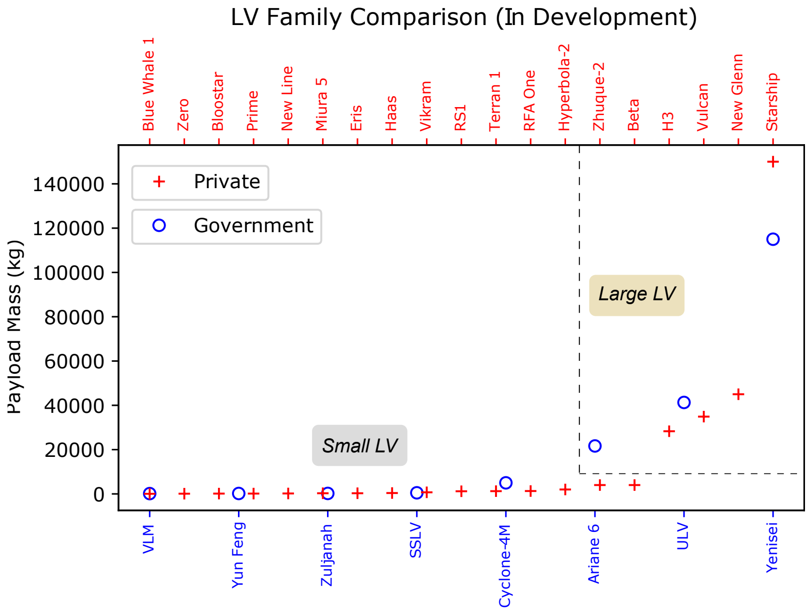

FIGURE 1.4: Comparison of launch vehicle families currently in development (*Comparison of orbital launch systems - Wikipedia*, 2022).

These companies have their own jargon in describing their rockets. Phantom Space is taking advantage of an improved supply chain and economies of scale to be a rocket "integrator" rather than a one-manufacturing-all rocket company (MITTR, 2022). Phantom space is also trying to make its own satellite design solutions. Rocket Lab has shown its capability in its reusable small launch vehicle with its Electron rocket. To improve reliability, Relativity Space is reducing the number of parts needed by 3D printing its rocket (Company, 2022).

1.2 LAPAN Rocket Program

Indonesia, through its National Institute of Aeronautics and Space (LAPAN), has been developing its own rockets as well. Rocket development by LAPAN is divided into 4 focuses (*Pusat Teknologi Roket*, 2022b):

1. EDF/TJ Rocket

FIGURE 1.5: Artist's rendition of Rocketlab's Electron booster recovery using parachute (Flight, 2019).

The main objective of the EDF/TJ Rocket program is the development and testing of experimental control systems designed by LAPAN. The rocket in interest is powered either by using an electric ducted fan (EDF) or a turbojet engine (TJ).

FIGURE 1.6: RKX-200 TJ rocket.

2. Sounding Rocket

   LAPAN sounding rocket program aims to enable atmospheric studies for Indonesian researchers. The most recent progress is the ballistic test launch of the RX-450-5 sounding rocket on 2 December 2020 in Pameungpeuk, Garut. It achieved 80 km downrange with 70-degree initial pitch. RX-450 rocket is projected to be the baseline rocket for future LAPAN guided, multi-stage sounding rocket/satellite orbiter projects.

3. Liquid-propellant Rocket

Figure 1.7: RX-450-5 rocket.

LAPAN is currently developing its own liquid-fuel rocket engine. A liquid fuel engine is advantageous to a solid fuel engine as it provides more efficiency. As opposed to its solid fuel counterpart, A liquid fuel engine's fuel flow can also be regulated which in turn enable the engineer to control the rocket's thrust. However, this also means that a liquid fuel engine introduces more complexity to the system by i.e. requiring turbomachinery and separate storage for its fuel and oxidizer.

(a) (b) (c)

Figure 1.8: LAPAN liquid fuel engines: (a)ECX1000H1; (b)ECX1000H2 (c)ECX2000H1.

4. Launch Vehicle

For its biggest plan, LAPAN is trying to build its own satellite launch vehicle by the year 2039. For this purpose, the development of a multi-stage rocket needed for an orbital flight has commenced by the development of the RX-450 rocket family. As the next step, the RX-450 rocket will be fitted with a first-stage rocket booster in addition to a stage separation capability.

FIGURE 1.9: LAPAN RPS plan.

1.3 Uncertainty Threats on Rocket Performance

With increasing demand in the launch vehicle market, so does the demand for a more accurate rocket model. In general, problems encountered by a launch vehicle can be traced down to:

- Nonlinearity;
- Model uncertainty;
- Environment uncertainty;
- Trajectory dispersions;
- Non-minimum phase systems;
- Actuator failures.

From all of the sources mentioned above, model uncertainty comes as the most physical aspect that comes with rocket manufacturing. One of the hardest properties to accurately measure is the moment of inertia of the rocket. The most straightforward way is to use computer-aided software where engineers input the geometry and mass properties of each rocket part. However, this might not take into account the imperfection in manufacturing. Small variations in one parameter could lead to large trajectory or stability deviations due to the complex and nonlinear couplings of a rocket.

A Monte Carlo simulation can be employed to address this type of problem. A Monte Carlo simulation works well with naturally probabilistic problems that are too difficult to solve analytically. With this method, any influences of uncertainties in the rocket design can be recognized by analyzing the trajectory patterns and dispersions. In this case, the uncertainty in each of the moments of inertia can be isolated and the significance of each uncertainty can act as feedback and baseline to develop more accurate manufacturing methods.

1.4 Problem Statement

The key problems in this thesis are:

- The individual effects from each of the moments of inertia's uncertainty;
- The distribution of the impact points under moments of inertia's uncertainties;
- The stability of the rocket under moments of inertia's uncertainties;
- The comparison between Monte Carlo simulations with a small and large number of runs.

1.5 Research Objectives

The objectives to be achieved in this thesis are:

- To determine which of the moments of inertia's uncertainties gives the largest influence on the rocket's dynamics;

- To identify patterns in the impact points due to moments of inertia's uncertainties;
- To assess the rocket's stability under moments of inertia's uncertainties;
- To investigate the optimal number of Monte Carlo iterations.

1.6 Research Scope and Limitation

In this thesis, it is assumed that:

- The rocket and its motor is assumed to be perfectly symmetrical (by mass and shape);
- The effects of the Earth's rotation, curvature, and mass distribution are neglected;
- The simulation will not consider the rocket's structural integrity.
- The moments of inertia's uncertainty are normally distributed.

This thesis is limited to:

- Only maximum range, maximum altitude, final impact coordinates, angle of attack, and sideslip angle will be used as the indicators;
- Numerical nature of the research exposes the results to numerical errors, idealizations, and limitations;
- The results may only be valid for the RX-200C rocket.

1.7 Significance of the Study

The results of this thesis can provide useful insight into the effects of imperfections in the manufacturing of LAPAN's solid propellant design. This thesis can also act as a reference model for a controller that addresses moments of inertia uncertainties. Additionally, tools developed during this thesis such as interfaces between multiple applications and the rocket modeling structure paradigm can be used for LAPAN future rocket projects.

CHAPTER 2
LITERATURE REVIEW

2.1 The Earth's Atmosphere

The earth's atmosphere is a mixture of gases that we commonly call "air". These gases blanket the earth due to gravity. The atmosphere mainly consists of N_2 (78.1%), O_2 (20.9%), Ar (0.9%), and CO_2 (0.03%). Its physical properties such as pressure, temperature, and density change with position, time, and celestial bodies' influences. In addition to the oxygen that it provides, the atmosphere also shields living creatures on earth against radiation and radio waves from space. For our purpose, the atmosphere's influence on an aerospace vehicle plays a significant role in the vehicle's structural integrity and flight dynamics through aerodynamics. Therefore, a proper understanding of the atmosphere will dictate the outcome of a mission.

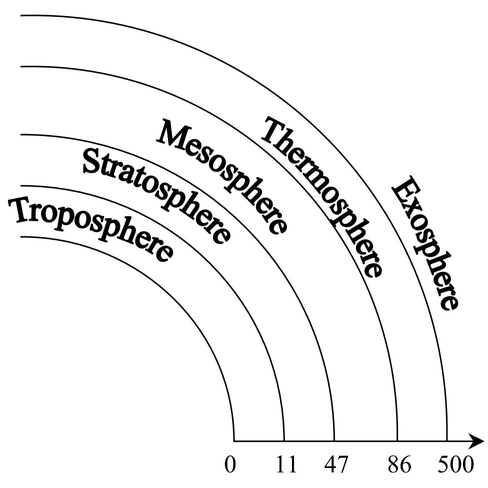

FIGURE 2.1: Atmospheric layers (Tewari, 2007).

The atmosphere can be divided into several layers as shown in Fig. 2.1. The first layer, the *troposphere*, starts from the sea-level altitude up to 11 km of altitude. This is the layer where wind gusts, turbulence, and weather as we know it occurs. The troposphere contains 80% of the earth's atmosphere by mass which makes it the thickest atmospheric layer. Starting from 11 km to 47 km of altitude is the *stratosphere*. In this layer, the wind profile is calmer but faster. Here, the temperature increases due to a high concentration of ozone absorbing solar radiation. The next layer is the *mesosphere* which ranges from 47 km to 86 km of altitude. The temperature in this layer decreases with a diminishing number of ozone in higher altitudes. This layer is also the starting point of another layer, the *ionosphere*, where free electrons and charged particles exist due to solar radiation and low particle density. The *thermosphere* is the next atmospheric layer. Starting from 90 km to 500 km of altitude, solar activity commences to greatly influence the atmospheric properties in the thermosphere region. Finally, the last layer is the *exosphere* where particles can escape the earth into space. The exosphere starts from 500 km and spans indefinitely into outer space.

Adding time variations to the diversity of the atmospheric layers makes predicting atmospheric properties a more challenging task. Atmospheric data is still nonetheless needed as a reference for various calculations involving atmospheric effects. To fill this demand, a standard model was created. The standard atmosphere bases its calculation of the atmospheric properties using the hydrostatic equation, temperature lapse rate data, and perfect gas equation. The results of the calculation are the atmospheric properties as a function of geopotential altitude. The variation of atmospheric properties based on COESA 1976 (*U.S. Standard Atmosphere, 1976*, 1976) is given in Fig. 2.2.

2.2 Gravity

For thousands of years, mankind has noticed that falling objects seem to be pulled towards the earth. This phenomenon is famously called the gravity of the earth. Isaac Newton then formalized this statement by saying that the immense mass of the Earth is the source of its gravity and that gravity can also be generalized for other celestial bodies. Assuming a completely spherical and homogenous Earth,

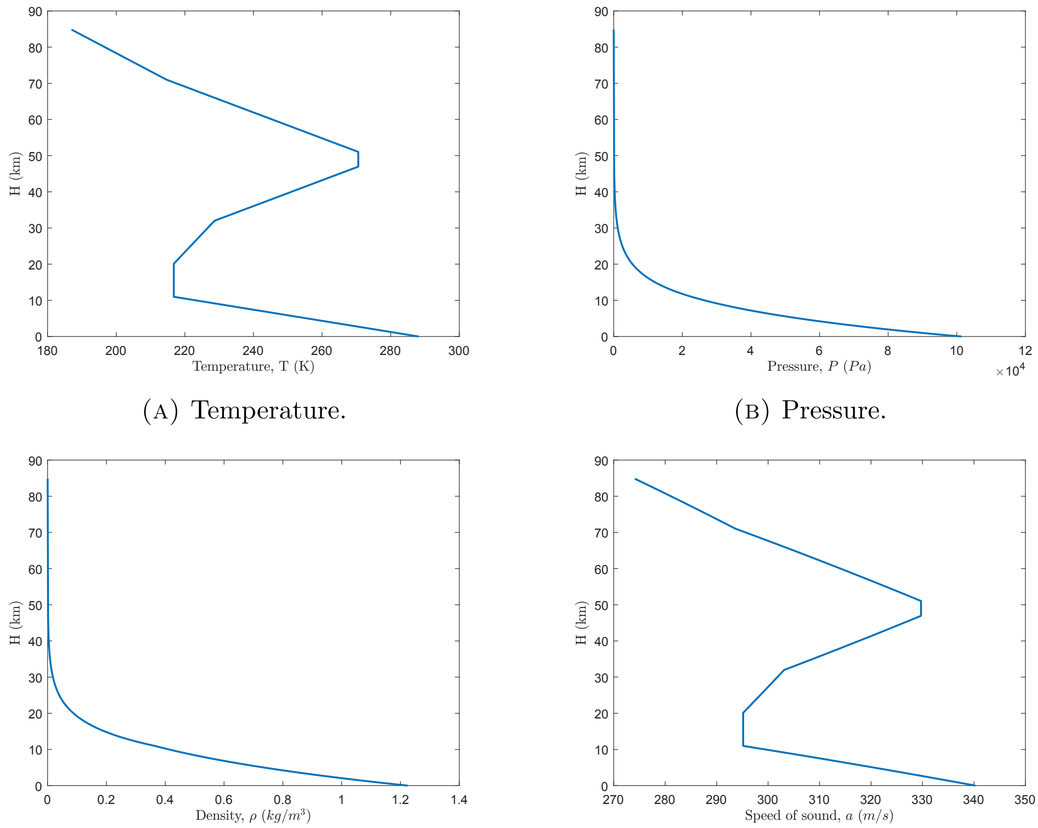

(A) Temperature.

(B) Pressure.

(C) Density.

(D) Speed of sound.

FIGURE 2.2: COESA 1976 derived atmospheric properties as a function of geopotential altitude H.

Newton's law of gravitation can mathematically describe the Earth's gravitational acceleration as

$$g = \frac{GM}{(h + r_e)^2} \tag{2.1}$$

where

- $g \triangleq$ Earth's gravitational acceleration;
- $G \triangleq$ Earth's gravitational constant;
- $M \triangleq$ Earth's mass;
- $h \triangleq$ The rocket's geometric altitude;
- $r_e \triangleq$ Earth's radius.

Figure Fig. 2.3 shows the gravitational acceleration values calculated using Eq. 2.1.

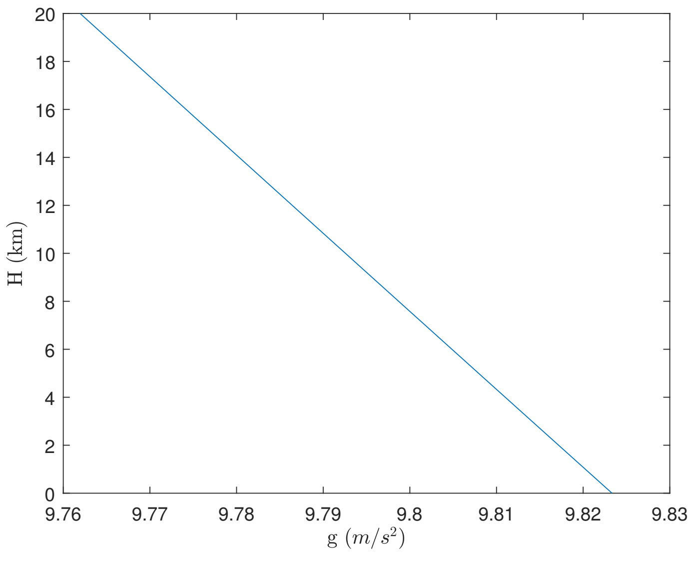

FIGURE 2.3: Newtonian gravitational acceleration up to 20 km altitude.

2.3 Equations of Motion

In classical mechanics, the motion of a rocket can be quantitatively described by a set of differential equations that are derived from Newton's laws (dynamical equations) and motion kinematics. In total, there will be 4 sets of equations; force equations, moment equations, translational and rotational kinematics equations; which will correspond to 12 scalar equations.

2.3.1 Reference Frames and Coordinate System

A reference frame defines the relative directions in space through its axes and unit vectors while the corresponding coordinate system quantitatively describes the position of the particles of interest. Newton's laws are only valid for observers in a special frame called the inertial frame which is commonly known as a frame that does not accelerate and/or rotate. As a consequence of taking the Earth as an inertial frame, the Earth is assumed to be non-rotating.

Two additional reference frames are going to be introduced; the local horizontal frame and the body frame. A local horizontal frame is a copy of the inertial frame whose origin is translated to the rocket's center of gravity. Thus, the local horizontal frame shares the same unit vectors with the inertial frame. A body frame is a frame whose origin is fixed to the rocket's center of gravity with its orientation following the rocket's attitude. The relationship between the inertial and body reference frame is shown in Fig. 2.4.

By convention, the directions of the axes in the inertial frame (x_i, y_i, z_i) follow the North-East-down system. For the body frame, the axes (x_b, y_b, z_b) follow the forward-right-down system. To simplify the relationship of the rocket's position and attitude between the body and the inertial frame, the Earth will be assumed to be flat. A flat-Earth non-rotating inertial frame is an acceptable assumption for a relatively short distance and short-duration flight (Jenkins, 1984).

A cartesian coordinate system is chosen to quantitatively measure the rocket's position along with Euler angles to describe the rocket's attitude. With respect to the inertial frame, the rocket's attitude can be decomposed into three Euler angles: roll angle (ϕ), pitch angle (θ), and yaw angle (ψ). Additionally, the angle of attack

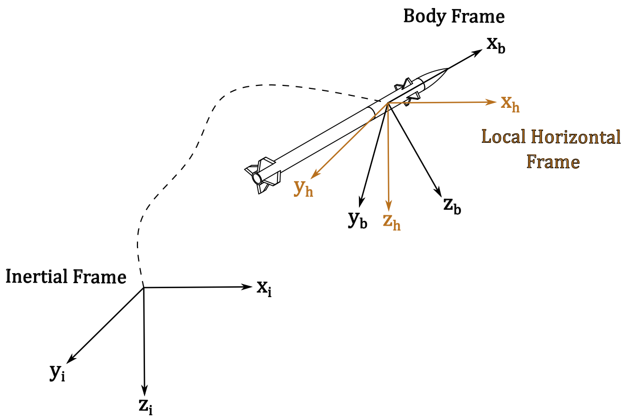

FIGURE 2.4: Relationships between the inertial frame and body frame using Euler angles.

α and the sideslip angle β define the rocket's velocity relative to the freestream atmosphere in the body axis. These angles are mathematically expressed as

$$\begin{aligned} \alpha &= \arctan\left(\frac{w}{u}\right) \\ \beta &= \arcsin\left(\frac{v}{V}\right) \end{aligned} \tag{2.2}$$

with

$$\begin{bmatrix} u \\ v \\ w \end{bmatrix} = \begin{bmatrix} u_s \\ v_s \\ w_s \end{bmatrix} + \begin{bmatrix} u_w \\ v_w \\ w_w \end{bmatrix} \tag{2.3}$$

or in vector forms

$$\mathbf{V} = \mathbf{V}_s + \mathbf{V}_w \tag{2.4}$$

where

- $\mathbf{V} \triangleq$ Freestream velocity in body frame;
- $\mathbf{V}_s \triangleq$ Rocket's velocity in the body frame relative to a static atmosphere;
- $\mathbf{V}_w \triangleq$ Wind velocity disturbance in the body frame.

The sideslip angle can also be expressed for $V \approx u$ as

$$\beta' = \arctan\left(\frac{v}{u}\right) \tag{2.5}$$

The illustration of the wind angles is given in Fig. 2.5.

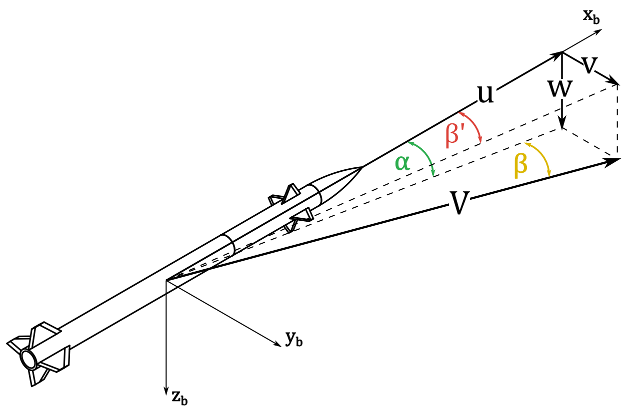

FIGURE 2.5: Wind angles representation.

2.3.2 System of Particles

Using Newton's laws implies that the rocket is assumed to be a point mass. In order to describe the rocket's attitude, the rocket will also be assumed to be taken as a system of particles called a rigid body whose characteristics are concentrated at its center of mass. In other words, any translational and rotational changes that are 'felt' by the center of mass are the same changes that are 'felt' by all of the particles in the rigid body; e.g. $a_{cm} = a_{body}$ and $\omega_{cm} = \omega_{body}$. Henceforth, the term center of mass will be considered analogous to the center of gravity.

Due to the large contribution of the fuel mass to the entire rocket mass, the changes in the mass profile (e.g. mass, inertia, the center of mass position, and their time derivatives) are going to be taken into account. However, the rocket is assumed to not undergo any deformations to its structure due to internal and external forces and moments. The rocket will then be redefined as a rigid body with a variable mass.

The rotational behaviors of a rigid body when exposed to moments can be characterized by its inertia tensor. The inertia tensor represents a rigid body's rotational resistance and inertial coupling. Inertial coupling determines whether one rotation in one axis will also induce another rotation in another axis. The inertia tensor is going to be represented in the body coordinate system. It is mathematically described as

$$\mathbf{I} = \begin{bmatrix} I_{xx} & -I_{xy} & -I_{xz} \\ -I_{xy} & I_{yy} & -I_{yz} \\ -I_{xz} & -I_{yz} & I_{zz} \end{bmatrix} \tag{2.6}$$

where

- I_{xx}, I_{yy}, and $I_{zz} \triangleq$ The second mass moment of inertia in x-, y-, and z-axis, respectively;
- I_{xz}, I_{xy}, and $I_{yz} \triangleq$ The products of inertia in xz-, xy-, and yz-plane, respectively.

For any rigid body, there exists a set of coordinate axis called the principal axes in which all of the three products of inertia are zero, such that

$$\mathbf{I} = \begin{bmatrix} I_{xx} & 0 & 0 \\ 0 & I_{yy} & 0 \\ 0 & 0 & I_{zz} \end{bmatrix} \tag{2.7}$$

2.3.3 Coriolis Law

External forces are normally described in the body frame. However, the basic form of Newton's 2nd law only accounts for motions observed in an inertial frame. Therefore, a vector transformation between an inertial and a rotating body frame is needed. This relationship is called the Coriolis law. The Coriolis law relates the time derivative of a vector between an inertial and a rotating frame

$$\left.\frac{d\rho}{dt}\right|_i = \left.\frac{d\rho}{dt}\right|_b + \left.(\mathbf{\Omega} \times \rho)\right|_b \tag{2.8}$$

where ρ is any vector fixed to the rotating frame and $\mathbf{\Omega}$ the angular velocity of the rotating frame while the subscripts i and b indicate that the particular terms are observed in the inertial and the body frame respectively.

2.3.4 Dynamical Equations

The translational and rotational equations for a rocket derived from Newton's 2nd law take on a similar form (Cornelisse, Schöyer, & Wakker, 1979)

- Translational Motion

$$m\frac{d\mathbf{V}}{dt}\bigg|_i = \mathbf{F}_c + \mathbf{F}_e \tag{2.9}$$

- Rotational Motion

$$\frac{d}{dt}(\mathbf{I}\cdot\mathbf{\Omega})\bigg|_i - \frac{d\mathbf{I}}{dt}\bigg|_b \cdot \mathbf{\Omega} = \mathbf{M}_c + \mathbf{M}_e \tag{2.10}$$

where

- $\mathbf{F}_c$ and $\mathbf{M}_c \triangleq$ Coriolis force and moment;
- $\mathbf{M}_e$ and $\mathbf{M}_e \triangleq$ External force and moment;
- m and $\mathbf{I} \triangleq$ The rocket's mass and inertia;
- $\mathbf{V}$ and $\mathbf{\Omega} \triangleq$ The rocket's translational and angular velocity.

The external forces and moments can be represented by the summation of forces and moments due to gravity ($\mathbf{F}_g$ & $\mathbf{M}_g$), aerodynamics ($\mathbf{F}_a$ & $\mathbf{M}_a$), and thrust ($\mathbf{F}_t$ & $\mathbf{M}_t$)

$$\mathbf{F}_e = \mathbf{F}_g + \mathbf{F}_a + \mathbf{F}_t \tag{2.11}$$

$$\mathbf{M}_e = \mathbf{M}_g + \mathbf{M}_a + \mathbf{M}_t \tag{2.12}$$

Using Coriolis law (Eq. 2.8) to express the remaining derivatives on the left hand side of Eq. 2.9 and Eq. 2.10 in the body frame yields

$$\frac{d\mathbf{V}}{dt}\bigg|_i = \frac{d\mathbf{V}}{dt}\bigg|_b + (\mathbf{\Omega}\times\mathbf{V})\bigg|_b \tag{2.13}$$

$$\frac{d}{dt}(\mathbf{I}\cdot\mathbf{\Omega})\bigg|_i = \frac{d\mathbf{I}}{dt}\bigg|_b \cdot \mathbf{\Omega} + \mathbf{I}\cdot\frac{d\mathbf{\Omega}}{dt}\bigg|_b + \mathbf{\Omega}\times(\mathbf{I}\cdot\mathbf{\Omega}). \tag{2.14}$$

From this point onwards, the subscript b will be dropped while also considering that the Coriolis and external forces and moments will also be derived in the body frame. Equations Eq. 2.9 and Eq. 2.10 can then be rewritten as

$$m\frac{d\mathbf{V}}{dt} + m(\mathbf{\Omega} \times \mathbf{V}) = \mathbf{F}_c + \mathbf{F}_g + \mathbf{F}_a + \mathbf{F}_t \tag{2.15}$$

$$\mathbf{I} \cdot \frac{d\mathbf{\Omega}}{dt} + \frac{d\mathbf{I}}{dt} \cdot \mathbf{\Omega} + \mathbf{\Omega} \times (\mathbf{I} \cdot \mathbf{\Omega}) - \frac{d\mathbf{I}}{dt} \cdot \mathbf{\Omega} = \mathbf{M}_c + \mathbf{M}_g + \mathbf{M}_a + \mathbf{M}_t. \tag{2.16}$$

2.3.5 Kinematic Equations

Eq. 2.15 and Eq. 2.16 are sufficient to analyze the stability and control of a rocket. However, these two equations are unable to give direct information on how the rocket's position and orientation change in the inertial frame. The rocket's position and orientation are used to calculate gravitational acceleration, thrust, and aerodynamic forces and moments. There needs to be another set of equations to relate the rocket's trajectory in the inertial and body frame.

Such equations can be obtained by analyzing the rocket's kinematics. Kinematics is commonly defined as the study of the geometry of motion. For a rocket, the kinematical equations are divided into translational and rotational equations. The construction of these equations is similar to the construction of a vector rotation transformation matrix such that the order of the transformation matrix multiplication is important. In aerospace applications, the standard rotation sequence begins with a yaw rotation, followed by a pitch rotation, into a roll rotation (rotation from z, y, into x-axis). This sequence is used for both translational and rotational kinematics equations.

As a consequence of using the Euler angles, there could be a case called the gimbal locking where the body of interest would lose two rotational degrees of freedom. Mathematically, there would be a singularity in the dynamics calculation. To avoid this condition, the range of the Euler angles will be limited to (Stevens, Lewis, & Johnson, 2016)

$$\begin{aligned} & -\pi < \phi \leq \pi \\ & -\pi/2 \leq \theta \leq \pi/2 \\ & -\pi < \psi \leq \pi \end{aligned} \tag{2.17}$$

Translational Kinematic Equations

The translational kinematics equations can be generated by converting the velocity vectors of the inertial frame to the body frame using rotation matrices. The first rotation occurs about the z-axis of the inertial frame which creates the yaw angle ψ (Fig. 2.6). The result of the first rotation is the intermediate frame 1 denoted by the subscript 1

$$\begin{bmatrix} \dot{x}_1 \\ \dot{y}_1 \\ \dot{z}_1 \end{bmatrix}_1 = \begin{bmatrix} \cos\psi & \sin\psi & 0 \\ -\sin\psi & \cos\psi & 0 \\ 0 & 0 & 1 \end{bmatrix} \begin{bmatrix} \dot{x} \\ \dot{y} \\ \dot{z} \end{bmatrix}_i = \mathbf{H}_i^1 \begin{bmatrix} \dot{x} \\ \dot{y} \\ \dot{z} \end{bmatrix}_i \tag{2.18}$$

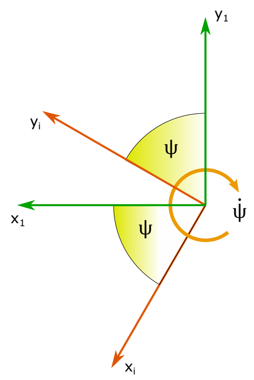

FIGURE 2.6: The relationship between the inertial and first intermediate frame.

Following the first rotation, the resulting intermediate frame is then rotated about its y-axis by the pitch angle θ (Fig. 2.7). Again, the resulting frame is called the intermediate frame 2 denoted by the subscript 2

$$\begin{bmatrix} \dot{x}_2 \\ \dot{y}_2 \\ \dot{z}_2 \end{bmatrix}_2 = \begin{bmatrix} \cos\theta & 0 & -\sin\theta \\ 0 & 1 & 0 \\ \sin\theta & 0 & \cos\theta \end{bmatrix} \begin{bmatrix} \dot{x}_1 \\ \dot{y}_1 \\ \dot{z}_1 \end{bmatrix}_1 = \mathbf{H}_1^2 \begin{bmatrix} \dot{x}_1 \\ \dot{y}_1 \\ \dot{z}_1 \end{bmatrix}_1 \tag{2.19}$$

The last rotation occurs about the x-axis of the intermediate frame 2 which creates the roll angle ϕ (Fig. 2.8). The result of this rotation is the body frame which is given as

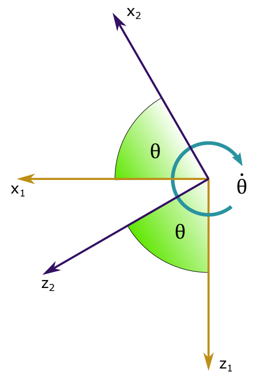

FIGURE 2.7: The relationship between the first and second intermediate frame.

$$\begin{bmatrix} u \\ v \\ w \end{bmatrix}_b = \begin{bmatrix} 1 & 0 & 0 \\ 0 & \cos\phi & \sin\phi \\ 0 & -\sin\phi & \cos\phi \end{bmatrix} \begin{bmatrix} \dot{x}_2 \\ \dot{y}_2 \\ \dot{z}_2 \end{bmatrix}_2 = \mathbf{H}_2^b \begin{bmatrix} \dot{x}_2 \\ \dot{y}_2 \\ \dot{z}_2 \end{bmatrix}_2 \tag{2.20}$$

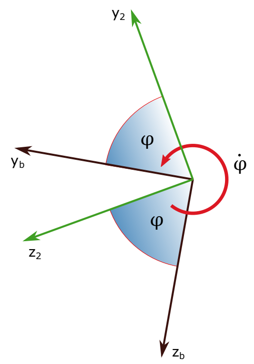

FIGURE 2.8: The relationship between the body and second intermediate frame.

Summarized, the velocity relationships between the inertial and body frame can be given as

$$\begin{bmatrix} u \\ v \\ w \end{bmatrix}_b = \mathbf{H}_2^B \mathbf{H}_1^2 \mathbf{H}_I^1 \begin{bmatrix} \dot{x} \\ \dot{y} \\ \dot{z} \end{bmatrix}_i = \mathbf{H}_i^b \begin{bmatrix} \dot{x} \\ \dot{y} \\ \dot{z} \end{bmatrix}_i \tag{2.21}$$

with

$$\mathbf{H}_i^b = \begin{bmatrix} c\theta c\psi & c\theta s\psi & -s\theta \\ -c\phi s\psi + s\phi s\theta c\psi & c\phi c\psi + s\phi s\theta s\psi & s\phi c\theta \\ s\phi s\psi + c\phi s\theta c\psi & -s\phi c\psi + c\phi s\theta s\psi & c\phi c\theta \end{bmatrix} \tag{2.22}$$

where c and s in Eq. 2.22 represent cosine and sine functions respectively. Furthermore, by calculating the inverse of $\mathbf{H}_i^b$ it can be proven that the inverse and the transpose of $\mathbf{H}_i^b$ are identical, which also means that

$$(\mathbf{H}_i^b)^{-1} = (\mathbf{H}_i^b)^T = \mathbf{H}_b^i \tag{2.23}$$

thus

$$\begin{bmatrix} \dot{x} \\ \dot{y} \\ \dot{z} \end{bmatrix} = \mathbf{H}_b^i \begin{bmatrix} u \\ v \\ w \end{bmatrix} \tag{2.24}$$

Rotational Kinematics Equations

Compared to its translational counterpart the projection method is less intuitive geometrically to transform angular rates from an inertial frame to a body frame and vice-versa. Therefore, a different approach will be taken while also noting that the individual rotations can be combined through vector additions provided the rotation vectors involved are transformed into the body frame before the addition.

Referring to Fig. 2.6, 2.7, and 2.8, it can be seen that the first rotation (yawing) occurs about the z-axis of the inertial frame, z_i, the second rotation (pitching) occurs about the y-axis of the intermediate frame 1, y_1, and the last rotation (rolling) occurs about the x-axis of the intermediate frame 2, x_2. In the light of the previous paragraph, the vector additions of these rotation vectors would equate to the angular rates in the body frame

$$\begin{bmatrix} p \\ q \\ r \end{bmatrix}_b = \begin{bmatrix} \dot{\phi} \\ 0 \\ 0 \end{bmatrix}_2 + \begin{bmatrix} 0 \\ \dot{\theta} \\ 0 \end{bmatrix}_1 + \begin{bmatrix} 0 \\ 0 \\ \dot{\psi} \end{bmatrix}_i \tag{2.25}$$

The individual rotations will now be transformed into the body frame. This is done by considering the correlations between the frames described in Eq. 2.18, 2.19, and 2.20. The transformation results to

$$\begin{aligned}\begin{bmatrix} p \\ q \\ r \end{bmatrix}_b &= \mathbf{H}_2^b \begin{bmatrix} \dot{\phi} \\ 0 \\ 0 \end{bmatrix}_2 + \mathbf{H}_2^b\mathbf{H}_1^2 \begin{bmatrix} 0 \\ \dot{\theta} \\ 0 \end{bmatrix}_1 + \mathbf{H}_2^b\mathbf{H}_1^2\mathbf{H}_i^1 \begin{bmatrix} 0 \\ 0 \\ \dot{\psi} \end{bmatrix}_i \\ &= \begin{bmatrix} 1 & 0 & -\sin\theta \\ 0 & \cos\phi & \sin\phi\cos\theta \\ 0 & -\sin\phi & \cos\phi\cos\theta \end{bmatrix} \begin{bmatrix} \dot{\phi} \\ \dot{\theta} \\ \dot{\psi} \end{bmatrix}_i \end{aligned} \tag{2.26}$$

Inversing Eq. 2.26 to solve for angular rates in the inertial frame yields

$$\begin{bmatrix} \dot{\phi} \\ \dot{\theta} \\ \dot{\psi} \end{bmatrix}_i = \begin{bmatrix} 1 & \sin\phi\tan\theta & \cos\phi\tan\theta \\ 0 & \cos\phi & -\sin\phi \\ 0 & \sin\phi\sec\theta & \cos\phi\sec\theta \end{bmatrix} \begin{bmatrix} p \\ q \\ r \end{bmatrix}_b \tag{2.27}$$

2.3.6 Forces and Moments

Thrust Force and Moment

A rocket engine is a type of propulsion system that, unlike a conventional aircraft, also carries its own oxidizer in addition to its fuel for combustion. Similar to a jet engine, the basic principle of a rocket engine is to produce thrust by ejecting fuel through its nozzle. The nett thrust from a rocket engine can be mathematically expressed by

$$T_{nett} = \dot{m}_e V_e + (P_e - P)A_e \tag{2.28}$$

where

- $\dot{m}_e$ and $V_e \triangleq$ The flowrate and velocity of expelled mass at the exhaust nozzle, respectively;
- P and $P_e \triangleq$ The ambient and exhaust nozzle static pressure, respectively;
- $A_e \triangleq$ The surface area of the exhaust nozzle.

The rocket engine performance is commonly measured by an engine static test. Thrust data from an engine static test at a known static pressure can be expressed mathematically as

$$T_{data} = \dot{m}_e V_e + P_e A_e \tag{2.29}$$

Knowing that the ambient static pressure is a function of altitude, the modified thrust equation can be rewritten as

$$T_{nett} = T_{data} - P(h) A_e \tag{2.30}$$

Assuming that there is no more pressure difference due to thrust at the rocket's nozzle after burnout, the final thrust equation can be expressed as

$$T = \begin{cases} T_{nett}, & \text{if } 0 < t \leq t_b \\ 0, & \text{if } t > t_b \end{cases} \tag{2.31}$$

where t_b is the rocket burn time. Since the rocket engine is completely symmetrical and collinear with the rocket's longitudinal axis, we will neglect the moment due to thrust and assume that the thrust will only act in the direction of the rocket's x-axis. The resulting thrust can be represented in the vector form as

$$\mathbf{F}_t = \begin{bmatrix} T \\ 0 \\ 0 \end{bmatrix} \tag{2.32}$$

Aerodynamic Forces and Moments

Any body immersed in a fluid and moving relative to the fluid experiences dynamic force and moment. For air, this phenomenon is subsequently called the aerodynamic force and moment. The aerodynamic force and moment can be described mathematically in vector form as

- Aerodynamic Force

$$\mathbf{F}_a = q_\infty S \begin{bmatrix} C_A \\ C_Y \\ C_N \end{bmatrix} = \begin{bmatrix} X' \\ Y' \\ Z' \end{bmatrix} \tag{2.33}$$

- Aerodynamic Moment

$$\mathbf{M}_a = q_\infty S l_{ref} \begin{bmatrix} C_l \\ C_m \\ C_n \end{bmatrix} = \begin{bmatrix} L' \\ M' \\ N' \end{bmatrix} \tag{2.34}$$

with

$$q_\infty = \frac{1}{2}\rho V^2 \tag{2.35}$$

where

- $q_\infty \triangleq$ Dynamic pressure;
- $\rho \triangleq$ Air density;
- $V \triangleq$ Freestream velocity;
- $S \triangleq$ Reference surface area;
- $[C_A\ C_Y\ C_N]^T \triangleq$ From left to right: axial, side force, and normal force coefficient;
- $[C_l\ C_m\ C_n]^T \triangleq$ From left to right: rolling, pitching, and yawing moment coefficient;
- $l_{ref} \triangleq$ Reference length.

The aerodynamic coefficients are dimensionless constants that are able to describe the aerodynamic characteristics of a body. They can be determined analytically, numerically, experimentally, or a combination of the three methods. These coefficients can be initially defined as functions of:

- Angular velocity $\mathbf{\Omega} = [p\ q\ r]^T$;
- Control surface deflection $\delta_c = [\delta_a\ \delta_e\ \delta_r]^T$;
- Angle of attack α and its rate $\dot{\alpha}$;
- Sideslip angle β;

- Mach number M;
- Center of gravity x_{cg};
- Reynold's number Re.

The contribution of the control surface deflections can often be omitted for a ballistic flight. The effect of Reynold's number is often negligible for a rocket flight in comparison to other parameters. In general, the center of gravity does not have any obvious role in aerodynamics. However, as the center of gravity is the chosen moment reference center, a moving center of gravity would in turn change the magnitude of the aerodynamic moments.

The influence of the sideslip angle and angular velocites can be approximated using a first-order Taylor series expansion. In line with the longitudinal and lateral-directional decoupling of a symmetric, flying vehicle, the first-order Taylor series approximation for the longitudinal mode can then be given as

$$C_{(lon)}(\mathrm{M}, \alpha, x_{cg}, \dot{\alpha}, q) = C_{(lon)} \tag{2.36}$$

$$C_{(lon)} = C_{(lon)_0} + \frac{\partial C_0}{\partial \dot{\alpha}}\dot{\alpha} + \frac{\partial C_0}{\partial q}q \tag{2.37}$$

with

$$C_{(lon)_0} = C_{(lon)}(\mathrm{M}, \alpha, x_{cg}, 0, 0) \tag{2.38}$$

where every partial derivative are evaluated at varying M, α, and x_{cg} and a constant value of $\dot{\alpha} = 0$ and $q = 0$.

Similarly, the Taylor series expansion for the lateral-directional mode can be given as

$$C_{(ld)}(\mathrm{M}, \alpha, x_{cg}, \beta, p, r) = C_{(ld)} \tag{2.39}$$

$$C_{(ld)} = C_{(ld)_0} + \frac{\partial C_0}{\partial \beta}\beta + \frac{\partial C_0}{\partial p}p + \frac{\partial C_0}{\partial r}r \tag{2.40}$$

with

$$C_{(ld)_0} = C_{(lon)}(\mathrm{M}, \alpha, x_{cg}, 0, 0, 0) \tag{2.41}$$

where every partial derivative are again evaluated at varying M, α, and x_{cg} and a constant value of $\beta = 0$, $p = 0$, and $r = 0$. The partial derivatives in Eq. 2.37 and Eq. 2.40 are defined as the aerodynamic derivative coefficients:

$$
\begin{aligned}
C_{mq} &= \frac{\partial C_m}{\partial\left(\frac{ql_{ref}}{2V}\right)} & C_{Nq} &= \frac{\partial C_N}{\partial\left(\frac{ql_{ref}}{2V}\right)} & C_{Aq} &= \frac{\partial C_A}{\partial\left(\frac{ql_{ref}}{2V}\right)}\\
C_{m\dot{\alpha}} &= \frac{\partial C_m}{\partial\left(\frac{\dot{\alpha}l_{ref}}{2V}\right)} & C_{N\dot{\alpha}} &= \frac{\partial C_N}{\partial\left(\frac{\dot{\alpha}l_{ref}}{2V}\right)} & C_{A\dot{\alpha}} &= \frac{\partial C_A}{\partial\left(\frac{\dot{\alpha}l_{ref}}{2V}\right)}\\
C_{lp} &= \frac{\partial C_l}{\partial\left(\frac{pl_{ref}}{2V}\right)} & C_{np} &= \frac{\partial C_n}{\partial\left(\frac{pl_{ref}}{2V}\right)} & C_{Yp} &= \frac{\partial C_Y}{\partial\left(\frac{pl_{ref}}{2V}\right)}\\
C_{lr} &= \frac{\partial C_l}{\partial\left(\frac{rl_{ref}}{2V}\right)} & C_{nr} &= \frac{\partial C_n}{\partial\left(\frac{rl_{ref}}{2V}\right)} & C_{Yr} &= \frac{\partial C_Y}{\partial\left(\frac{rl_{ref}}{2V}\right)}\\
C_{l\beta} &= \frac{\partial C_l}{\partial \beta} & C_{n\beta} &= \frac{\partial C_n}{\partial \beta} & C_{Y\beta} &= \frac{\partial C_Y}{\partial \beta}
\end{aligned}
$$

where all of the dynamic derivative coefficients are non-dimensionalized using the factor $\frac{l_{ref}}{2V}$. In summary, the aerodynamic forces and moments can be rewritten in terms of the aerodynamic coefficients as

- Aerodynamic Force

$$
\mathbf{F}_a = q_\infty S \begin{bmatrix} C_A \\ C_Y \\ C_N \end{bmatrix} = q_\infty S \begin{bmatrix} C_{A_0} + C_{Aq}\left(\frac{ql_{ref}}{2V}\right) + C_{A\dot{\alpha}}\left(\frac{\dot{\alpha}l_{ref}}{2V}\right) \\ C_{Y_0} + C_{Y\beta}\beta + C_{Yp}\left(\frac{pl_{ref}}{2V}\right) + C_{Yr}\left(\frac{rl_{ref}}{2V}\right) \\ C_{N_0} + C_{Nq}\left(\frac{ql_{ref}}{2V}\right) + C_{N\dot{\alpha}}\left(\frac{\dot{\alpha}l_{ref}}{2V}\right) \end{bmatrix} \tag{2.42}
$$

- Aerodynamic Moment

$$
\mathbf{M}_a = q_\infty S l_{ref} \begin{bmatrix} C_l \\ C_m \\ C_n \end{bmatrix} = q_\infty S l_{ref} \begin{bmatrix} C_{l_0} + C_{l\beta}\beta + C_{lp}\left(\frac{pl_{ref}}{2V}\right) + C_{lr}\left(\frac{rl_{ref}}{2V}\right) \\ C_{m_0} + C_{mq}\left(\frac{ql_{ref}}{2V}\right) + C_{m\dot{\alpha}}\left(\frac{\dot{\alpha}l_{ref}}{2V}\right) \\ C_{n_0} + C_{n\beta}\beta + C_{np}\left(\frac{pl_{ref}}{2V}\right) + C_{nr}\left(\frac{rl_{ref}}{2V}\right) \end{bmatrix} \tag{2.43}
$$

Gravitational Force and Moment

As the chosen moment center is the rocket's center of gravity, the moment due to gravity will be neglected for the moment equations. The gravitational force in the inertial frame can be mathematically expressed in vector form as

$$
\mathbf{F}_g = \begin{bmatrix} 0 \\ 0 \\ mg \end{bmatrix}_i \tag{2.44}
$$

Transforming the gravitational force into the body frame using the rotation matrix $\mathbf{H}_i^b$ from Eq. 2.22 yields

$$\mathbf{F}_g = \mathbf{H}_i^b \begin{bmatrix} 0 \\ 0 \\ mg \end{bmatrix}_i = mg \begin{bmatrix} -\sin\theta \\ \cos\theta\sin\phi \\ \cos\theta\cos\phi \end{bmatrix}_b = \begin{bmatrix} F_{g_x} \\ F_{g_y} \\ F_{g_z} \end{bmatrix} \tag{2.45}$$

Coriolis Force and Moment

The Coriolis force and moment are considered as fictitious force and moment. They appeared in the equations due to the relative motion between the propelled fuel and the center of gravity of the rocket (Cornelisse et al., 1979). The Coriolis force is defined by

$$\mathbf{F}_c = 2\dot{m}\boldsymbol{\Omega} \times \mathbf{r}_n \tag{2.46}$$

The Coriolis force will be neglected due to its small magnitude relative to the rocket thrust. However, the Coriolis moment will not be neglected as it will provide a considerable damping characteristic to the rocket during powered flight. The Coriolis moment is defined by

$$\mathbf{M}_c = -\left.\frac{d\mathbf{I}}{dt}\right|_b \cdot \boldsymbol{\Omega} + \dot{m}\mathbf{r}_n \times (\boldsymbol{\Omega} \times \mathbf{r}_n) \tag{2.47}$$

where

$$\mathbf{r}_n = \begin{bmatrix} x_n \\ y_n \\ z_n \end{bmatrix} \tag{2.48}$$

For a rocket with a circular, flat exhaust nozzle surface area, the center of mass flow $\mathbf{r}_n$ is defined by the distance between the center of mass and the exhaust nozzle surface area center point as shown in Fig. 2.9.

It follows that the terms $-\left.\frac{d\mathbf{I}}{dt}\right|_b$ in Eq. 2.47 and Eq. 2.16 will cancel each other out (the term in Eq. 2.16 is already represented in the body frame). Therefore, the remaining contribution of the Coriolis moment will be expressed as

$$\mathbf{M}_c' = \dot{m}\mathbf{r}_n \times (\boldsymbol{\Omega} \times \mathbf{r}_n) \tag{2.49}$$

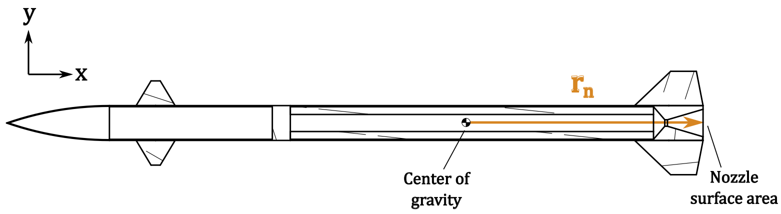

FIGURE 2.9: Center of mass flow.

2.4 Equations of Motion Summary

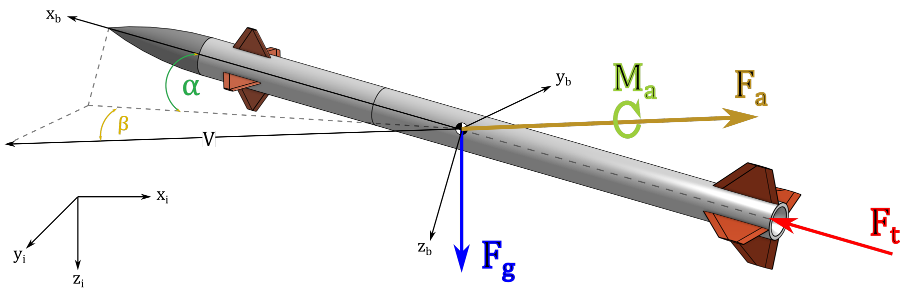

FIGURE 2.10: Free body diagram.

The free-body diagram following the derivations of the equations of motion and the corresponding forces and moments in the previous section is given in Fig.2.10. The contribution of the Coriolis moment will not be included in the free body diagram since it is not considered as an external moment. We can then rewrite the dynamical equations Eq.2.15 and Eq.2.16 in scalar form as

- Force equations:

$$\begin{aligned} m(\dot{u} + qw - rv) &= X' - mg\sin\theta + T \\ m(\dot{v} + ru - pw) &= Y' + mg\cos\theta\sin\phi \\ m(\dot{w} + pv - qu) &= Z' + mg\cos\theta\cos\phi \end{aligned} \tag{2.50}$$

- Moment equations:

$$\begin{aligned} I_{xx}\dot{p} - (I_{yy} - I_{zz})qr &= L' \\ I_{yy}\dot{q} + (I_{xx} - I_{zz})pr &= M' + \dot{m}qx_n^2 \\ I_{zz}\dot{r} - (I_{xx} - I_{yy})pq &= N' + \dot{m}rx_n^2 \end{aligned} \tag{2.51}$$

where we have assumed that the rocket's center of gravity moves along the principal axes (Eq.2.7) and the rocket's center of mass flow is defined as

$$\mathbf{r}_n = \begin{bmatrix} x_n \\ 0 \\ 0 \end{bmatrix} \tag{2.52}$$

2.5 Statistics

2.5.1 Monte Carlo Simulation

A Monte Carlo simulation is a numerical simulation that utilizes the Monte Carlo method where an event is performed several times to generate patterns in the distribution arising from the repeated events. This type of simulation can help find the uncertainty propagation of an equation. The propagation of uncertainty of an equation describes how the uncertainty in the equation's variables affects the outcome of the equation.

The origin of the Monte Carlo method dated back to the World War II-era when American physicists were stuck on the atomic bomb design. The complex nature of an atomic bomb made it hard to be solved with conventional analytical methods. At the present time, the Monte Carlo simulation can be used universally to solve any problems with naturally probabilistic behavior.

A Monte Carlo simulation utilizes random samplings of variables according to a known distribution. A common distribution that is used is the normal distribution due to its frequent occurrence in nature. A Monte Carlo simulation relies on the Law of Large Numbers and the Central Limit Theorem where, if combined, given a large enough sample, the distribution of the population will be normally distributed

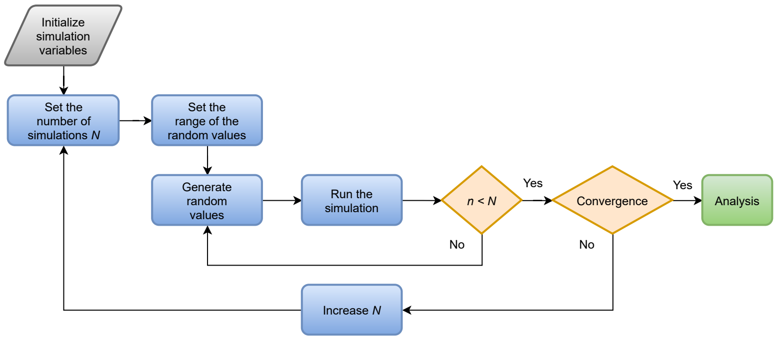

FIGURE 2.11: Flowchart of a Monte Carlo simulation.

and will converge to a single value. The flow of a Monte Carlo simulation is summarized in Fig. 2.11.

Even though the uncertainty is stochastic, the equations of motion are generally deterministic. As soon as the uncertainty is set and the randomising process stops, the whole simulation will become deterministic. Furthermore, the accuracy of a Monte Carlo simulation depends heavily on the number of simulation runs. Thus, the required computing power can grow large quickly. Nonetheless, with the current advancement in computing technology, a Monte Carlo simulation is getting more and more affordable.

2.5.2 Normal Distribution

A normal, or Gaussian, distribution is a type of theoretical probability distribution containing random real values which often occur naturally in real-life distributions. It can be useful to predict an event from a distribution or, the other way around, creating a distribution that has a normal probabilistic nature. The mathematical description of a normal distribution with a mean μ, standard deviation σ, and random value x can be expressed by its probability density function in general form as

$$f(x) = \frac{1}{\sigma\sqrt{2\pi}} e^{-\frac{1}{2}\left(\frac{x-\mu}{\sigma}\right)^2} \tag{2.53}$$

The distinct bell shape of a normal distribution curve is illustrated in Fig. 2.12. One convenient thing about a normal distribution is that the probability of an event occurring can be directly determined by the 68-95-99.7 rule or also formally called

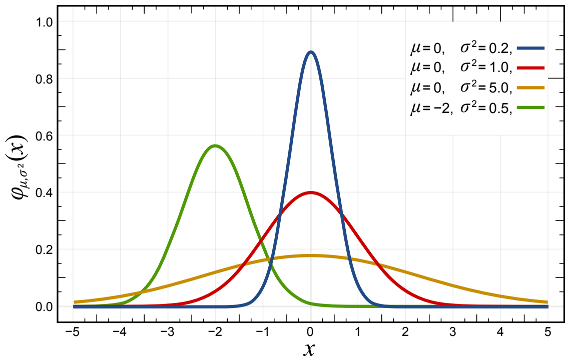

FIGURE 2.12: Various normal distribution curves.

the empirical rule. The empirical rule states that events within 1σ, 2σ, and 3σ distance from the average have a probability of 68%, 95%, and 99.7% (PSU, 2022).

2.5.3 Kernel Density Estimation

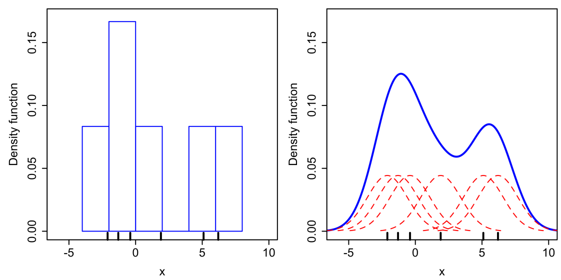

FIGURE 2.13: Comparison between a histogram and kernel density estimation (Drleft, 2010).

A kernel density estimation is a method to approximate the probability density function of a random distribution. In principle, a kernel density estimation works similar to a histogram as demonstrated in Fig. 2.13. One of the main propositions of the kernel density estimation lies in its non-parametric nature where it is assumed that the distribution does not belong to any theoretical probability distributions. The kernel density estimator can be mathematically expressed by

$$\hat{f}_h(x) = \frac{1}{nh}\sum_{i=1}^{n} K\left(\frac{x - x_i}{h}\right) \tag{2.54}$$

where,

- $n \triangleq$ Number of sample data;
- $h \triangleq$ Bandwidth;
- $x_i \triangleq$ Sample data value;
- $K \triangleq$ Kernel function.

From Eq. 2.54 it can be seen that aside from the data sample, the characteristic of a kernel density estimate can be characterized by its kernel function and bandwidth. The selection of the appropriate kernel function and bandwidth may determine the accuracy of the estimate. Fig. 2.14 shows common kernel functions. In general, the selection of the kernel function is not as crucial as the bandwidth. The bandwidth is also commonly referred to as the smoothing parameter. Some data might not be properly represented if the smoothing parameter is too big while the data might be too "jaggy" if the smoothing parameter is too small. In practice, the bandwidth can be tuned manually or automatically using tuning algorithms.

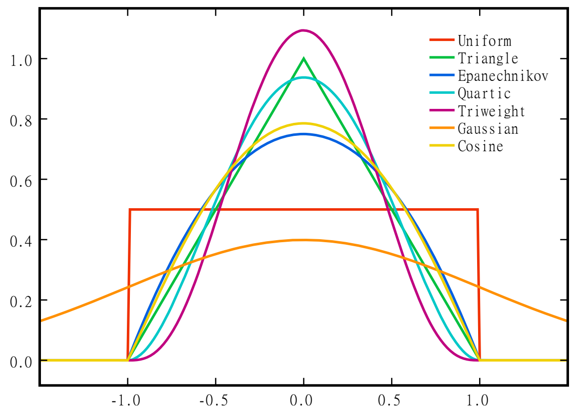

FIGURE 2.14: Various kernel functions (Amberg, 2008).

CHAPTER 3
RESEARCH METHODOLOGY

3.1 Research Overview

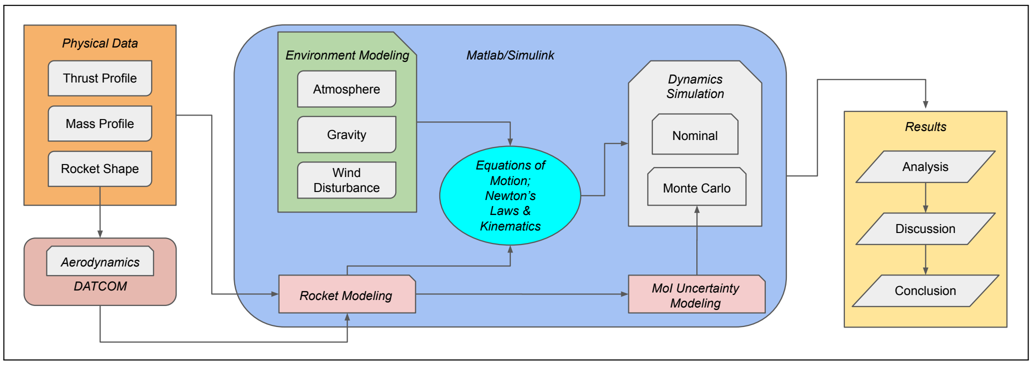

FIGURE 3.1: Research flowchart

This thesis begins by collecting and processing the mass profile, thrust data, and shape of the rocket RX-200C. The required data such as the rocket shape and thrust profile are obtained from LAPAN. The aerodynamic characteristics of the rocket are generated by using Missile DATCOM. Missile DATCOM takes the rocket's shape and flight condition as input and outputs the rocket's aerodynamic coefficients. The resulting rocket data will then be initialized in MATLAB workspace using scripts and stored in a file to be used by the Simulink model.

The dynamical framework and simulation are modeled in Simulink. Both specialized built-in and custom made functions (i.e. for mathematical equations) will be utilized. Separate modeling will be created for:

1. Forces and Moments: Thrust, aerodynamics, gravity, and Coriolis;

2. Mass and moments of inertia

3. Atmosphere

4. Sensor/Data Processing

The ballistic simulation analysis is categorized into two cases:

- Nominal: With wind disturbance but without uncertainty;

- Uncertainty: Monte Carlo simulations with wind disturbance and moments of inertia uncertainty.

The Monte Carlo simulation is set up through a MATLAB script that generates randomized moments of inertia profile for the Simulink model before each run. Simulation results are transferred to the MATLAB workspace and stored in several saved variable files. Lastly, data visualization will be done in MATLAB and Python. The focus of the analysis will be the trajectory and stability of the rocket under moments of inertia uncertainty.

3.2 Physical Modeling

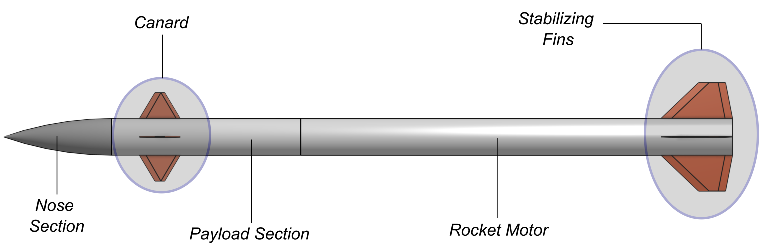

(A)

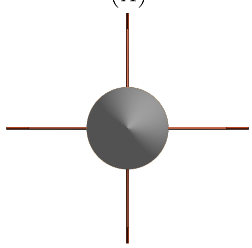

(B)

FIGURE 3.2: (A)RX-200C sections overview. (B) RX-200C front view.

Part	m (kg)	x_{cg} (m)	I_{xx} (kg m^2)	I_{yy} (kg m^2)
Rocket, fully fueled	216.658	2.182	1.5	200.83
Fuel	79.91	$2.714_{(c)}$	$0.4593_{(c)}$	$30.1022_{(c)}$
Rocket, after burnout	$136.748_{(c)}$	$1.8711_{(c)}$	$1.0407_{(c)}$	$134.8952_{(c)}$

Note: Inertia values are taken at the particular part's center of mass.
Subscript (c) indicates a calculated/approximated value.

TABLE 3.1: Summary of the mass characteristics.

The rocket that will be analyzed in this thesis is the LAPAN RX-200C rocket. The RX-200C rocket is a solid-propellant rocket having a 20 cm maximum diameter and a length of 4.062 m. The three main sections of the rocket as well as its two fin sets are displayed in Fig. 3.2. Each of the two fin sets has its own airfoil profile for its four fins. The front fin set features all-movable fins which are commonly referred to as canards while the fins for the aft fin set are fixed and act as stabilizing fins. The complete sizing of the rocket and each fin set can be found in Appendix A.

It can be seen from Tab. 3.1 that the mass contribution of the fuel (fuel fraction) is approximately 35% of the wet mass of the rocket. This mass is going to be ejected only in the span of 10 seconds. For comparison, the typical fuel fraction of modern airliners ranges from 26-45% (*Fuel fraction*, 2020). However, the time it takes for these airliners to spend all of their fuel is in the order of hours. In other words, the mass characteristics of an airliner can then be assumed to be constant for a small time frame several magnitudes lower than its whole flight. For the RX-200C rocket case, however, the mass modeling will have to include the effect of a changing mass through this 10 seconds time frame.

With this in mind, the mass characteristics need to be approximated since the data provided by LAPAN does not include the necessary mass characteristics during engine burn. The mass characteristics that will be approximated are mass, the center of gravity, and moments of inertia.

The moments of inertia I_{yy} and I_{zz} will have the same value due to the rocket's symmetry. The products of inertia will also be zero as the rocket's inertia tensor will be calculated about its center of mass.

Linear interpolation will be used to approximate the mass characteristics between wet and dry mass rocket's condition. The methods to approximate the necessary fuel and dry mass characteristics are summarized in Appendix A. The resulting approximations are summarized in Tab. 3.1 and shown as graphs in Fig. 3.3 and Fig. 3.4. All of the mass characteristics stay constant after the engine stops firing (t > 10 s) and will hold the last value registered at t = 10 s.

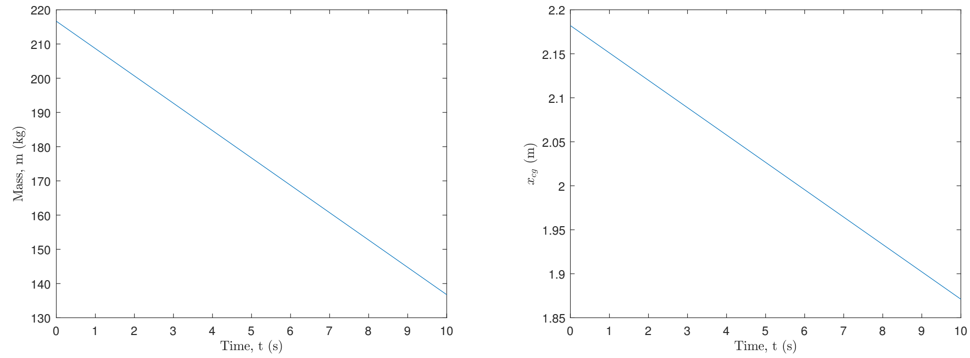

FIGURE 3.3: Mass (left) and center of gravity position (right).

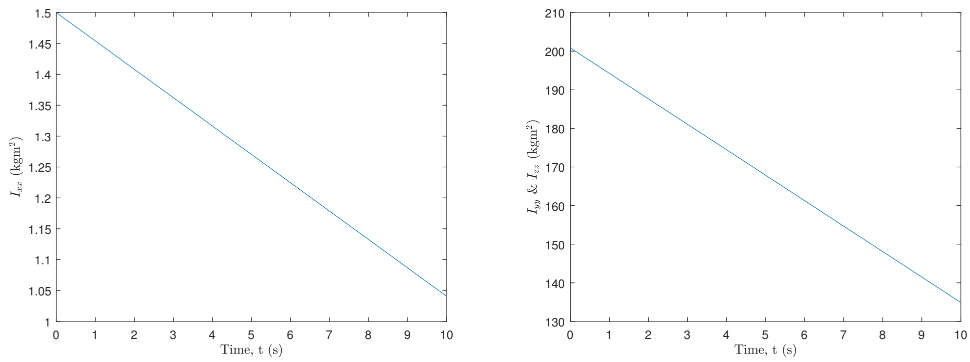

FIGURE 3.4: Second moments of inertia graphs; about x-axis (left) and about y and z-axis (right).

The thrust characteristic of the RX-200C rocket is shown in Fig. 3.5. The data shown in Fig. 3.5 was obtained from a sea-level static test result by LAPAN. The thrust curve is characteristic of a tubular-type grain geometry. During its 10 seconds engine burn the rocket will achieve a maximum thrust of 27.147 kN at time t = 6.6 s.

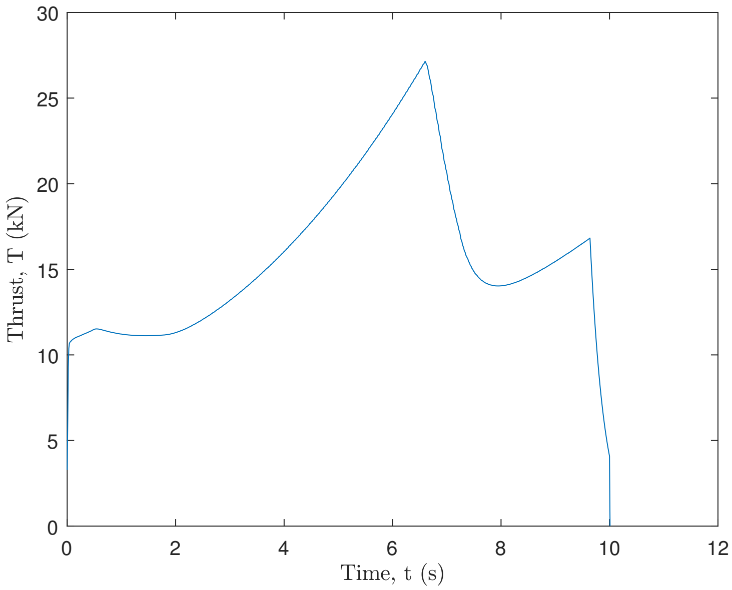

FIGURE 3.5: Thrust Profile.

3.3 Missile DATCOM

The USAF DATCOM is a computer program written in FORTRAN that started out as a handbook developed by the US Air Force to approximate the aerodynamic coefficients of a flying body with analytical and empirical methods. Two types of DATCOM programs exist; Digital DATCOM and Missile DATCOM. Digital DATCOM is specialized for bodies resembling a conventional aircraft while Missile DATCOM is specialized for bodies resembling a missile or a rocket. Usage-wise, the differences between the two versions lie in the terms of the input variables that are used. Digital DATCOM uses aircraft terms while Missile DATCOM uses missile/rocket terms. Additionally, Missile DATCOM is equipped with more appropriate functions for a supersonic flight when compared to Digital DATCOM (Vukelich, 1981). In this thesis, we will be using Missile DATCOM 1997 FORTRAN 90 revision (Blake, 1998).

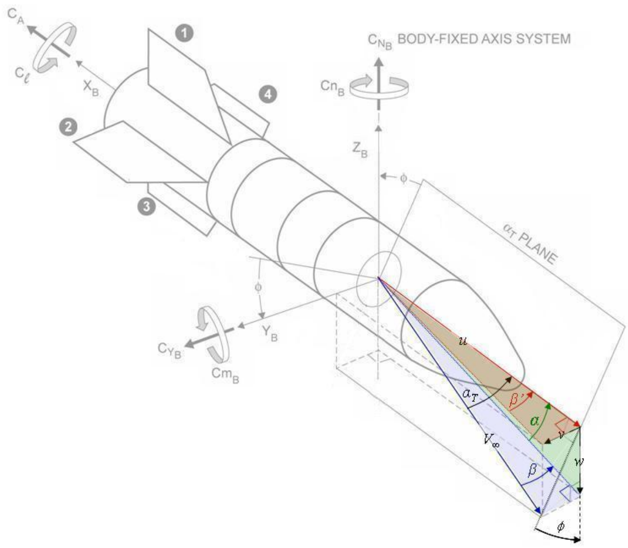

FIGURE 3.6: Missile DATCOM's coordinate system (Auman et al., 2008).

3.3.1 Input Definition

To generate aerodynamic coefficients using Missile DATCOM, an input file must first be prepared. This input file contains the necessary parameters that will represent the shape and flight conditions of the rocket. The input file is in the format of a plain text file (.txt) with a specific filename for005.dat. The execution of an aerodynamics calculation is called a "*case*". Input parameters for a case are divided into variable groups called **namelists** and **control cards**. Note that Missile Datcom has a different coordinate system when compared to the one that is commonly used for conventional aircraft. In this Missile DATCOM version, the sideslip angle β is defined as β' in Fig. 3.6. The full input file is provided in Appendix B. For the full explanations of the available namelists and control cards, the reader is to consult the Missile DATCOM manual (Blake, 1998).

FLTCON Namelist

In this namelist, the ranges for the angle of attack, Mach number, and Reynolds number are specified. The Reynolds number can be substituted by altitude. The program will then calculate the Reynolds number based on the specified Mach

```
$FLTCON
 NALPHA = 19.0,
 ALPHA(1) = -18.,-16.,-14.,-12.,-10.,-8.,-6.,-4.,
 ALPHA(9) = -2.,0.,2.,4.,6.,8.,10.,12.,14.,16.,18.,
 NMACH = 15.0,
 MACH(1) = 0.15,0.3,0.45,0.6,0.75,0.9,1.05,1.2,
 MACH(9) = 1.35,1.5,1.65,1.8,1.95,2.1,2.25,
 ALT(1) = 0.E03,0.E03,0.E03,0.E03,0.E03,0.E03,0.E03,0.E03,
 ALT(9) = 0.E03,0.E03,0.E03,0.E03,0.E03,0.E03,0.E03,
 BETA = 0.,
$END
```

FIGURE 3.7: FLTCON Namelist

number and atmospheric properties of the given altitudes (1962 Standard Atmosphere Model). The sideslip angle can also be included as an input. However, each case can only be executed for one sideslip angle value. The range of these parameters should correspond to the estimated simulation conditions. It is advised to use an increment that will include transonic Mach numbers to accurately simulate the transition between subsonic and supersonic regimes. As previously stated in Sec. 2.3.6, the change of Reynold's number will be neglected. This is reflected by the altitude array ALT in Fig. 3.7 that is set to one value 0.0E03. This value corresponds to the sea-level atmospheric condition.

REFQ Namelist

```
$REFQ
 SREF = 0.12946,
 LREF = 0.203,
 LATREF = 0.203,
 XCG = 2.182,
 ZCG = 0.0,
 BLAYER = 0.0,
 ROUGH = 0.0012,
$END
```

FIGURE 3.8: REFQ Namelist

In the REFQ namelist, the reference quantities are specified. The use of this namelist is optional. If this namelist is not specified by the user, the parameters will then be filled by the program according to preset default settings. For missiles and rockets, it is common to choose the maximum diameter of the rocket as the longitudinal (LREF) and lateral-directional (LATREF) reference lengths. The surface area (SREF) is defined by the area at maximum diameter. The variable XCG is measured as the distance in the x-axis from the nose tip to the rocket's center of gravity. The surface roughness of the rocket is specified using the variable ROUGH.

Aside from the surface roughness, the quantities specified in this namelist can refer to any arbitrary features as long as the user is consistent with their use. For example, LATREF could also refer to the rocket's length instead of the rocket's maximum diameter. However, the rocket's length would then need to be used when calculating the aerodynamic moments or when comparing the aerodynamic coefficients with other rockets.

AXIBOD Namelist

```
$AXIBOD
 X0 = 0.0,
 TNOSE = 1.,
 LNOSE = 0.600,
 DNOSE = 0.203,
 LCENTR = 3.462,
 DCENTR = 0.203,
 DEXIT = 0.16,
$END
```

Figure 3.9: AXIBOD Namelist

In this namelist the shape of the rocket's main body (without the fin sets) from the nose tip to the rocket's nozzle is defined. Illustrated in Fig. 3.10, the body of a rocket can be broken down into 3 main sections; the nose cone, center, and aft sections. The corresponding length and diameter of each section need to be specified. The shape of the nose cone is tangent ogive and coded as TNOSE = 1 as shown in Fig. 3.9. The RX-200C rocket does not have an aft section since the main body diameter of the rocket stays constant right after the nose cone until the nozzle exit. Therefore, the entire section from the base of the nose cone until the nozzle exit will be defined as the rocket's center section.

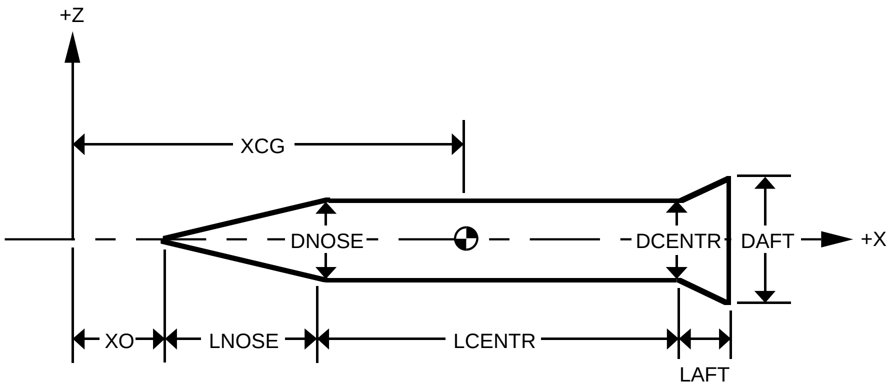

FIGURE 3.10: Main body sections (Blake, 1998).

FINSET Namelist

The shape, position, and orientation of the rocket's fins are defined in the FINSET namelist. The fin panels present in the rocket are grouped into fin sets. The RX200C rocket has two fin sets: a group of four fin panels as canards at the front portion of the rocket and a group of four fin panels as stabilizing fins at the aft section of the rocket. The parameters for each of the finsets need to be specified in two separate namelist. Sequentially from the nose tip, the namelist FINSET1 defines the canard fin set while the namelist FINSET2 defines the stabilizing fins fin set. The graphical interpretations of the position and orientation definitions specified in Fig. 3.11 are shown in Fig. 3.12 and Fig. 3.13.

The airfoil of the fin panels are designated per fin set; i.e. fin panels in the same fin set must have the same type of airfoil. The available airfoil profiles in Missile DATCOM are the hexagonal, circular arc, NACA, and user-defined airfoil types. The hexagonal airfoil will be used in this thesis. The airfoil parameters of a hexagonal airfoil is shown in Fig. 3.14. These parameters are specified as a percentage of the chord at each span station.

Control Cards

Control cards are optional commands that provide extra functionalities to the users. The control cards shown in Fig. 3.15 are used for:

- CASEID RX200C: Specifying the name of the case;

```
$FINSET1
 SECTYP = HEX,
 SSPAN = 0.,0.144,
 CHORD = 0.227,0.054,
 XLE = 0.756,
 STA   = 0.0,
 SWEEP = 31.0,
 NPANEL = 4.0,
 PHIF = 0.0,90.0,180.0,270.0,
 LER = 0.002,0.002,
 ZUPPER = 0.0122,0.054,
 ZLOWER = 0.0122,0.054,
 LMAXU = 0.16,0.6,
 LMAXL = 0.16,0.6,
 LFLATU = 0.745,0.023,
 LFLATL = 0.745,0.023,
$END
```

(A) FINSET1 Namelist.

```
$FINSET2
 SECTYP = HEX,
 SSPAN = 0.,0.200,
 CHORD = 0.399,0.150,
 XLE = 3.663,
 STA = 0.0,
 SWEEP = 46.4,
 NPANEL = 4.0,
 PHIF = 0.0,90.0,180.0,270.0,
 ZUPPER = 0.0075,0.02,
 ZLOWER = 0.0075,0.02,
 LMAXU = 0.145,0.387,
 LMAXL = 0.145,0.387,
 LFLATU = 0.752,0.34,
 LFLATL = 0.752,0.34,
$END
```

(B) FINSET2 Namelist.

FIGURE 3.11: Fin set definition for (A) canard and (B) stabilizing fins.

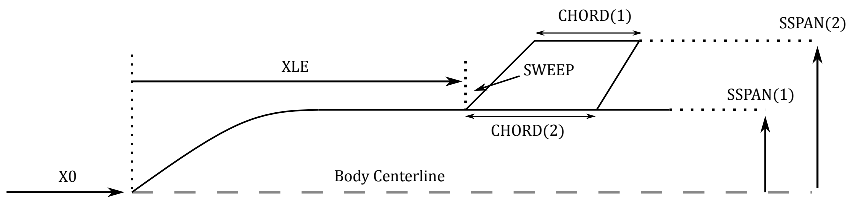

FIGURE 3.12: FINSET position graphical interpretation.

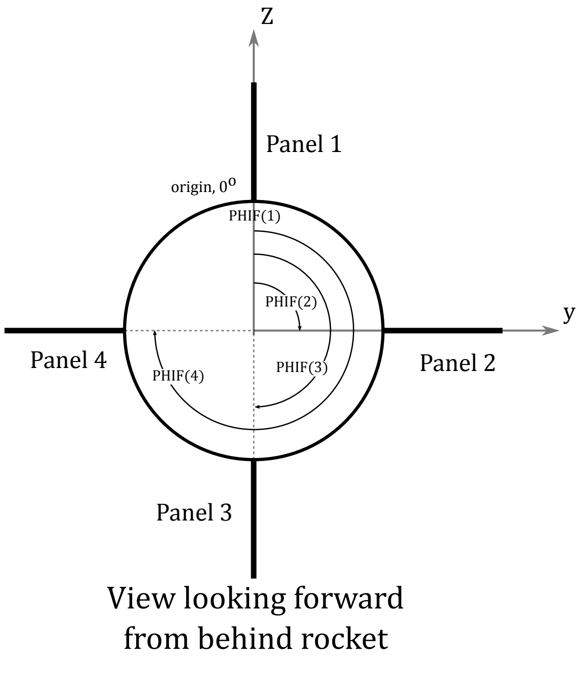

FIGURE 3.13: FINSET orientation graphical interpretation.

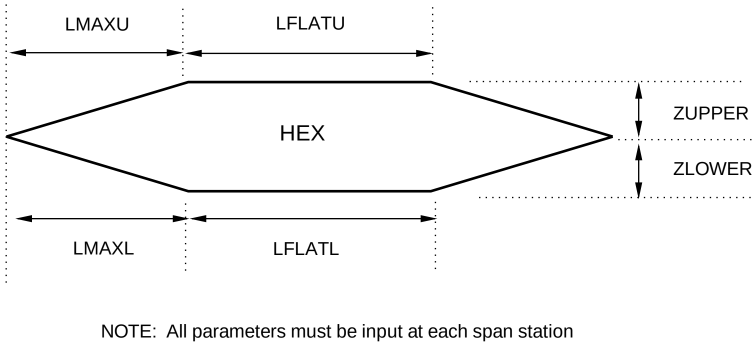

FIGURE 3.14: Hexagonal airfoil parameters (Blake, 1998).

```
CASEID RX200C
PRINT GEOM BODY
DERIV DEG
DIM M
DAMP
NEXT CASE
```

FIGURE 3.15: Control Cards

- PRINT GEOM BODY: Printing output body coordinates to for009.dat output file;
- DERIV DEG: Setting deg/s as the unit of angular rates;
- DIM M: Setting meter as the unit for lengths;
- DAMP: Prompting the program to output dynamic derivatives;
- NEXT CASE: Designating the termination of a case.

3.3.2 Output Description

The resulting aerodynamic coefficients that are calculated by this program can be divided into three categories:

- Static Coefficients:
  - $C_A \triangleq$ axial force coefficient
  - $C_Y \triangleq$ sideforce coefficient

  - $C_N \triangleq$ normal force coefficient
  - $C_l \triangleq$ rolling moment coefficient
  - $C_m \triangleq$ pitching moment coefficient
  - $C_n \triangleq$ yawing moment coefficient

- Static Derivative Coefficients:
  - $C_{N_\alpha} \triangleq$ normal force coefficient derivative with angle of attack
  - $C_{m_\alpha} \triangleq$ pitching moment coefficient derivative with angle of attack
  - $C_{Y_\beta} \triangleq$ side force coefficient derivative with sideslip angle
  - $C_{n_\beta} \triangleq$ yawing moment coefficient derivative with sideslip angle
  - $C_{l_\beta} \triangleq$ rolling moment coefficient derivative with sideslip angle

- Dynamic Derivative Coefficients:
  - $C_{m_q} \triangleq$ pitching moment coefficient derivative with pitch rate
  - $C_{N_q} \triangleq$ normal force coefficient derivative with pitch rate
  - $C_{A_q} \triangleq$ axial force coefficient derivative with pitch rate
  - $C_{m_{\dot\alpha}} \triangleq$ pitching moment derivative with rate of change of angle of attack
  - $C_{N_{\dot\alpha}} \triangleq$ normal force coefficient derivative with rate of change of angle of attack
  - $C_{l_p} \triangleq$ rolling moment coefficient derivative with roll rate
  - $C_{Y_p} \triangleq$ side force coefficient derivative with roll rate
  - $C_{n_p} \triangleq$ yawing moment coefficient derivative with roll rate
  - $C_{l_r} \triangleq$ rolling moment coefficient derivative with yaw rate
  - $C_{Y_r} \triangleq$ side force coefficient derivative with yaw rate
  - $C_{n_r} \triangleq$ yawing moment coefficient derivative with yaw rate

After the program execution, several files will appear in the same folder based on the namelists and control cards that are described in the previous section. The aerodynamic coefficient data is stored in for006.dat file. A copy of the namelists and control cards of the input file is also included in the for006.dat file for error checking. The axisymmetric body and mold line that is "perceived" by the program is also included as shown in Fig. 3.16.

```
1         ***** THE USAF AUTOMATED MISSILE DATCOM * REV 3/99 *****     CASE   1
               AERODYNAMIC METHODS FOR MISSILE CONFIGURATIONS          PAGE   2
                                   RX200C
                        AXISYMMETRIC BODY DEFINITION

                             NOSE   CENTERBODY     AFT BODY        TOTAL
    SHAPE                   OGIVE     CYLINDER     --------
    LENGTH                   .600        3.462         .000        4.062   M
    FINENESS RATIO          2.956       17.054         .000       20.010
    PLANFORM AREA            .082         .703         .000         .784   M**2
    AREA CENTROID            .374        2.331         .000        2.127   M
    WETTED AREA              .259        2.208         .000        2.467   M**2
    VOLUME                   .010         .112         .000         .122   M**3
    VOL. CENTROID            .411        2.331         .000        2.167   M

                              MOLD LINE CONTOUR

     LONGITUDINAL STATIONS     .0000       .0600       .1200       .1800       .2400
         .3000      .3600      .4200       .4800       .5400       .6000       .9462
        1.2924     1.6386     1.9848      2.3310      2.6772      3.0234      3.3696
        3.7158     4.0620*

               BODY RADII      .0000       .0197       .0372       .0525       .0656
         .0767      .0856      .0926       .0975       .1005       .1015       .1015
         .1015      .1015      .1015       .1015       .1015       .1015       .1015
         .1015      .1015*
    NOTE - * INDICATES SLOPE DISCONTINUOUS POINTS
```

FIGURE 3.16: Axisymmetric body and mold line contour definition.

For every specified Mach number the program will produce four tables; each for static, static derivative, longitudinal dynamic derivative, and lateral dynamic derivative aerodynamic coefficients. Information regarding the flight conditions and reference quantities is also provided in every table. The resulting coefficients are presented in the tables as functions of the angle of attack as shown in Fig. 3.17 A more comprehensive sample of the output file is provided in Appendix B.

3.4 MATLAB and Simulink

MATLAB (Matrix Laboratory) is a numerical computing environment and programming language from MathWorks, Inc. It was invented in the 1970s by mathematician Cleve Moler and was initially released in 1984. Programming in MATLAB can be done using scripting and interactive programming. Initialized variables are

```
1        ***** THE USAF AUTOMATED MISSILE DATCOM * REV 3/99 *****     CASE   1
              AERODYNAMIC METHODS FOR MISSILE CONFIGURATIONS          PAGE   3
                                  RX200C
               STATIC AERODYNAMICS FOR BODY-FIN SET 1 AND 2

      ******* FLIGHT CONDITIONS AND REFERENCE QUANTITIES *******
     MACH NO  =        .15              REYNOLDS NO = 3.478E+06 /M
     ALTITUDE =         .0 M        DYNAMIC PRESSURE =   1595.87 N/M**2
     SIDESLIP =        .00 DEG                  ROLL =       .00 DEG
     REF AREA =       .129 M**2        MOMENT CENTER =     2.182 M
     REF LENGTH =      .20 M          LAT REF LENGTH =       .20 M

                  ----- LONGITUDINAL -----     -- LATERAL DIRECTIONAL --
         ALPHA       CN          CM        CA         CY        CLN       CLL

        -18.00    -2.083     4.989      .079      .000      .000      .000
        -16.00    -1.875     4.316      .089      .000      .000      .000
        -14.00    -1.657     3.695      .095      .000      .000      .000
        -12.00    -1.421     3.044      .097      .000      .000      .000
        -10.00    -1.166     2.360      .094      .000      .000      .000
         -8.00     -.890     1.645      .091      .000      .000      .000
         -6.00     -.633     1.084      .092      .000      .000      .000
         -4.00     -.393      .587      .096      .000      .000      .000
         -2.00     -.173      .160      .099      .000      .000      .000
           .00      .000      .000      .100      .000      .000      .000
```

Figure 3.17: Aerodynamic coefficient table, truncated for clarity.

stored in a variable pool called the workspace and can be saved to a MAT-file. Additionally, Simulink, an extension of MATLAB, provides its users with graphical programming capability using a block diagram approach.

Simulink offers various types of block diagrams from low-level to high-level, application-specific blocks. Examples of the low-level blocks include algebraic math operations, calculus, lookup tables, and signal manipulations. A great example of a high-level, application-specific block category is The Aerospace Blockset which provides functionalities such as vehicle dynamics and flight environment modeling. Combined with its capability to solve differential equations, Simulink can be utilized to simulate a nonlinear aerospace system.

Users can use MATLAB functions from Simulink, and vice versa, and transfer data between the two due to their tight integration. MATLAB 2018a version will be used in this thesis.

3.4.1 Simulink Model

The rocket's Simulink model represents the implementation of the equations that have been derived in Chp. 2. Simulink solves the nonlinear differential equations of the rocket model using its built-in ordinary differential equation (ODE) solvers. The available ODE solvers are:

- Discrete (no continuous states);
- ode8 (Dormand-Prince);
- ode5 (Dormand-Prince);
- ode4 (Runge-Kutta);
- ode3 (Bogackl-Shampine);
- ode2 (Heun);
- ode1 (Euler);
- ode14x (extrapolation).

The Simulink model consists of block diagrams that can be grouped into several subsystems. The main subsystems for our rocket model are:

- Dynamical and kinematical equations;
- Wind disturbance;
- Environment;
- Mass characteristics;
- Forces and moments.

The 6-Degree-of-Freedom (6DoF) block that models the equations of motion derived in Sec. 2.3 can be found in the top-most level of the rocket model. As shown in Fig. 3.18, the 6DoF block takes forces, moments, and mass characteristics as input and produces the states of the rocket as the output. The output states can be inspected in the sensor subsystem before being relayed to the MATLAB workspace.

The wind disturbance is modeled as a step function of the sidewind velocity only (v_w) (Fig. 3.19). In hindsight, this type of disturbance is too artificial when

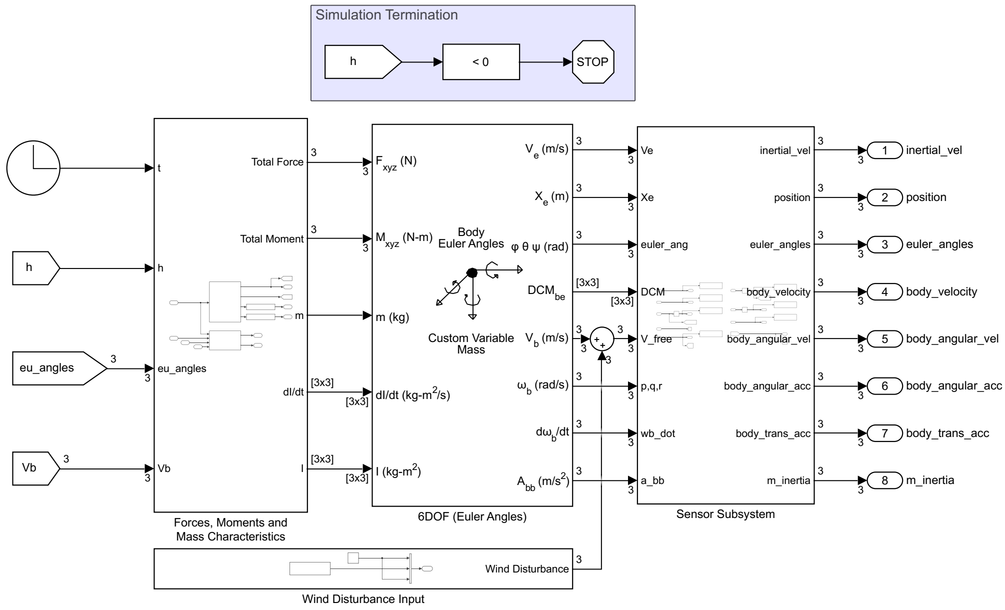

FIGURE 3.18: Top-most level of the Simulink model.

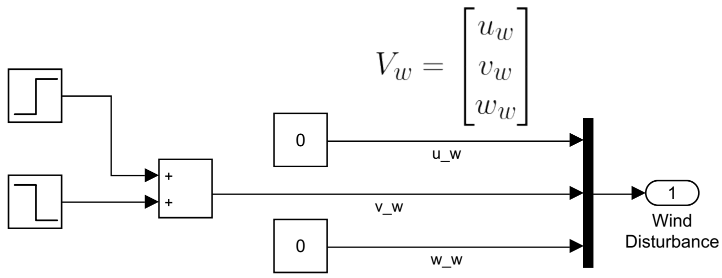

FIGURE 3.19: Block diagrams of the wind disturbance model.

compared to a real wind phenomenon. However, it provides a starting point to intuitively understand the rocket's behavior when exposed to other forms of disturbance. A sidewind velocity disturbance is deliberately chosen as it is the only wind velocity component that can excite the lateral-directional motion of the rocket (as will be further discussed in Sec. 4.3.2).

The environment subsystem contains the atmosphere modeling and the relative air properties (Fig. 3.20). The output of this subsystem is almost exclusively used for aerodynamics calculation except for the ambient pressure that is used for the effective thrust calculation. Shown in Fig. 3.21, the effective thrust force consists of the raw thrust data from the lookup table and the ambient pressure contribution from the atmosphere model.

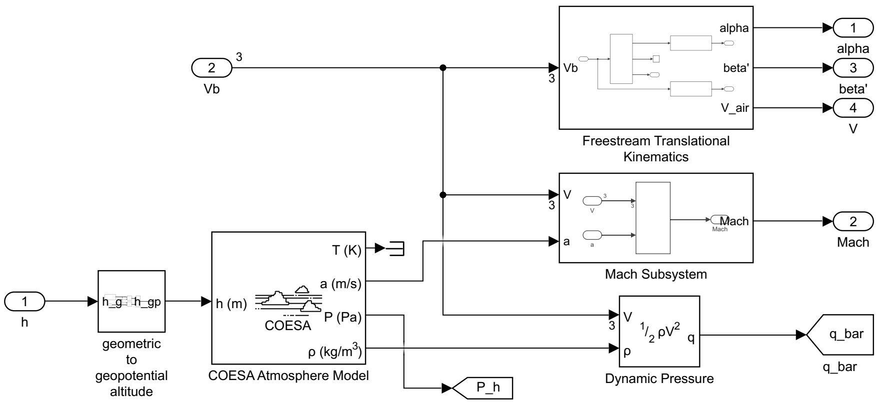

FIGURE 3.20: Environment subsystem.

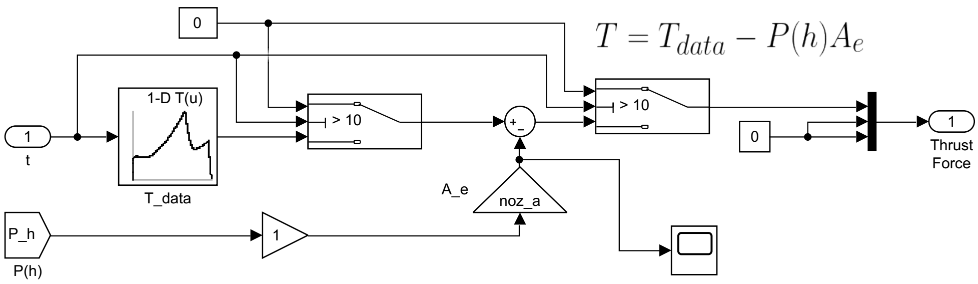

FIGURE 3.21: Thrust subsystem.

The block diagrams for Newton's law of gravitation are given in Fig. 3.22. The corresponding blocks for the gravitational force are shown Fig. 3.23 where the matrix rotation from the inertial to body frame is also demonstrated.

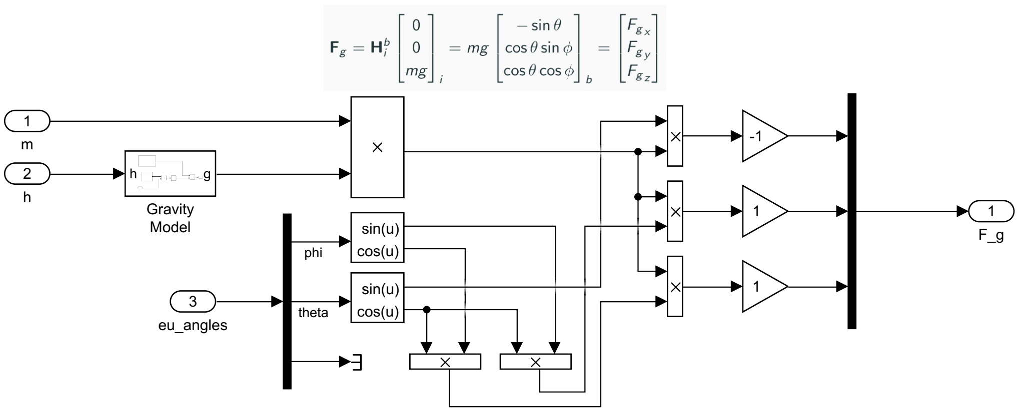

FIGURE 3.22: Gravitational force subsystem.

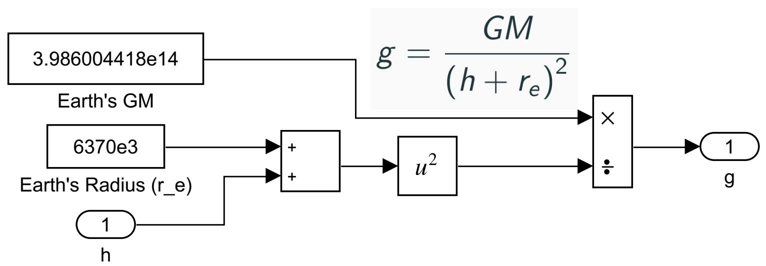

FIGURE 3.23: Block diagrams of the gravitational acceleration.

The aerodynamic coefficient calculations are divided into longitudinal (Fig. 3.24) and lateral-directional subsytems (Fig. 3.25).

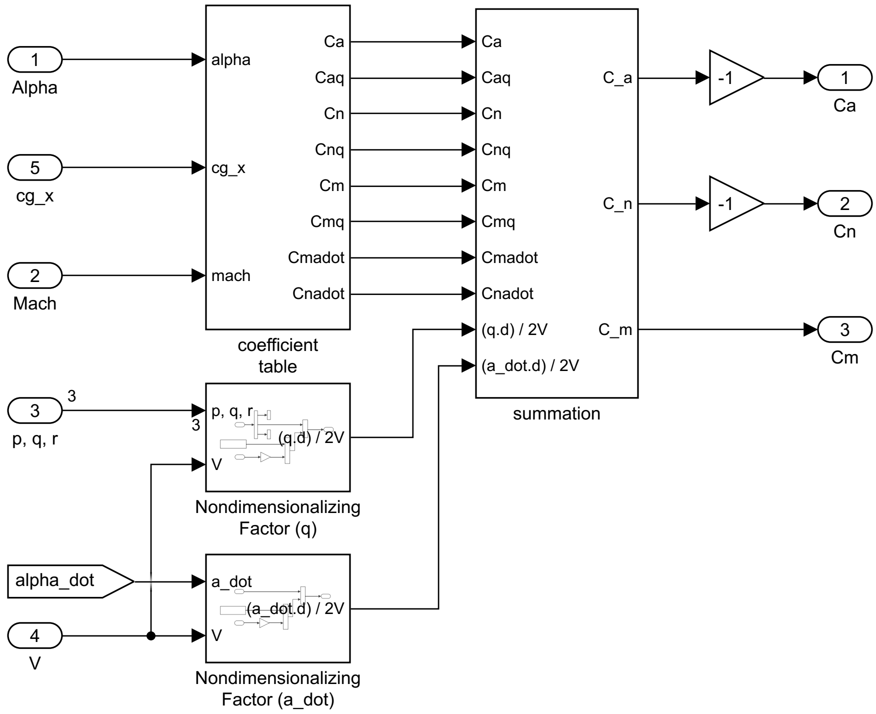

FIGURE 3.24: Longitudinal aerodynamic coefficients subsystem.

As shown in Fig. 3.26 and Fig. 3.27, the aerodynamic coefficients are presented by lookup tables and are functions of the angle of attack, Mach number, and the center of gravity position. The axial and normal force coefficients are multiplied by -1 (-1 gain block) due to the difference in body coordinate system definitions between Missile DATCOM (Fig. 3.6) and the 6DoF block (Fig. 2.10).

The contribution of the Coriolis moment is illustrated in Fig. 3.28. The mass and moments of inertia are modeled with lookup tables in the mass characteristics subsystem. Their time derivatives are given as a constant block since their values do not change over time except for the time of burnout (represented by a switch block in Fig. 3.29).

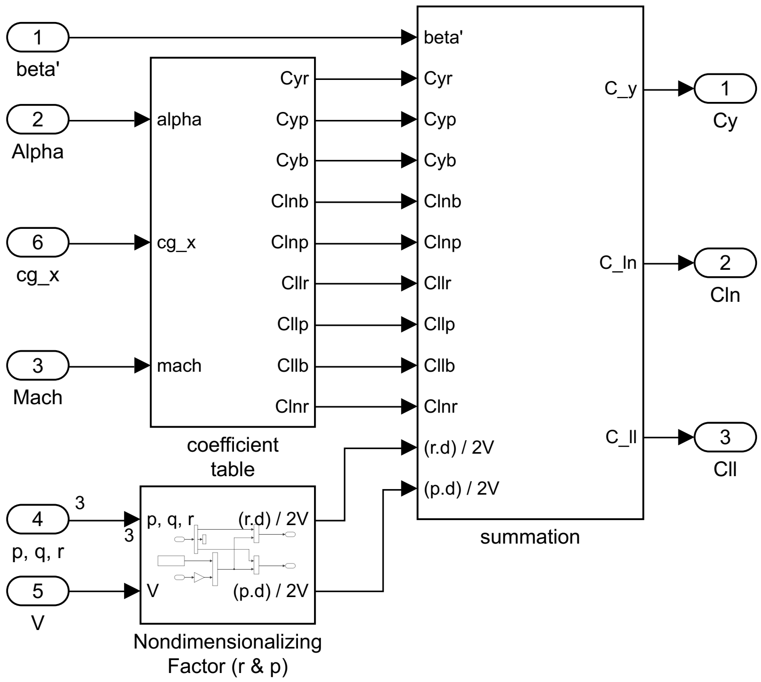

FIGURE 3.25: Lateral-directional aerodynamic coefficients subsystem.

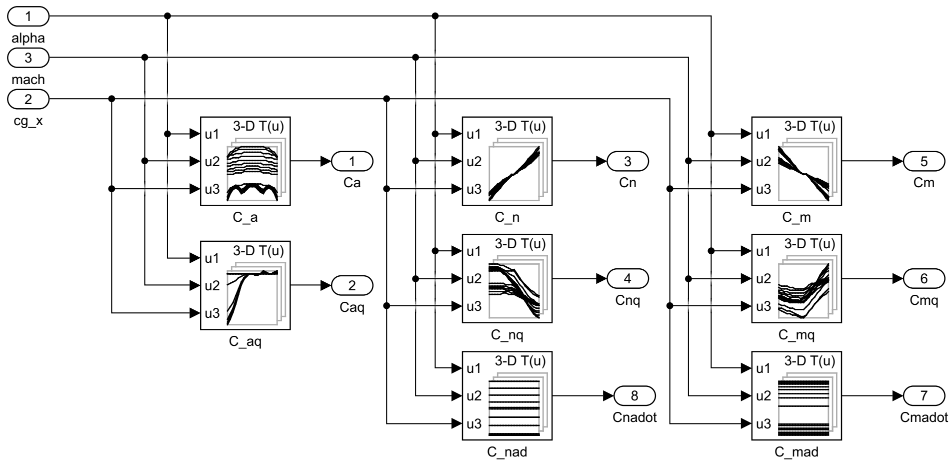

FIGURE 3.26: Longitudinal aerodynamic coefficients.

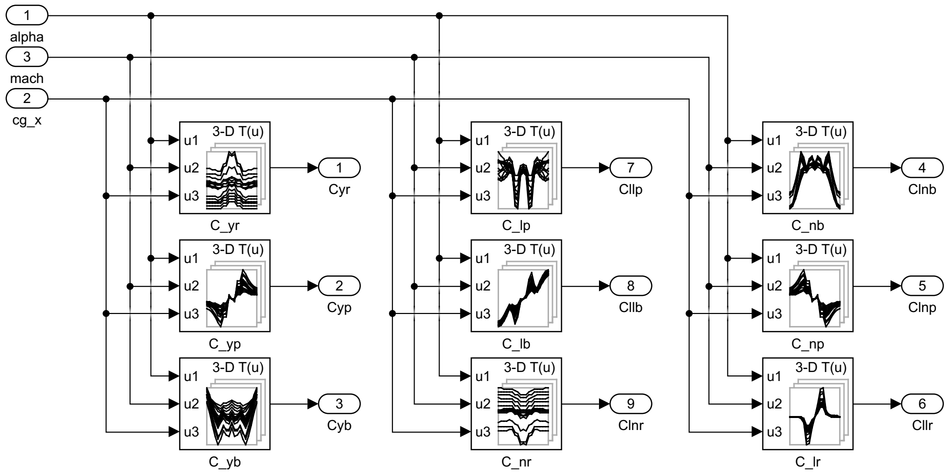

FIGURE 3.27: Lateral-directional aerodynamic coefficients.

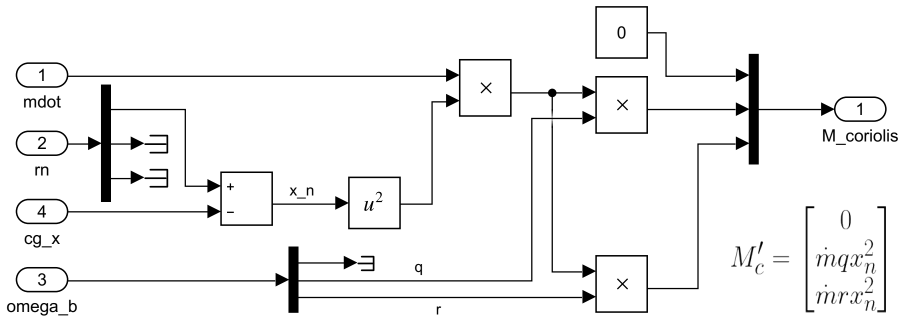

FIGURE 3.28: Coriolis moment subsystem.

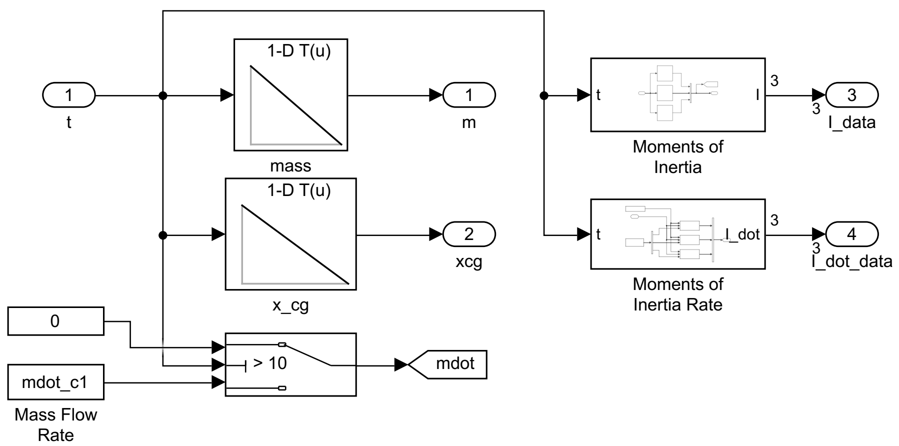

FIGURE 3.29: Mass characteristics subsystem.

3.4.2 MATLAB Scripts

In this section, the general ideas of the major scripts used in this thesis are going to be discussed. The full scripts are available in Appendix B.

DATCOM x_{cg} Iterator

As stated in Sec. 3.3, the aerodynamic coefficients from Missile DATCOM are only functions of the angle of attack and Mach number. Following the notions in Sec. 2.3.6, the aerodynamic coefficients are also functions of the center of gravity position. Therefore, these coefficients need to be modified to account for the movement of the center of gravity. The general workflow of the script is as follows:

1. Create Missile DATCOM input file (for005.dat);
2. Run Missile DATCOM;
3. Use MATLAB function datcomimport() to parse the output file (for006.dat);
4. Append the parsed output to an array;
5. Loop for the number of desired x_{cg} points;
6. Save the array to a MAT-file.

The resulting aerodynamic coefficients will be in the form of m-by-n-by-o matrices where m, n, and o are the number of data points of the angle of attack, Mach number, and the center of gravity, respectively. 10 center of gravity points will be used while the aerodynamic coefficients for the in-between center of gravity points will be linearly interpolated.

Rocket Data Initialization

The necessary variables used by the Simulink model are initialized using MATLAB scripts and saved to a MAT-file. Before every Simulink simulation, this MAT-file needs to be loaded to populate the MATLAB workspace. These scripts can be grouped into four categories:

- Aerodynamic coefficients: initialize the aerodynamic coefficients from the DATCOM x_{cg} iterator script;
- Mass profile: initialize and estimate the mass, moments of inertia, and x_{cg} ;
- Thrust profile: initialize thrust profile data from LAPAN that is stored in a MAT-file;
- Initial condition: specify initial conditions for the position, velocity, attitude, and attitude rates.

Monte Carlo Simulation

In this thesis, Monte Carlo simulations are performed by programmatically running the Simulink Model through a MATLAB script. The main objective of the Monte Carlo simulations is to analyze the change of the rocket's dynamics when exposed to moments of inertia uncertainty.

The uncertainty will only be applied to one of the moments of inertia per simulation. This way, the individual influences of each moment of inertia on the rocket's dynamics can be isolated and compared. The moments of inertia profiles under uncertainty are generated by the MATLAB script before every Simulink run. These profiles are formulated using two approaches:

- Constant Uncertainty

$$\begin{aligned} I_{rf} &= \mathcal{N}(I_n(0),\ \sigma_p I_n(0)) \\ I_{re} &= \mathcal{N}(I_n(t_b),\ \sigma_p I_n(t_b)) \\ \frac{dI_r}{dt} &= \frac{I_{re} - I_{rf}}{t_b} \\ I_r(t) &= I_{rf} + \frac{dI_r}{dt} t \end{aligned} \tag{3.1}$$

- Noise Uncertainty

$$\begin{aligned} I_r(t) &= \mathcal{N}(I_n(t),\ \sigma_p I_n(t)) \\ \frac{dI_r}{dt} &= \frac{I_r(t_b) - I_r(0)}{t_b} \end{aligned} \tag{3.2}$$

where

- $I_n(t) \triangleq$ Moments of inertia without uncertainty (nominal);
- $I_r(t) \triangleq$ Randomized moments of Inertia;
- I_{rf} and $I_{re} \triangleq$ Randomized moments of inertia at full and empty mass, respectively;
- $\mathcal{N}(\mu,\ \sigma) \triangleq$ Normal distribution function where μ and σ are the mean and the standard devitation, respectively;
- $\sigma_p \triangleq$ Standard deviation percentage multiplier;
- $t_b \triangleq$ Rocket motor burn time.

MATLAB's built-in function, normrnd(), is used to represent the normal distribution function $\mathcal{N}$. For both uncertainty types, the moments of inertia profile $I(t)$ and rate of moments of inertia $\frac{dI}{dt}$ under uncertainty are then mathematically defined by

$$\begin{aligned} I(t) &= \begin{cases} I_r(t), & \text{if } 0 < t \leq t_b \\ I_r(t_b), & \text{if } t > t_b \end{cases} \\ \frac{dI_r}{dt} &= \begin{cases} \frac{dI_r}{dt}, & \text{if } 0 < t \leq t_b \\ 0, & \text{if } t > t_b \end{cases} \end{aligned} \tag{3.3}$$

The noise profile is created by incrementally inputting each sample time (t_s $0 < t_s \leq t_b$) into $I_r(t)$ using the model's fixed time step t_{step} as the increment. Consequently, the noise frequency is constant and defined by

$$f_n = \frac{1}{t_{step}} \tag{3.4}$$

For the constant uncertainty, there are rare occasions where the randomized value for the dry moments inertia will be larger than the wet moments of inertia which is not realistic. Therefore, the randomising process is modified such that the script would re-roll the randomized values if the previous statement is detected.

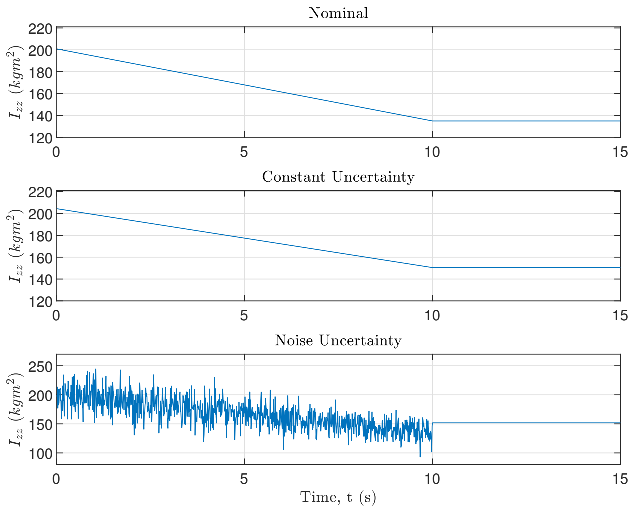

FIGURE 3.30: Comparison between various moments of inertia profiles.

In addition, the function rng('shuffle') will be used to produce a random seed based on the current time to make sure that the normal distribution function outputs different values at every runs. The comparison between the nominal profile, constant uncertainty, and noise uncertainty moments of inertia is shown in Fig. 3.30.

CHAPTER 4
RESULTS AND DISCUSSIONS

4.1 Overview

The simulation results will be divided into two categories:

- Nominal simulation: with disturbance but no uncertainty;
- Monte Carlo, uncertainty simulation: with disturbance and uncertainty.

As mentioned in Sec. 3.4.1, the wind disturbance will be in the form of a step function in sidewind velocity (v_w). The behavior of this step disturbance is characterized by:

- Starting step time: at $t = 5$ seconds;
- Step duration: 1 second;
- Step magnitude: 0, +1, +2, and +3 m/s

Therefore, there will be four nominal trajectories that will correspond to each of the wind disturbances.

The parameters for the initial conditions are shown in Tab. 4.1. The initial translational velocity is defined as the rocket's velocity just after leaving the launcher as illustrated in Fig. 4.1. The Simulink ODE solver is set to automatic for Simulink to choose with a fixed integration time step of 0.02 seconds. The simulation would stop automatically if the altitude goes below zero.

4.2 Nominal Simulations

The nominal rocket trajectories for all four wind disturbances are shown in Fig. 4.2. In absence of any wind disturbances, the rocket follows a parabolic trajectory

FIGURE 4.1: LAPAN RX-320 Rocket on its launcher (right) and right before leaving the launcher (left) (*Pusat Teknologi Roket*, 2022a).

State	Variable	Value	Unit
Position	$[x_e\ y_e\ z_e]$	[0 0 0]	m
Velocity	$[u_s\ v_s\ w_s]$	[20 0 0]	m/s
Attitude	$[\phi\ \theta\ \psi]$	[0 60 0]	deg
Angular rate	$[p\ q\ r]$	[0 0 0]	deg/s

TABLE 4.1: Initial conditions for all simulations.

without any displacements in the y-direction and achieved the largest maximum range, and consequently also the largest final x-displacement, of 23.178 km. The largest maximum altitude of 9.466 km and the largest final y-displacement of -257.78 m are achieved when the rocket encounters a +3 m/s wind disturbance.

As summarized in Tab. 4.2, with the increase of the wind disturbance magnitude, the maximum altitude increases while the maximum range and final x position decrease. However, the rocket's final y position does not necessarily follow a linear pattern that is governed by the direction and magnitude of the wind disturbance. A +3 m/s wind disturbance leads to a negative final y coordinate whilst a +1 m/s wind disturbance causes a positive and larger final displacement in y-direction than a +2 m/s wind disturbance.

The angle of attack trajectories under all wind disturbances exhibit a similar profile. For all trajectories, the maximum angle of attack of about +4.6 deg occurs right after the launch. In terms of the overall longitudinal stability, the rocket has a tendency to attain and maintain the angle of attack close to zero. A noticeable

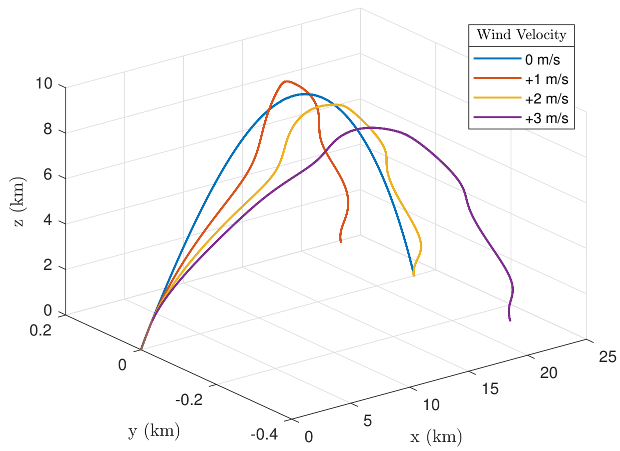

FIGURE 4.2: 3D-trajectory comparison between different wind disturbance magnitudes.

v_w	Max. R (km)	Max. H		Final x (km)	Final y (m)
		H (km)	t (s)		
0	23.178	9.355	44.600	23.178	0.000
+1	23.136	9.423	44.920	23.135	193.190
+2	23.108	9.450	44.880	23.108	-1.028
+3	23.083	9.466	44.840	23.082	-257.780

TABLE 4.2: Trajectory summary of the nominal simulation.

oscillation appears just before apogee in the form of a small and damped, long-period oscillation as depicted in Fig. 4.3.

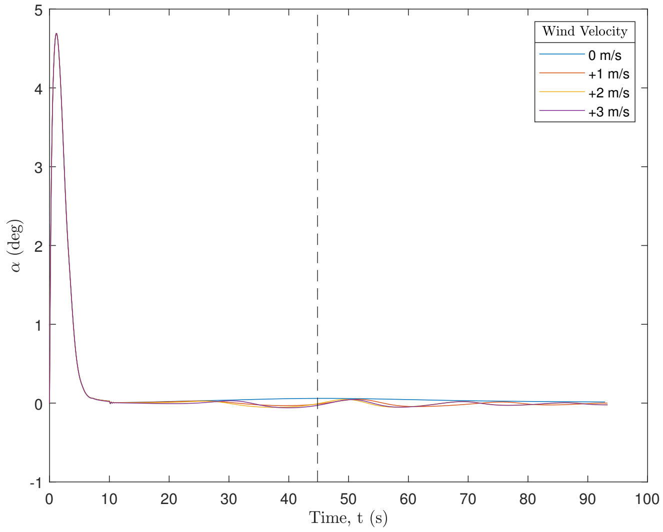

FIGURE 4.3: Angle of attack comparison between different wind disturbance magnitudes, dashed line represents mean apogee time.

As shown in Fig. 4.4, the sideslip angle will remain zero without any wind disturbances. As soon as a wind disturbance is introduced, a short-period sideslip angle oscillation begins. The magnitude of this oscillation increases with wind disturbance. All sideslip angle trajectories follow an identical pattern until right before apogee at which point the oscillation for +1 m/s wind disturbance flips and drifts away in a different direction than the rest. All sideslip trajectories do not suggest a convergence to a single value. Although not showing a similar sign of stability like the angle of attack, the rocket is able to keep the sideslip angles to small values between ± 1 deg throughout the flight for all wind disturbances.

4.3 Simulation with Uncertainty

4.3.1 Uncertainty Overview

The results of the Monte Carlo simulations are used to compare the effects of each of the moments of inertia and their uncertainty types. In total, there are 12 different

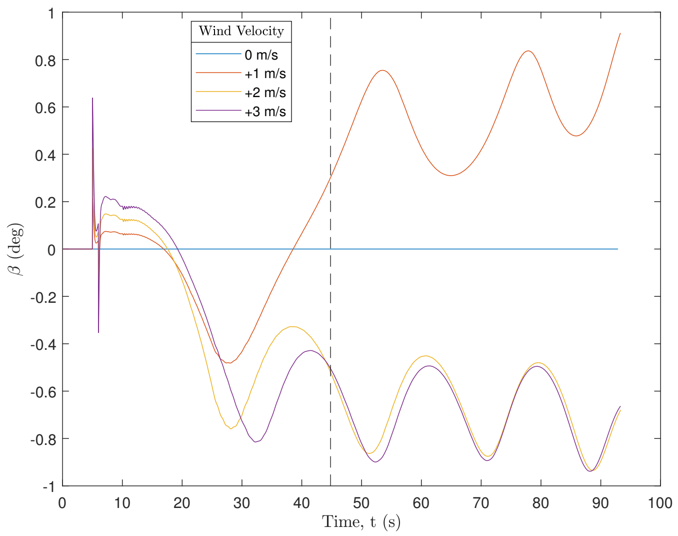

FIGURE 4.4: Sideslip angle comparison between different wind disturbance magnitudes, dashed line represents mean apogee time.

cases which correspond to the combinations of:

- 3 percentage standard deviations σ_p: 3%, 6%, and 10%;
- 4 sidewind (v_w) disturbances: 0, +1, +2, and +3 m/s.

Taking into account the three moments of inertia (I_{xx}, I_{yy}, I_{zz}) and two uncertainty types (constant and noise), there will be a total of 72 different subcases where each of these subcases will be run for 500 times.

The analysis will be focused on the distribution of the final position, maximum range, and maximum altitude using kernel density estimations and normal distribution parameterizations. The kernel density estimation for univariate and bivariate distribution is done in Python using the Seaborn library (*Seaborn Documentation*, 2022). The estimation utilizes Gaussian kernels and the bandwidth is selected using Scott's rule. The stability of the rocket will also be briefly investigated by comparing the angle of attack and sideslip angle trajectory profiles.

4.3.2 Special Case: Uncertainty with v_w = 0 m/s

The simulations with 0 m/s sidewind disturbance can be treated as a special case where the rocket is locked in the longitudinal motions only. Considering the initial conditions stated in Tab. 4.1, the lateral-directional equations from Eq. 2.50 and Eq. 2.51 can be rewritten for the first simulation time step as

$$\begin{aligned} m\dot{v} &= q_\infty S C_Y \\ I_{xx}\dot{p} &= q_\infty S l_{ref} C_l \\ I_{zz}\dot{r} &= q_\infty S l_{ref} C_n \end{aligned} \tag{4.1}$$

Due to the rocket's symmetry, the lateral-directional aerodynamic coefficients will be zero at zero sideslip angle. Referring to Sec. 2.3.1, the sideslip angle will remain at zero value since in this particular case both v_s and v_w are set to zero. This is exactly the condition depicted in Fig. 4.4 for the trajectory without any sidewind disturbances.

Thus, Eq. 4.2 can be further rewritten to

$$\begin{aligned} \dot{v} &= 0 \\ \dot{p} &= 0 \\ \dot{r} &= 0 \end{aligned} \tag{4.2}$$

In other words, as long as there is no sidewind disturbance, no value of I_{xx} and I_{zz} will be able to change the rocket's dynamics and no I_{yy} values will create any change for the lateral-directional motions. Therefore, the analysis for this case can be reduced where the primary focus will be the effects of I_{yy} uncertainty to the longitudinal motions of the rocket without any sidewind disturbances.

The longitudinal lock can further be seen from Fig. 4.5 where the resulting final positions are shown to lie solely in the x-axis. The distributions of the maximum range are shown in Fig. 4.6. In this case, the maximum range exactly represents the final x position. Compared to the density estimation for the maximum altitude in Fig. 4.7, the distribution of the maximum range does not completely resemble a normal distribution.

As displayed in Tab. 4.3, the averages for both uncertainty types differ only slightly from the nominal result with the order of centimeters,. For both noise and constant uncertainty, the spread of the final x positions grows larger as the

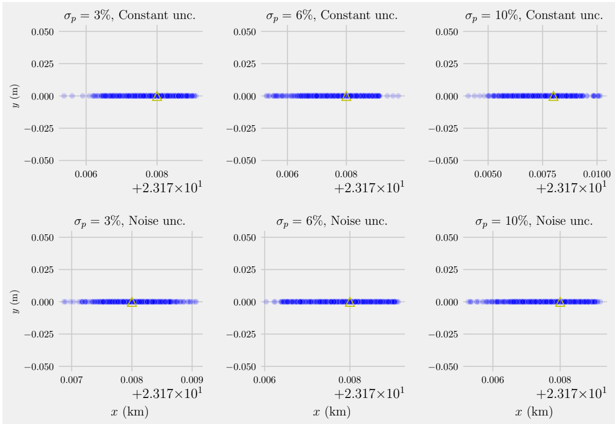

FIGURE 4.5: Final xy position results for I_{yy} uncertainty with no wind disturbance, yellow triangle indicates the nominal xy.

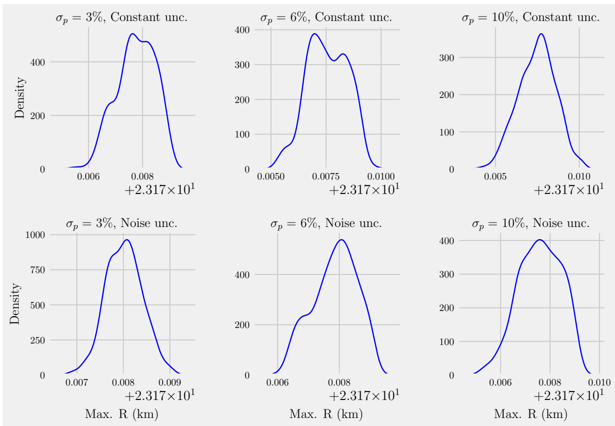

FIGURE 4.6: Maximum range KDE plot for I_{yy} uncertainty with no wind disturbance.

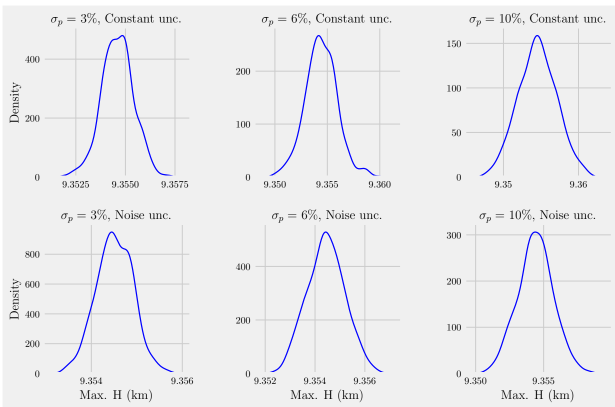

FIGURE 4.7: Maximum altitude KDE plot for I_{yy} uncertainty with no wind disturbance.

standard deviation of the uncertainty gets larger. Although not that striking, the constant uncertainty produces a larger spread for the maximum range and altitude.

Indicator	Mean and std. dev.	Nominal Sim.	I_{yy}, σ_p (%)					
			Constant Unc.			Noise Unc.		
			3	6	10	3	6	10
Max. R	μ (km)	23.1780	23.1778	23.1776	23.1775	23.1780	23.1779	23.1776
	σ (m)	0	0.7	0.9	1.1	0.4	0.7	0.9
Max. H	μ (km)	9.3545	9.3546	9.3544	9.3545	9.3545	9.3544	9.3544
	σ (m)	0	0.8	1.5	2.5	0.4	0.7	1.3

TABLE 4.3: Average and standard deviation summary for I_{yy} uncertainty with $v_w = 0$ m/s.

All angle of attack trajectories shown in Fig. 4.8 resemble a similar stability profile to the nominal angle of attack trajectory. The rocket tends to minimize the angle of attack close to zero while having the maximum angle of attack of about +4.7 deg right after launch.

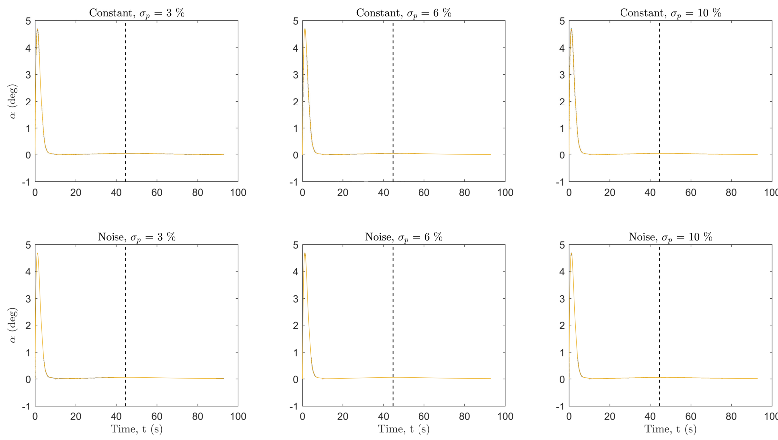

FIGURE 4.8: Angle of attack comparison for I_{yy} uncertainty with $v_w = 0$ m/s, dashed line represents approximated apogee timings.

4.3.3 Case 1: Constant Unc. and $v_w = +1$ m/s

For all distributions, the nominal impact point is shown to be inside the highest probability density areas as displayed in Fig. 4.9. Similar impact point clusters

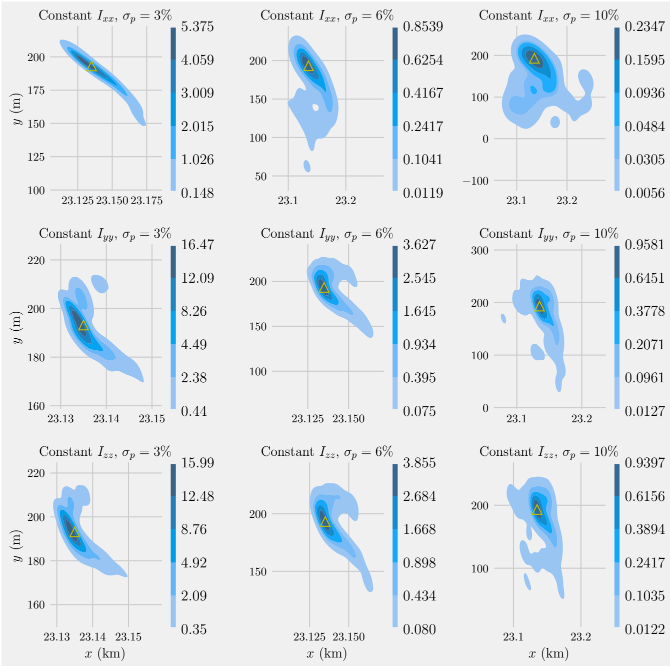

FIGURE 4.9: Final xy position results for constant unc. with $v_w =$ +1 m/s, yellow triangle indicates the nominal final xy.

can be seen from I_{yy} and I_{zz} uncertainties. This can further be supported by their univariate probability density estimates shown in Fig. 4.10 and Fig. 4.11.

Tab. 4.4 indicates that the mean and standard deviations of all indicators for I_{yy} and I_{zz} uncertainties with respect to each σ_p have similar values. Compared to the nominal value, the final x averages across all uncertainties differ only by a small amount with the largest deviation of (+)6 meters occurring on 10% I_{xx} and I_{zz} uncertainty. The same thing can also be said for the maximum altitude with the largest deviation of (+)4 meters occurring on 10% I_{xx} uncertainty. As illustrated in Fig. 4.12, the distributions of the maximum altitude show a close resemblance to a normal distribution.

On contrary, the increase in σ_p leads to the decrease of the averages of the final y value. This decrease is more evident with the I_{xx} uncertainties. The standard deviation for all of the indicators increases as σ_p increases. Relative to the I_{yy} and I_{zz} uncertainties, the uncertainties in I_{xx} create the largest standard deviations in all of the indicators; almost doubling the values with the same σ_p uncertainty.

All of the angle of attack trajectories follow a stability profile tendency similar

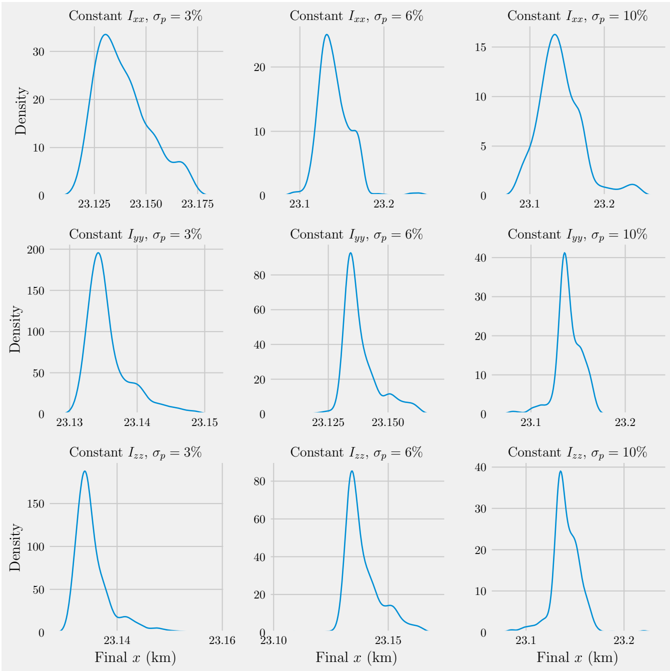

FIGURE 4.10: Final x density estimates from constant unc. and v_w = +1 m/s case.

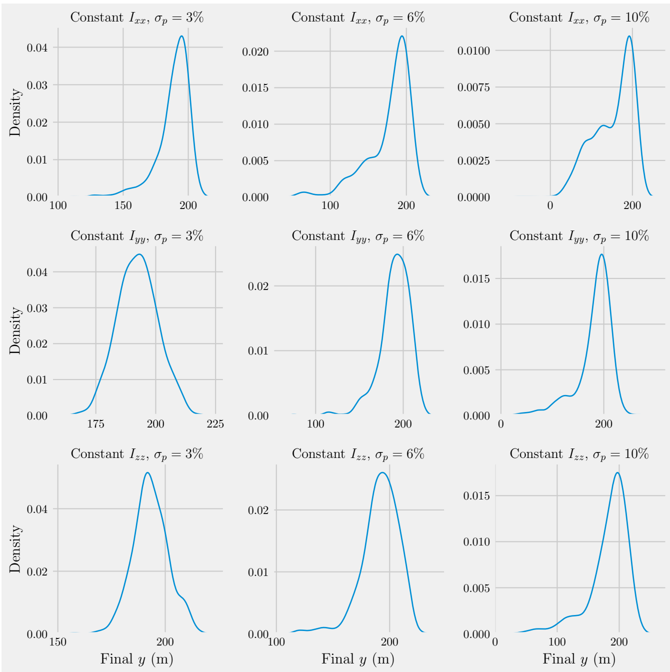

FIGURE 4.11: Final y density estimates from constant unc. and v_w = +1 m/s case.

Indicator	Mean and std. dev.	Nominal Sim.	Constant Uncertainty								
			I_{xx}, σ_p (%)			I_{yy}, σ_p (%)			I_{zz}, σ_p (%)		
			3	6	10	3	6	10	3	6	10
Final x	μ (km)	23.135	23.140	23.140	23.141	23.136	23.140	23.140	23.135	23.140	23.141
	σ (m)	0	13	19	30	3	8	15	4	8	14
Final y	μ (m)	193	189	178	152	192	190	183	193	192	183
	σ (m)	0	13	29	50	8	18	34	8	17	32
Max. R	μ (km)	23.136	23.140	23.142	23.141	23.136	23.139	23.141	23.136	23.140	23.141
	σ (m)	0	13	19	30	3	7	14	4	8	14
Max. H	μ (km)	9.423	9.423	9.425	9.427	9.423	9.423	9.423	9.423	9.424	9.423
	σ (m)	0	11	20	30	3	5	10	3	5	19

TABLE 4.4: Average and standard deviation summary from constant unc. and $v_w = +1$ m/s case.

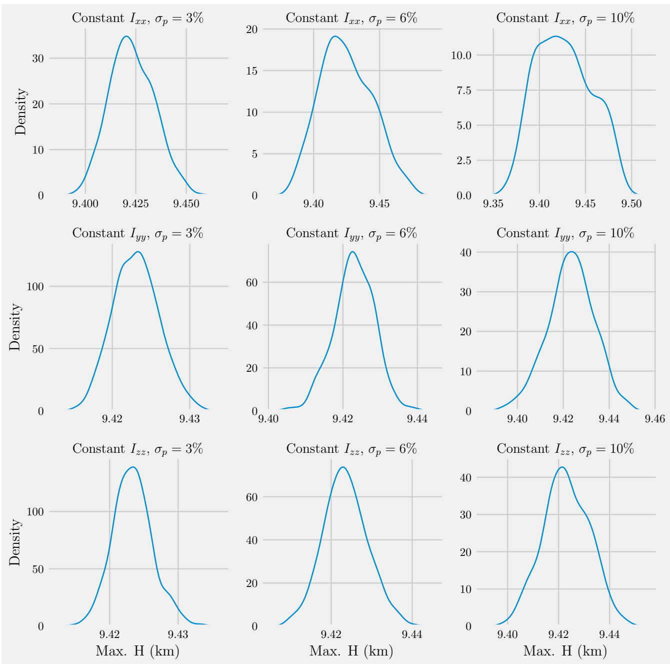

FIGURE 4.12: Max. altitude density estimates from constant unc. and $v_w = +1$ m/s case.

to the nominal simulation while having the approximate maximum angle of attack of about +4.7 deg right after launch as presented in Fig. 4.13. Thereafter, the angle of attack is maintained close to zero. For all of the uncertainties, there is a slight noticeable oscillation after reaching apogee.

As can be seen in Fig. 4.14, the change in the sideslip angle's oscillation phase and amplitude grows in magnitude as σ_p increases. Particularly with $\sigma_p = 10\%$, some trajectory outliers can be identified as their trajectories flip around apogee.

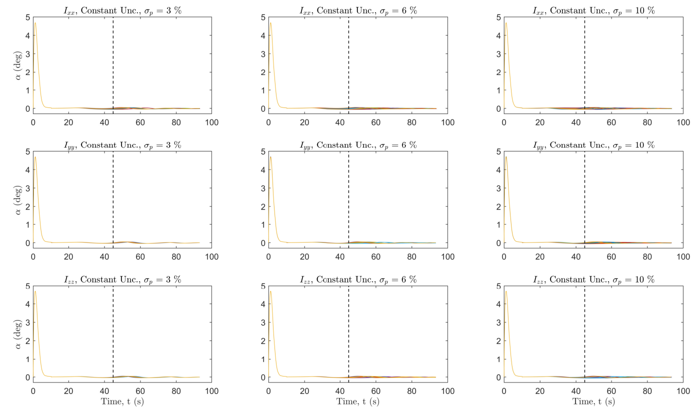

FIGURE 4.13: Angle of attack comparison from constant unc. and $v_w = +1$ m/s case, dashed line represents the approximated apogee timings.

Across moments of inertia, the trajectories with I_{yy} and I_{zz} uncertainties show a similar profile while the variations in the oscillation phase and amplitude is even more distinct with the uncertainty in I_{xx}. For all trajectories, no clear sign of asymptotic stability is shown. However, the sideslip angle is kept between ± 1 deg throughout the whole flight.

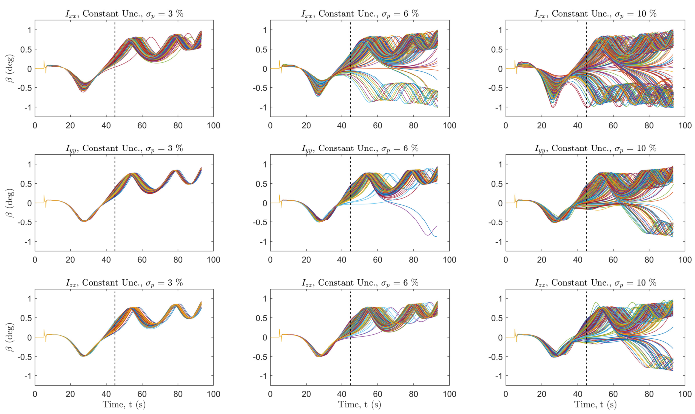

FIGURE 4.14: Sideslip angle comparison from constant unc. and $v_w = +1$ m/s case, dashed line represents approximated apogee timings.

4.3.4 Case 2: Constant Unc. and $v_w = +2$ m/s

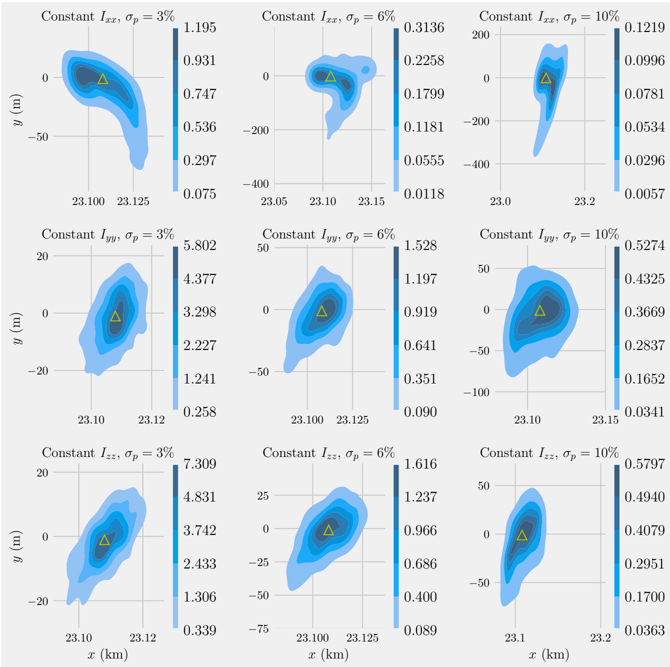

FIGURE 4.15: Final xy position results for constant unc. with v_w = +2 m/s, yellow triangle indicates the nominal final xy.

The nominal impact point is shown to be inside the highest probability density areas except for the I_{xx} uncertainties as displayed in Fig. 4.15. The multi-modalities in the final x density for I_{xx} uncertainties can better be seen from Fig. 4.16. However, there is no multi-modality observed for the final y density as shown in Fig. 4.17.

Tab. 4.5 indicates that the mean and standard deviations of all indicators for I_{yy} and I_{zz} uncertainties with respect to each σ_p display similar values. Compared to the nominal value, the final x averages across all uncertainties differ only by a small amount with the largest deviation of (+)7 meters occurring on 6% and 10% I_{xx} uncertainties. The same thing can also be said for the maximum altitude with the largest deviation of (-)3 meters occurring on 10% I_{xx} uncertainty. As illustrated in Fig. 4.18, the distributions of the maximum altitude show a resemblance to a normal distribution.

On the contrary, the increase in σ_p leads to the decrease of the averages of the final y value. This decrease is more evident with the I_{xx} uncertainties. The

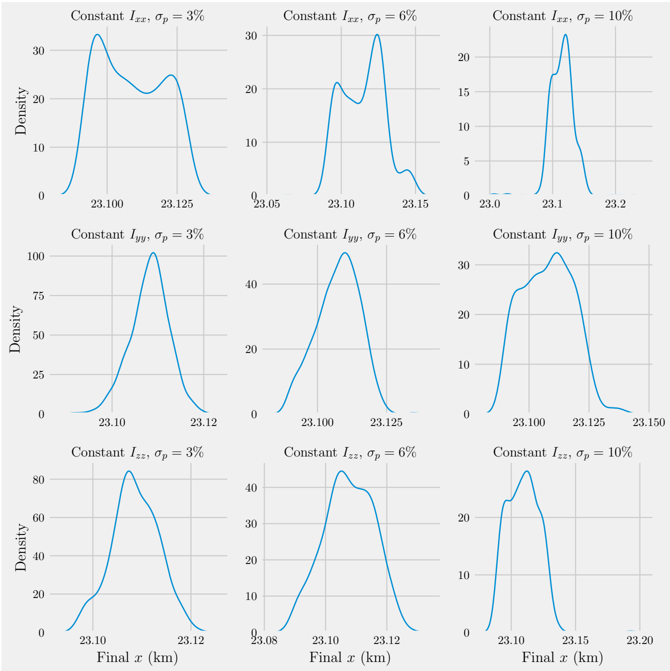

FIGURE 4.16: Final x density estimates from constant unc. and v_w = +2 m/s case.

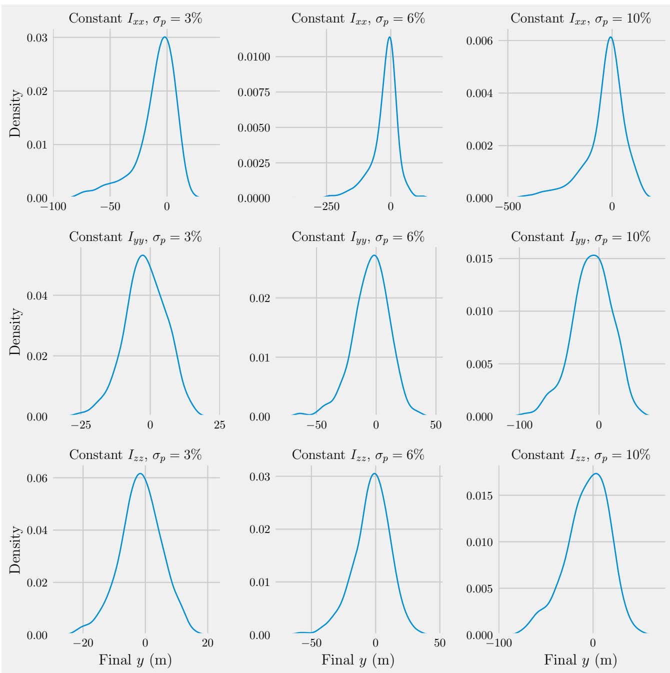

FIGURE 4.17: Final y density estimates from constant unc. and v_w = +2 m/s case.

Indicator	Mean and std. dev.	Nominal Sim.	Constant Uncertainty								
			I_{xx}, σ_p (%)			I_{yy}, σ_p (%)			I_{zz}, σ_p (%)		
			3	6	10	3	6	10	3	6	10
Final x	μ (km)	23.108	23.109	23.115	23.115	23.108	23.107	23.108	23.109	23.108	23.109
	σ (m)	0	12	14	20	4	8	10	5	8	12
Final y	μ (m)	-1	-10	-24	-32	-2	-5	-9	-2	-3	-6
	σ (m)	0	18	54	95	7	15	25	7	14	23
Max. R	μ (km)	23.108	23.109	23.115	23.115	23.108	23.107	23.108	23.109	23.108	23.109
	σ (m)	0	12	14	19	4	8	10	5	8	12
Max. H	μ (km)	9.450	9.449	9.448	9.447	9.449	9.449	9.449	9.450	9.450	9.450
	σ (m)	0	1	5	17	2	3	6	1	2	4

TABLE 4.5: Average and standard deviation summary from constant unc. and $v_w = +2$ m/s case.

standard deviation for all of the indicators increases as σ_p increases. Relative to the I_{yy} and I_{zz} uncertainties, the standard deviations of I_{xx} uncertainties almost have double the values with the same σ_p uncertainty for all indicators except for the final y values where it is about triple the values.

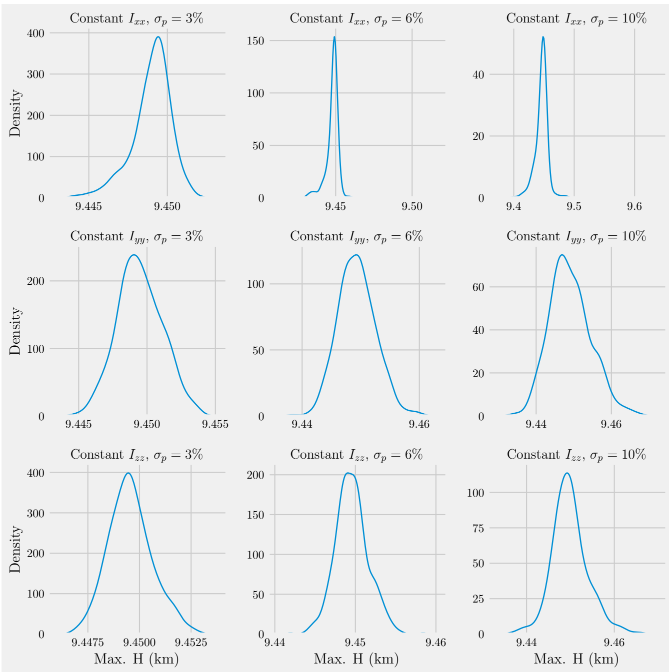

FIGURE 4.18: Max. altitude density estimates from constant unc. and $v_w = +2$ m/s case.

All angle of attack trajectories show a stability tendency similar to the nominal simulation. The approximate maximum angle of attack of about +4.7 deg right after launch as presented in Fig. 4.19. The angle of attack trajectories are shown to be close to zero for the rest of the flight. For all of the uncertainties, a slight oscillation is noticeable after reaching apogee.

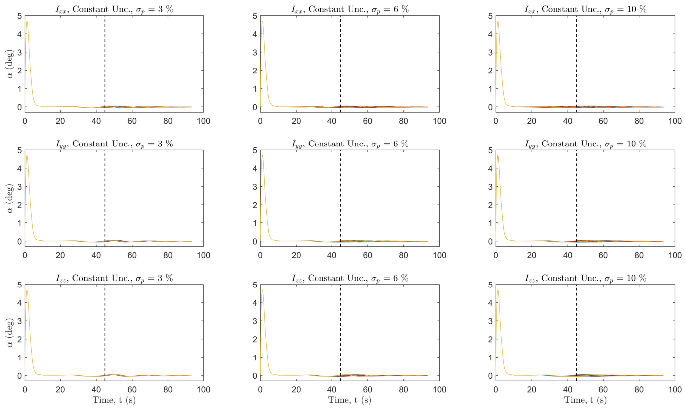

FIGURE 4.19: Angle of attack comparison from constant unc. and v_w = +2 m/s case, dashed line represents the approximated apogee timings.

It can be seen from Fig. 4.20 that for the sideslip trajectories the change in the oscillation phase and amplitude grows in magnitude as σ_p increases. Particularly with $\sigma_p = 10\%$, some trajectory outliers can be identified as their trajectories drift to the positive region around apogee. The outliers are more profound with the I_{xx} uncertainty. Across moments of inertia, the trajectories with I_{yy} and I_{zz} uncertainties share similar profiles. For all trajectories, no clear sign of asymptotic stability is shown. However, the sideslip angle is kept between -1 deg $< \beta <$ 1 deg throughout the whole flight.

4.3.5 Case 3: Constant Unc. and $v_w = +3$ m/s

For all distributions, the nominal impact point is shown to be inside the highest probability density areas as displayed in Fig. 4.21. As shown in Fig. 4.22 and Fig. 4.23, the distribution of the impact points with I_{xx} uncertainties display a sign of bimodality as σ_p increases. The univariate density estimates suggest that the impact points of I_{yy} and $_{zz}$ uncertainties share similar profiles and are normally

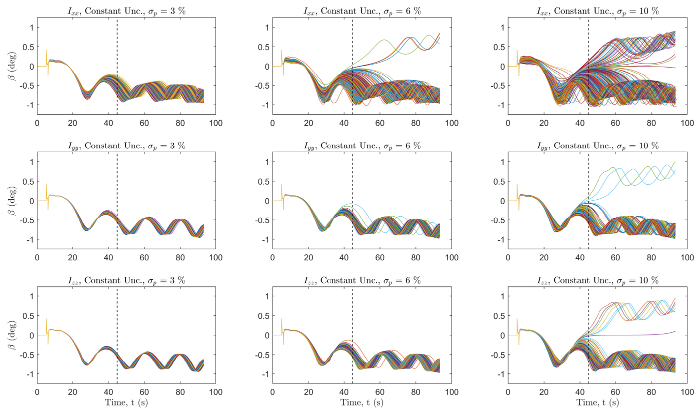

FIGURE 4.20: Sideslip angle comparison from constant unc. and v_w = +2 m/s case, dashed line represents approximated apogee timings.

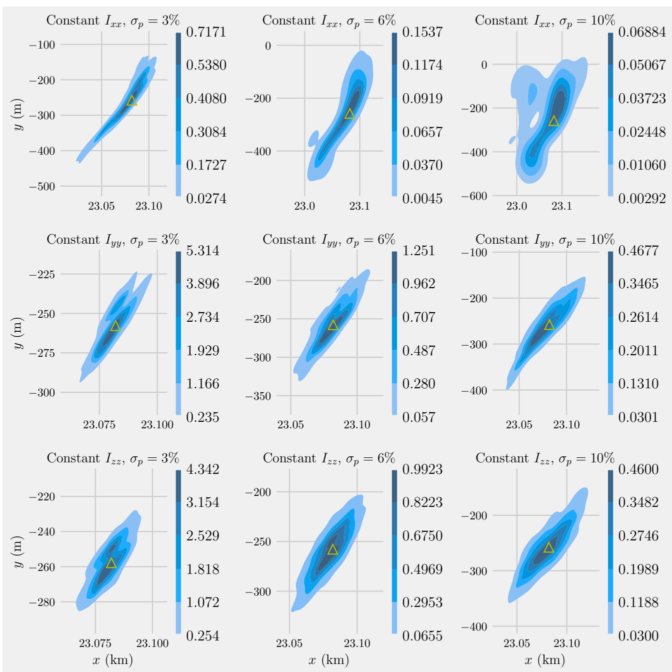

FIGURE 4.21: Final xy position results for constant unc. with v_w = +3 m/s, yellow triangle indicates the nominal final xy.

distributed. As illustrated in Fig. 4.24, all distributions of the maximum altitude show a close resemblance to a normal distribution.

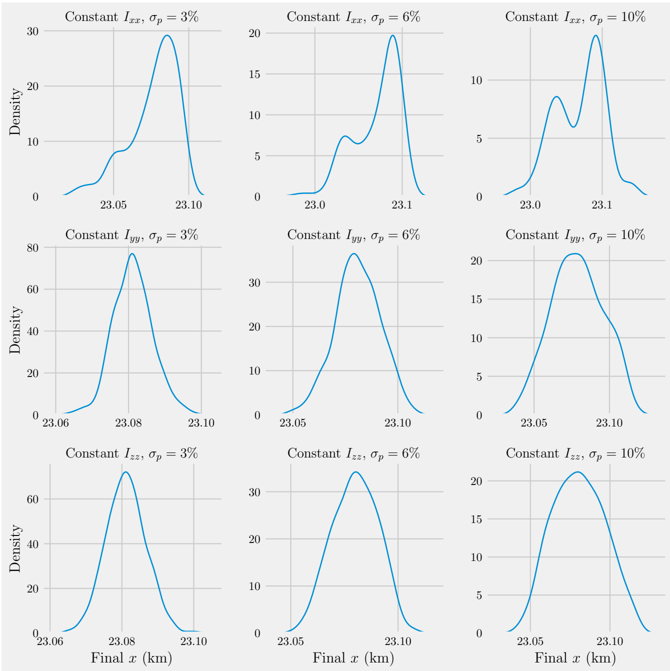

FIGURE 4.22: Final x density estimates from constant unc. and v_w = +3 m/s case.

Tab. 4.6 also indicates that the mean and standard deviations of all indicators for I_{yy} and I_{zz} uncertainties with respect to each σ_p display similar values. All indicators' averages from I_{yy} and I_{zz} uncertainties differ only by a small amount. In contrast, the I_{xx} uncertainties create the largest average difference on all of the indicators.

The increase in σ_p leads to the decrease of the averages of the final y value. This decrease is more evident with the I_{xx} uncertainties. The standard deviation for all of the indicators increases as σ_p increases. Relative to the I_{yy} and I_{zz} uncertainties, the uncertainties in I_{xx} create the largest standard deviations in all of the indicators; about 2 times as much on the final x, 4 times on the final y, and 8 times on the maximum altitude.

All angle of attack trajectories follow a stability profile tendency similar to the nominal simulation while having the approximate maximum angle of attack of about +4.7 deg right after launch as presented in Fig. 4.25. Thereafter, the angle

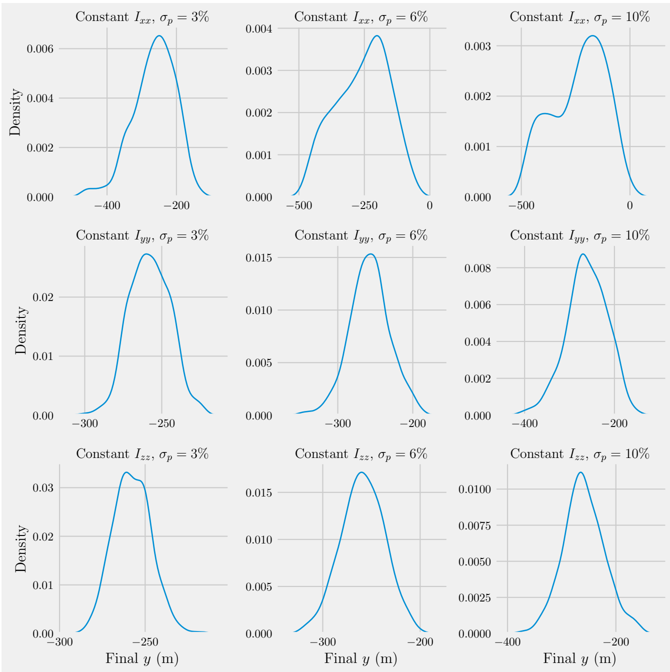

FIGURE 4.23: Final y density estimates from constant unc. and v_w = +3 m/s case.

Indicator	Mean and std. dev.	Nominal Sim.	Constant Uncertainty								
			I_{xx}, σ_p (%)			I_{yy}, σ_p (%)			I_{zz}, σ_p (%)		
			3	6	10	3	6	10	3	6	10
Final x	μ (km)	23.082	23.076	23.071	23.069	23.081	23.081	23.079	23.081	23.080	23.080
	σ (m)	0	16	27	34	5	11	17	6	11	16
Final y	μ (m)	-258	-264	-258	-234	-258	-258	-261	-258	-259	-259
	σ (m)	0	61	100	123	13	27	45	11	22	38
Max. R	μ (km)	23.083	23.078	23.073	23.070	23.083	23.082	23.080	23.083	23.081	23.082
	σ (m)	0	16	26	33	5	10	17	5	10	16
Max. H	μ (km)	9.466	9.469	9.478	9.488	9.466	9.466	9.466	9.465	9.466	9.466
	σ (m)	0	16	41	53	2	4	7	2	4	7

TABLE 4.6: Average and standard deviation summary from constant unc. and v_w = +3 m/s case.

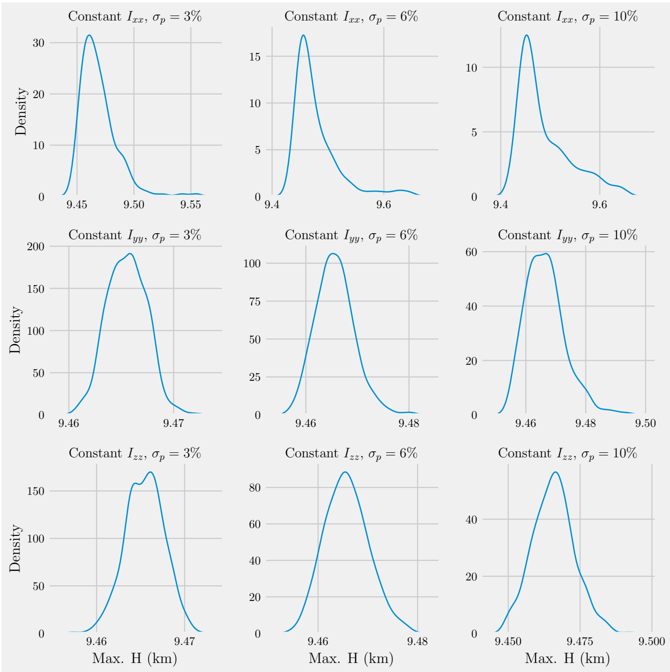

FIGURE 4.24: Max. altitude density estimates from constant unc. and $v_w = +3$ m/s case.

of attack is maintained close to zero. For all of the uncertainties, there is a slight noticeable oscillation after reaching apogee.

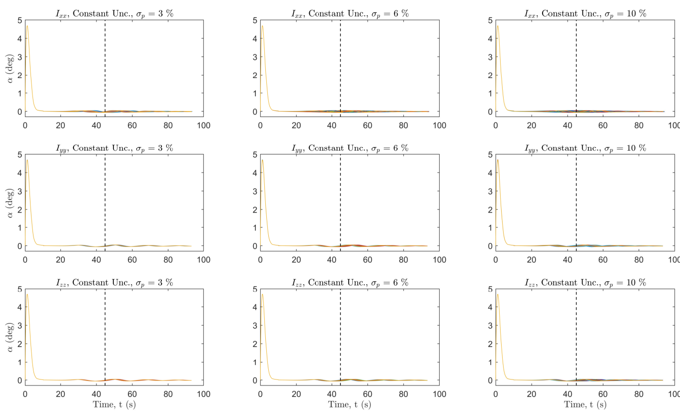

FIGURE 4.25: Angle of attack comparison from constant unc. and $v_w = +3$ m/s case, dashed line represents the approximated apogee timings.

As can be seen in Fig. 4.26 that for the sideslip angle trajectories the change in the oscillation phase and amplitude grows in magnitude as σ_p increases. Particularly for 6% and 10% I_{xx} uncertainty, some trajectory outliers can be identified as their trajectories flip to the positive region approximately at time $t = 20$ s. The number of outliers grows with σ_p. Across moments of inertia, the trajectories with I_{yy} and I_{zz} uncertainties show a similar profile while the variations in the oscillation phase and amplitude are even more distinct with the uncertainty in I_{xx}. For all trajectories, no clear sign of asymptotic stability is shown. However, the sideslip angle is kept between -1 deg < β < 1 deg throughout the whole flight.

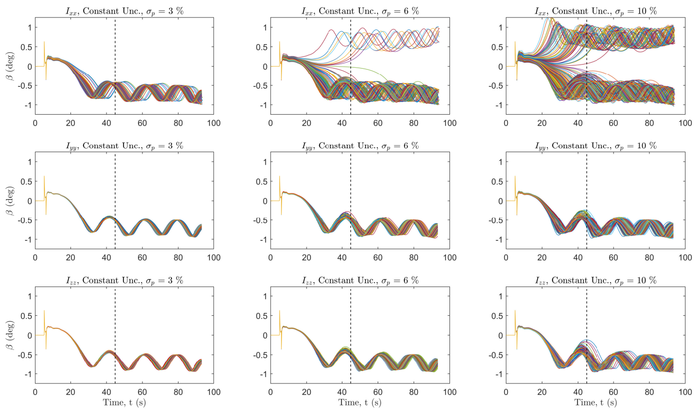

FIGURE 4.26: Sideslip angle comparison from constant unc. and $v_w = +3$ m/s case, dashed line represents approximated apogee timings.

4.3.6 Case 4: Noise Unc. and $v_w = +1$ m/s

Over all distributions, the nominal impact point is shown to be located in the highest probability density areas as shown in Fig. 4.27. Impact points for I_{yy} and I_{zz} uncertainties show a similar cluster with the same σ_p values. Their univariate probability density estimates further supported the previous statement as shown in Fig. 4.28 and Fig. 4.29.

From Tab. 4.7 it is also evident that across the same σ_p the mean and standard deviations of all indicators for I_{yy} and I_{zz} uncertainties have similar values. Compared to the nominal value, the final x averages across all uncertainties differ only by a small amount with the largest deviation of (+)6 meters occurring on 10% I_{zz}

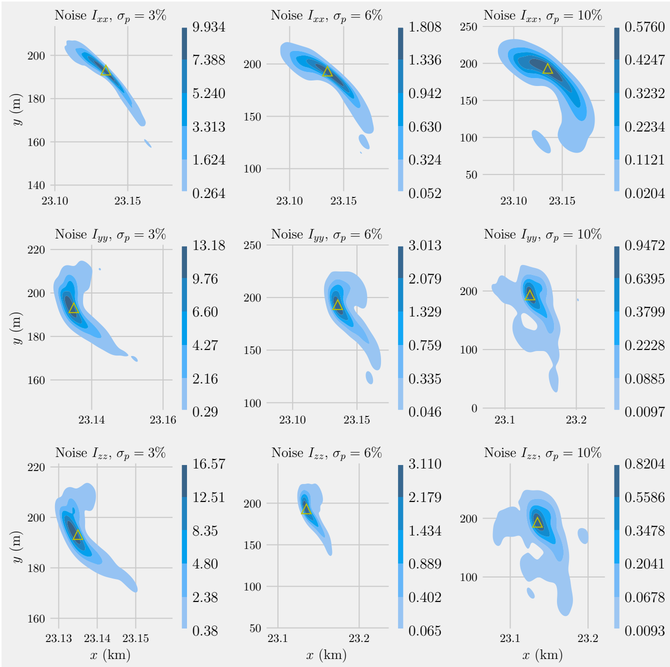

FIGURE 4.27: Final xy position results for noise unc. with v_w = +1 m/s, yellow triangle indicates the nominal final xy.

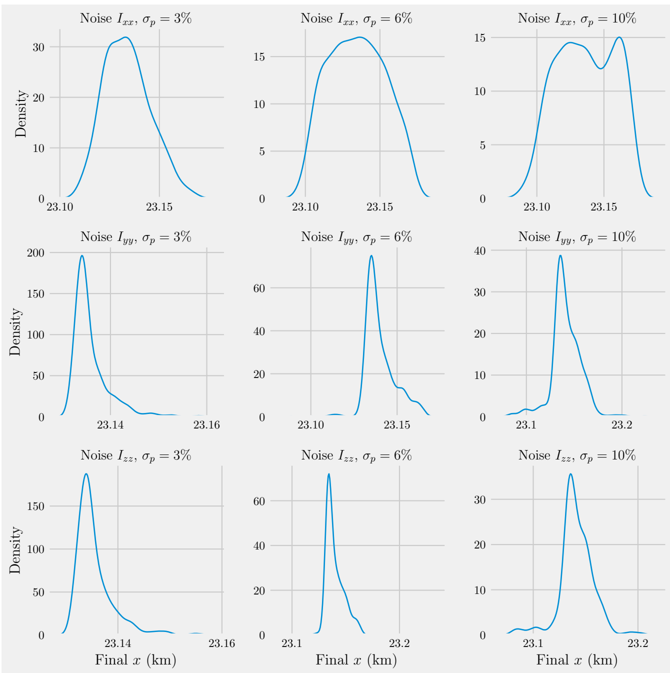

FIGURE 4.28: Final x density estimates from noise unc. and v_w = +1 m/s case.

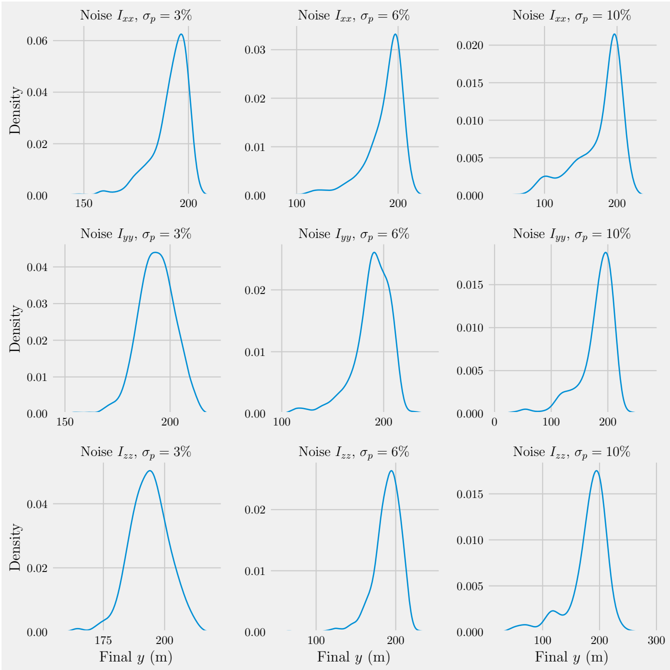

FIGURE 4.29: Final y density estimates from noise unc. and $v_w = +1$ m/s case.

uncertainty. The same thing can also be said for the maximum altitude with the largest deviation of (+)4 meters occurring on 10% I_{xx} uncertainty. As illustrated in Fig. 4.30, the distributions of the maximum altitude show a close resemblance to a normal distribution.

Indicator	Mean and std. dev.	Nominal Sim.	Noise Uncertainty								
			I_{xx}, σ_p (%)			I_{yy}, σ_p (%)			I_{zz}, σ_p (%)		
			3	6	10	3	6	10	3	6	10
Final x	μ (km)	23.135	23.134	23.130	23.137	23.136	23.140	23.141	23.135	23.140	23.141
	σ (m)	0	12	19	21	4	9	16	4	9	16
Final y	μ (m)	193	192	187	176	194	189	181	194	189	181
	σ (m)	0	9	19	32	9	18	32	8	17	34
Max. R	μ (km)	23.136	23.135	23.135	23.137	23.137	23.141	23.142	23.136	23.141	23.142
	σ (m)	0	12	19	21	4	9	16	4	9	16
Max. H	μ (km)	9.423	9.424	9.426	9.427	9.424	9.423	9.423	9.424	9.423	9.423
	σ (m)	0	5	12	19	4	7	11	3	6	11

TABLE 4.7: Average and standard deviation summary from noise unc. and $v_w = +1$ m/s case.

Conversely, the increase in σ_p leads to the decrease of the averages of the final y value. This decrease is more noticeable with the I_{xx} uncertainties. The standard deviation for all of the indicators increases as σ_p increases. Relative to the I_{yy} and I_{zz} uncertainties, the uncertainties in I_{xx} create the largest standard deviations in all of the indicators except for the final y. With the same σ_p, the standard deviations of the final y coordinate across different moments of inertia have approximately the same values.

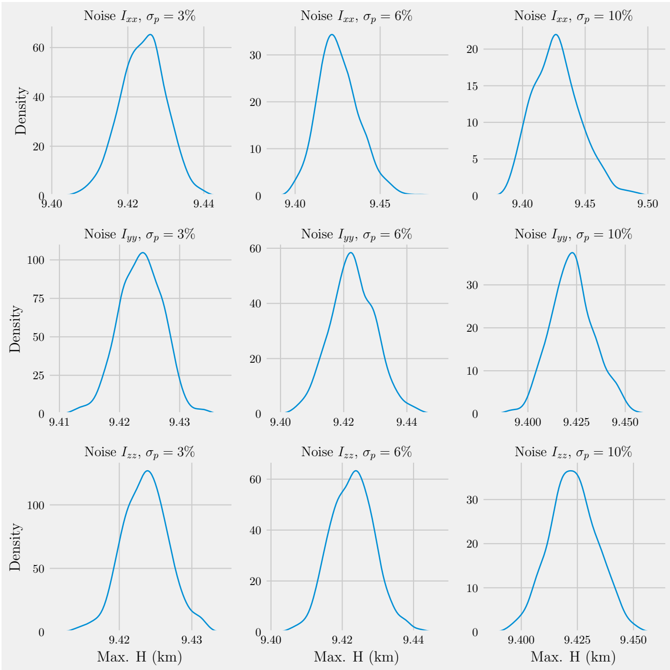

FIGURE 4.30: Max. altitude density estimates from noise unc. and $v_w = +1$ m/s case.

The angle of attack profiles for all trajectories show a stability tendency similar to the nominal simulation. The approximate maximum angle of attack of about +4.7 deg right after launch as presented in Fig. 4.31. The angle of attack trajectories are shown to be close to zero for the rest of the flight. For all of the uncertainties, a slight oscillation is noticeable after reaching apogee.

It is evident from Fig. 4.32 that for the sideslip trajectories the change in the oscillation phase and amplitude grows in magnitude as σ_p increases. Particularly for I_{yy} and I_{zz} uncertainties with $\sigma_p = 10\%$, some trajectory outliers can be identified as their trajectories drift to the negative region around apogee. Across moments of inertia, the trajectories with I_{yy} and I_{zz} uncertainties share similar profiles. For all

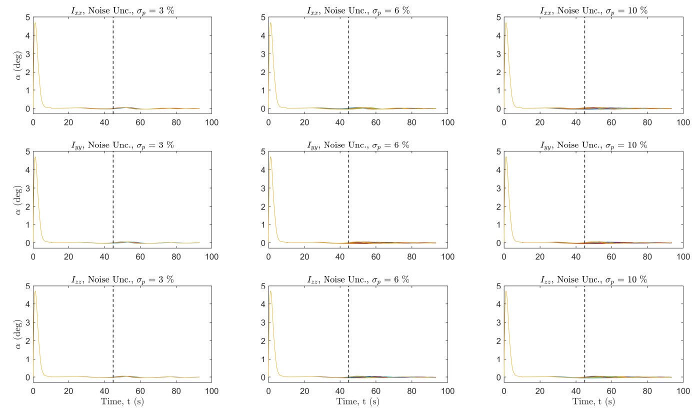

FIGURE 4.31: Angle of attack comparison from noise unc. and v_w = +1 m/s case, dashed line represents the approximated apogee timings.

trajectories, no clear sign of asymptotic stability is shown. However, the sideslip angle is kept between -1 deg $< \beta <$ 1 deg throughout the whole flight.

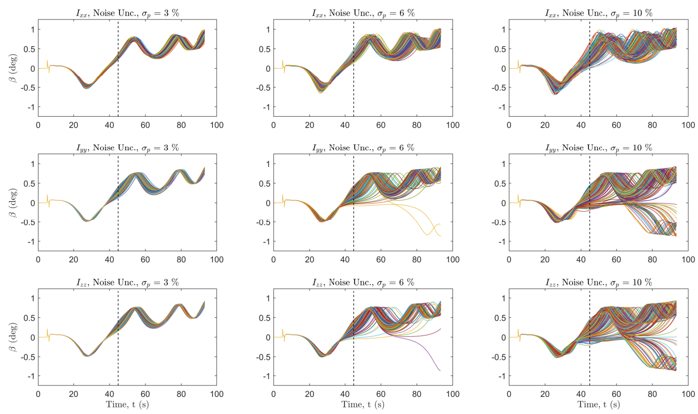

FIGURE 4.32: Sideslip angle comparison from noise unc. and v_w = +1 m/s case, dashed line represents approximated apogee timings.

4.3.7 Case 5: Noise Unc. and $v_w = +2$ m/s

The impact point distributions are shown in Fig. 4.33. It can be seen that the impact points for I_{yy} and I_{zz} uncertainties show similar clusters with the same σ_p values. Multiple high-density spots can also be observed from some of the

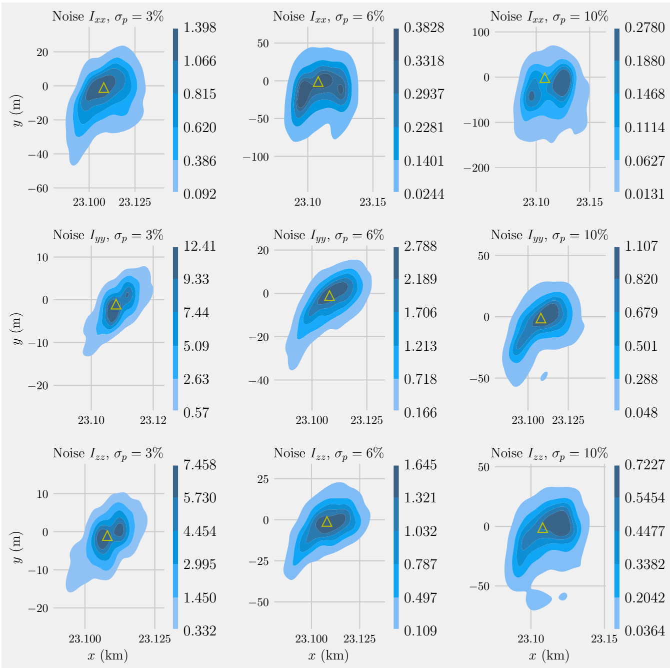

FIGURE 4.33: Final xy position results for noise unc. with v_w = +2 m/s, yellow triangle indicates the nominal final xy.

distributions. These characteristics can be further seen by the multi-modalities in the univariate final x density estimation shown in Fig. 4.34. However, the univariate final y density estimations (Fig. 4.35) show a close resemblance to a normal distribution.

Tab. 4.8 indicates that the mean and standard deviations of all indicators for I_{yy} and I_{zz} uncertainties with respect to each σ_p display similar values. Compared to the nominal value, the final x averages across all uncertainties differ only by a small amount with the largest deviation of (+)5 meters occurring on 10% I_{xx} uncertainty. The same thing can also be said for the maximum altitude with the largest deviation of (+)1 meter over multiple uncertainties. As illustrated in Fig. 4.36, the distributions of the maximum altitude show a close resemblance to a normal distribution.

On contrary, the increase in σ_p leads to the decrease of the averages of the final y value. This decrease is more evident with the I_{xx} uncertainties. The standard deviation for all of the indicators increases as σ_p increases. Relative to the I_{yy} and I_{zz} uncertainties, the uncertainties in I_{xx} create the largest standard deviations in

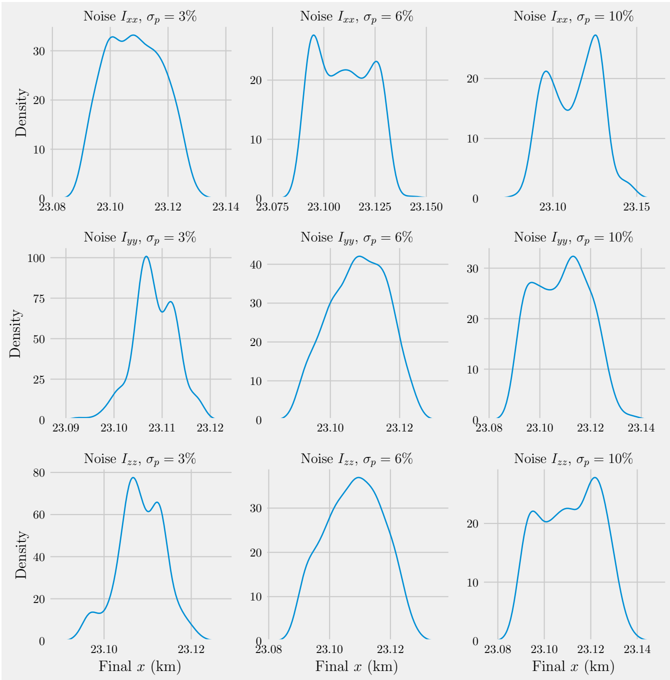

FIGURE 4.34: Final x density estimates from noise unc. and $v_w = +2$ m/s case.

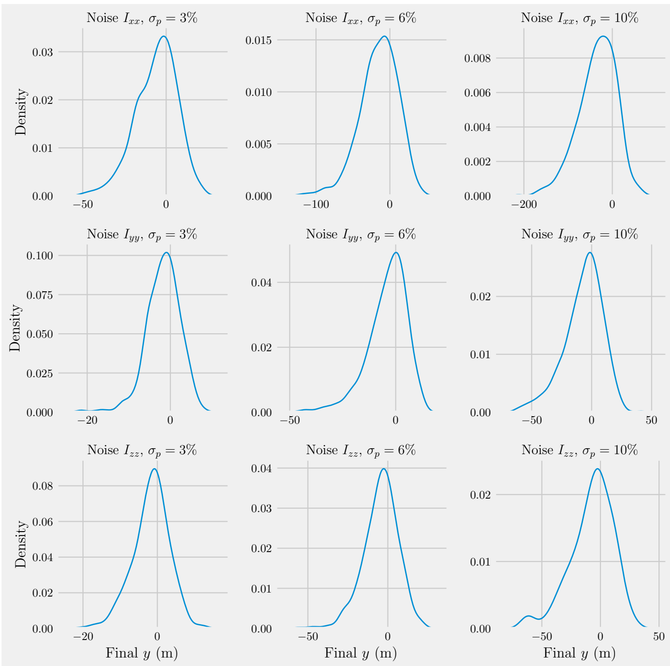

FIGURE 4.35: Final y density estimates from noise unc. and $v_w = +2$ m/s case.

Indicator	Mean and std. dev.	Nominal Sim.	Noise Uncertainty								
			I_{xx}, σ_p (%)			I_{yy}, σ_p (%)			I_{zz}, σ_p (%)		
			3	6	10	3	6	10	3	6	10
Final x	μ (km)	23.108	23.108	23.110	23.113	23.108	23.108	23.108	23.108	23.108	23.111
	σ (m)	0	10	13	15	4	8	11	5	9	13
Final y	μ (m)	-1	-6	-15	-34	-2	-4	-7	-2	-4	-7
	σ (m)	0	12	26	43	4	9	16	5	11	19
Max. R	μ (km)	23.108	23.108	23.110	23.113	23.108	23.108	23.108	23.108	23.108	23.111
	σ (m)	0	10	13	15	4	8	11	5	9	13
Max. H	μ (km)	9.450	9.449	9.449	9.449	9.449	9.449	9.449	9.449	9.449	9.450
	σ (m)	0	3	6	11	1	2	4	1	2	4

TABLE 4.8: Average and standard deviation summary from noise unc. and $v_w = +2$ m/s case.

all of the indicators. The stark difference of the I_{xx} uncertainties can be seen from its final y standard deviations; about triple the values with the same σ_p uncertainty when compared to I_{yy} and I_{zz} uncertainties.

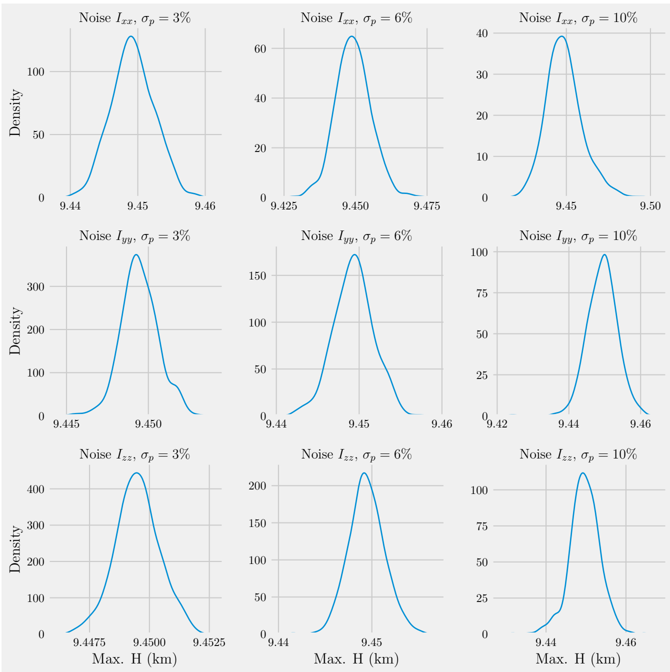

FIGURE 4.36: Max. altitude density estimates from noise unc. and $v_w = +2$ m/s case.

All angle of attack trajectories show a stability tendency similar to the nominal simulation. The approximate maximum angle of attack of about +4.7 deg right after launch as presented in Fig. 4.37. The angle of attack trajectories are shown to be close to zero for the rest of the flight. For all of the uncertainties, a slight oscillation is noticeable after reaching apogee.

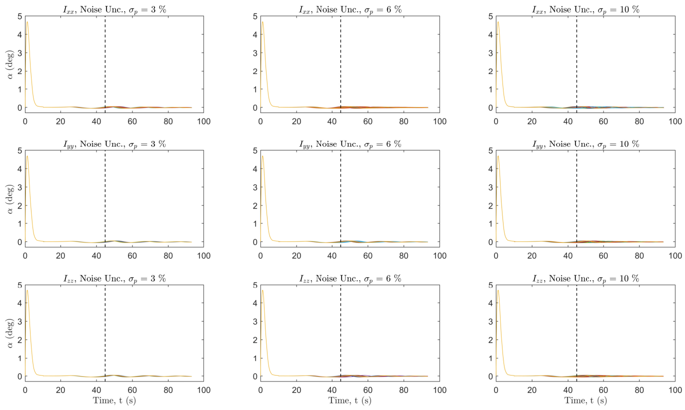

FIGURE 4.37: Angle of attack comparison from noise unc. and v_w = +2 m/s case, dashed line represents the approximated apogee timings.

It is evident from Fig. 4.38 that for the sideslip trajectories the change in the oscillation phase and amplitude grows in magnitude as σ_p increases. Particularly with $\sigma_p = 10\%$, some trajectory outliers can be identified as their trajectories drift to the positive region around apogee except for the I_{xx} uncertainty. However, no trajectories for the I_{xx} uncertainties drift to the negative region. Across moments of inertia, the trajectories with I_{yy} and I_{zz} uncertainties share similar profiles. For all trajectories, no clear sign of asymptotic stability is shown. However, the sideslip angle is kept between ± 1 deg throughout the whole flight.

4.3.8 Case 6: Noise Unc. and $v_w = +3$ m/s

For all distributions, the nominal impact point is shown to be located in the highest probability density areas as shown in Fig. 4.39. Impact points for I_{yy} and I_{zz} uncertainties show a similar cluster with the same σ_p values. Their univariate probability density estimates further supported the previous statement as shown in Fig. 4.40 and Fig. 4.41. As illustrated in Fig. 4.42, the distributions of the maximum altitude show a close resemblance to a normal distribution.

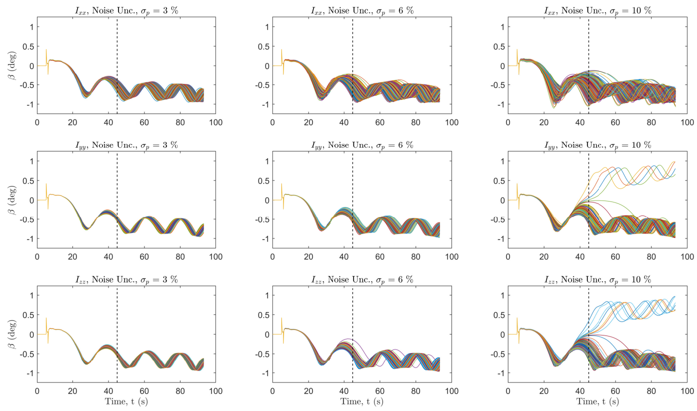

FIGURE 4.38: Sideslip angle comparison from noise unc. and $v_w = +2$ m/s case, dashed line represents approximated apogee timings.

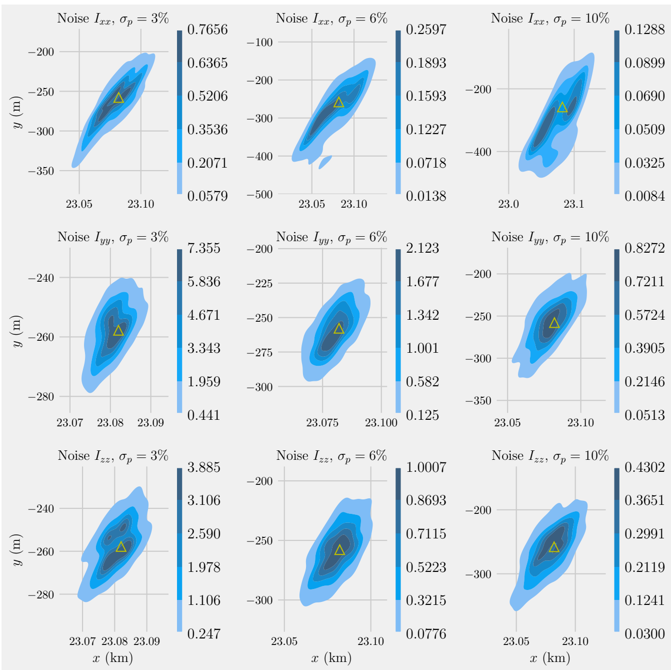

FIGURE 4.39: Final xy position results for noise unc. with $v_w = +3$ m/s, yellow triangle indicates the nominal final xy.

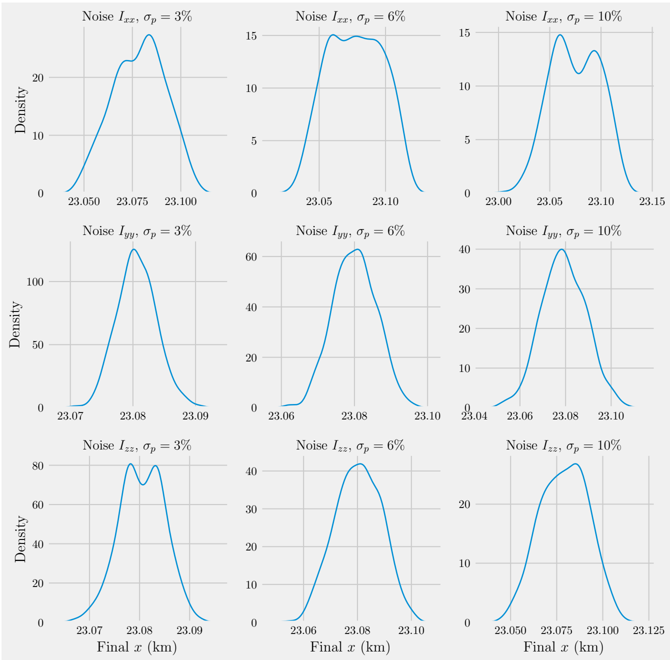

FIGURE 4.40: Final x density estimates from noise unc. and $v_w = +3$ m/s case.

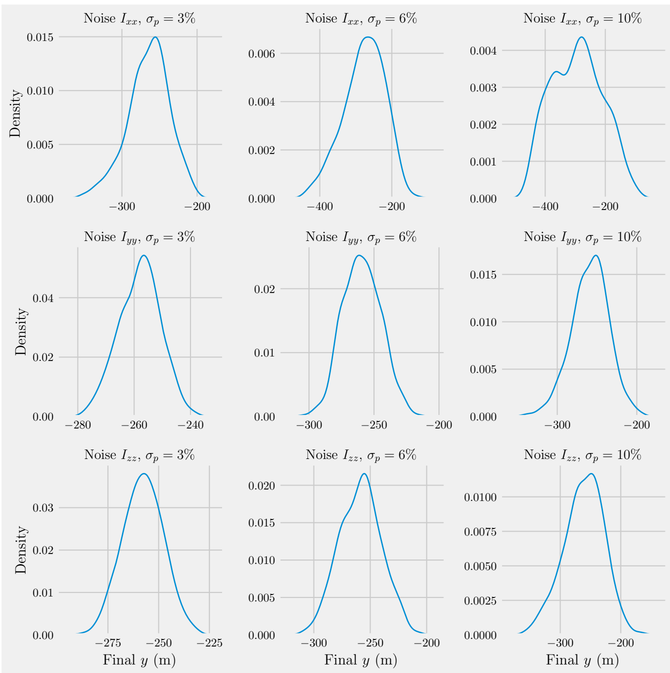

FIGURE 4.41: Final y density estimates from noise unc. and $v_w = +3$ m/s case.

From Tab. 4.9 it is also evident that across the same σ_p the mean and standard deviations of all indicators for I_{yy} and I_{zz} uncertainties have similar values. All indicators' averages from I_{yy} and I_{zz} uncertainties differ only by a small amount. In contrast, the I_{xx} uncertainties create the largest average difference on all of the indicators.

Indicator	Mean and std. dev.	Nominal Sim.	Noise Uncertainty								
			I_{xx}, σ_p (%)			I_{yy}, σ_p (%)			I_{zz}, σ_p (%)		
			3	6	10	3	6	10	3	6	10
Final x	μ (km)	23.082	23.079	23.077	23.075	23.081	23.080	23.079	23.080	23.080	23.079
	σ (m)	0	13	20	24	3	6	10	5	8	13
Final y	μ (m)	-258	-265	-277	-294	-258	-259	-259	-258	-259	-261
	σ (m)	0	28	57	84	7	15	24	10	18	33
Max. R	μ (km)	23.083	23.080	23.079	23.077	23.082	23.081	23.081	23.082	23.082	23.081
	σ (m)	0	13	20	23	3	6	10	4	8	13
Max. H	μ (km)	9.466	9.467	9.470	9.477	9.466	9.466	9.466	9.466	9.466	9.466
	σ (m)	0	5	13	25	2	3	5	2	4	6

TABLE 4.9: Average and standard deviation summary from noise unc. and $v_w = +3$ m/s case.

The increase in σ_p leads to the decrease of the averages of the final y value. This decrease is more evident with the I_{xx} uncertainties. The standard deviation for all of the indicators increases as σ_p increases. Relative to the I_{yy} and I_{zz} uncertainties, the uncertainties in I_{xx} create the largest standard deviations in all of the indicators; about 3 times as much on the final x, 4 times on the final y, and 3 times on the maximum altitude.

All angle of attack trajectories follow a stability profile tendency similar to the nominal simulation while having the approximate maximum angle of attack of about +4.7 deg right after launch as presented in Fig. 4.43. Thereafter, the angle of attack is maintained close to zero. For all of the uncertainties, there is a slight noticeable oscillation after reaching apogee.

As can be seen in Fig. 4.44 that for the sideslip angle trajectories the change in the oscillation phase and amplitude grows in magnitude as σ_p increases. Across moments of inertia, the trajectories with I_{yy} and I_{zz} uncertainties show a similar profile while the variations in the oscillation phase and amplitude are even more distinct with the uncertainty in I_{xx}. For all trajectories, no clear sign of asymptotic stability is shown. However, the sideslip angle is kept between -1 deg $< \beta <$ 1 deg throughout the whole flight.

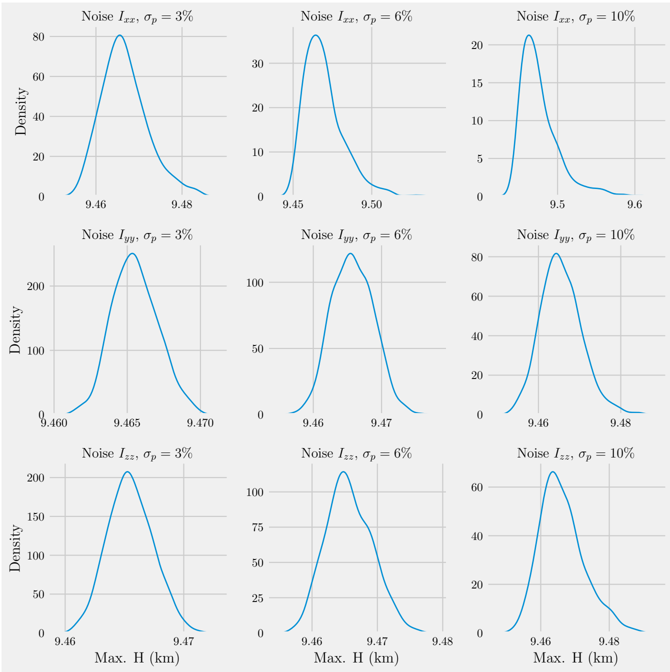

FIGURE 4.42: Max. altitude density estimates from noise unc. and $v_w = +3$ m/s case.

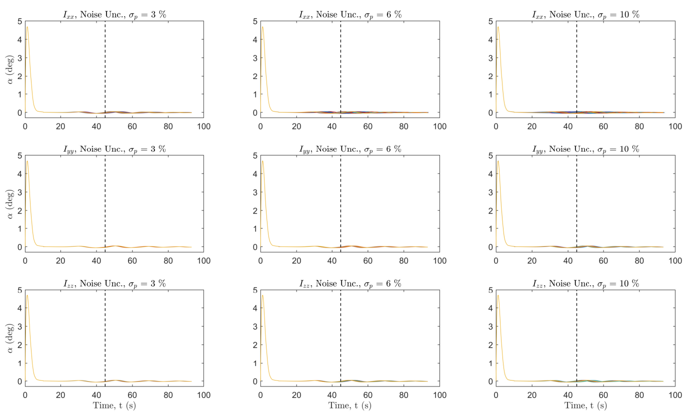

FIGURE 4.43: Angle of attack comparison from noise unc. and v_w = +3 m/s case, dashed line represents the approximated apogee timings.

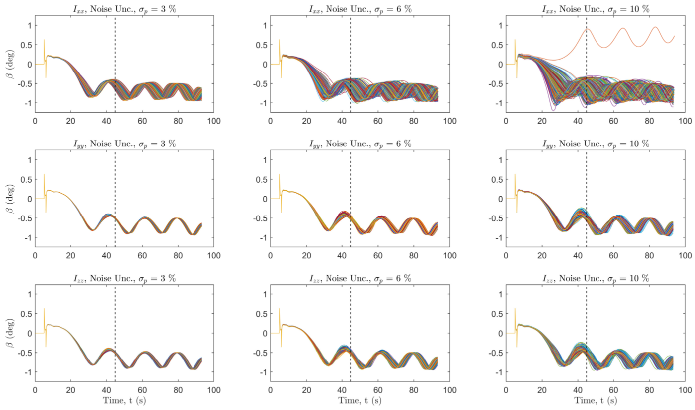

FIGURE 4.44: Sideslip angle comparison from noise unc. and v_w = +3 m/s case, dashed line represents approximated apogee timings.

4.3.9 Case 7: 10,000 Runs, Constant Unc. and $v_w = +2$ m/s

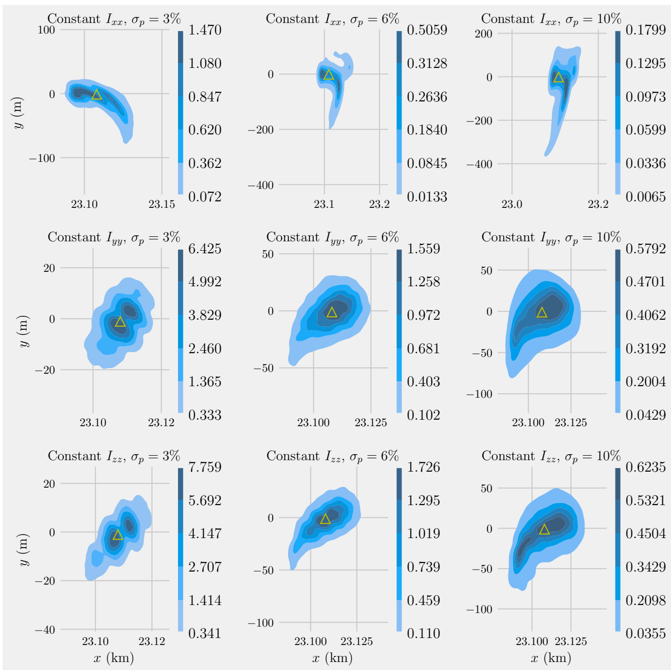

FIGURE 4.45: Final xy position results for constant unc. with v_w = +2 m/s and 10,000 runs, yellow triangle indicates the nominal final xy.

From Fig. 4.45 it is evident that similar clusters of impact points can be seen from I_{yy} and I_{zz}. The nominal impact point is shown to be inside the highest probability density areas except for the I_{xx} uncertainties. The multi-modalities in the final x density for I_{xx} shown in Fig. 4.46 can be seen more profound when compared to the same case with 500 runs (Fig. 4.16). However, there is still no multi-modality observed for the final y density as shown in Fig. 4.47.

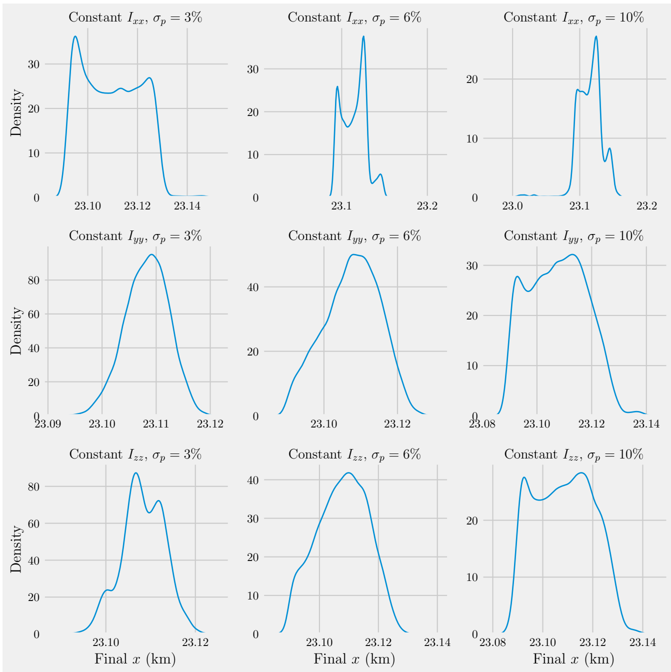

FIGURE 4.46: Final x density estimates from constant unc. and v_w = +2 m/s case with 10,000 runs.

Tab. 4.10 displays similar values when compared to the results of the 500 runs (Tab. 4.5). The mean and standard deviations of all indicators for I_{yy} and I_{zz} uncertainties with respect to each σ_p display similar values. Compared to the nominal value, the final x averages across all uncertainties differ only by a small amount with the largest deviation of (+)7 meters occurring on 6% and 10% I_{xx} uncertainties. The same thing can also be said for the maximum altitude with the largest deviation of (-)2 meters occurring on 6% and 10% I_{xx} uncertainties. As illustrated in Fig. 4.48, the distributions of the maximum altitude show a resemblance to a normal distribution.

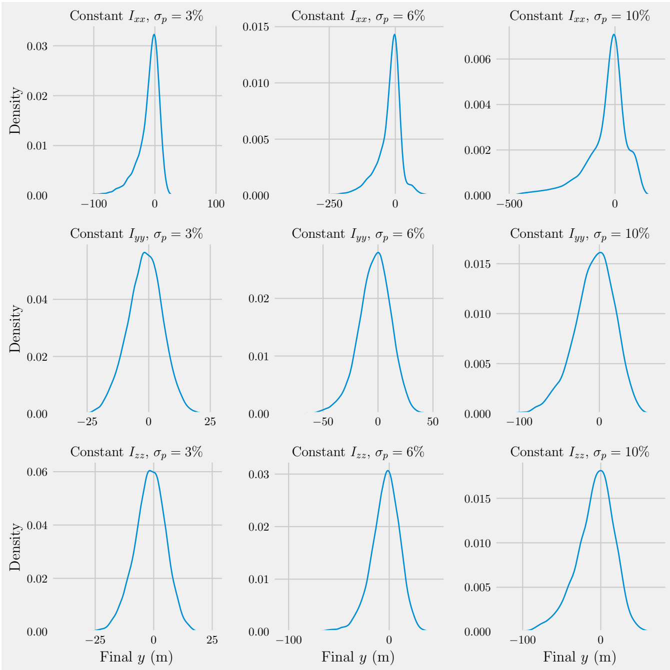

FIGURE 4.47: Final y density estimates from constant unc. and v_w = +2 m/s case with 10,000 runs.

Indicator	Mean and std. dev.	Nominal Sim.	Constant Uncertainty								
			I_{xx}, σ_p (%)			I_{yy}, σ_p (%)			I_{zz}, σ_p (%)		
			3	6	10	3	6	10	3	6	10
Final x	μ (km)	23.108	23.109	23.115	23.115	23.108	23.108	23.108	23.108	23.108	23.108
	σ (m)	0	11	14	20	4	8	10	5	9	11
Final y	μ (m)	-1	-10	-23	-38	-2	-3	-6	-2	-4	-7
	σ (m)	0	19	49	98	7	15	25	7	14	24
Max. R	μ (km)	23.108	23.110	23.115	23.115	23.108	23.108	23.108	23.108	23.108	23.108
	σ (m)	0	11	14	20	4	8	10	5	9	11
Max. H	μ (km)	9.450	9.449	9.448	9.448	9.450	9.450	9.450	9.450	9.450	9.450
	σ (m)	0	1	4	18	2	3	6	1	2	4

TABLE 4.10: Average and standard deviation summary from constant unc. and v_w = +2 m/s case with 10,000 runs.

The increase in σ_p leads to the decrease of the averages of the final y value. This decrease is more evident with the I_{xx} uncertainties. The standard deviation for all of the indicators increases as σ_p increases. Relative to the I_{yy} and I_{zz} uncertainties, the standard deviations of I_{xx} uncertainties have about double the values with the same σ_p uncertainty for all indicators except for the final y values where it is about triple the values.

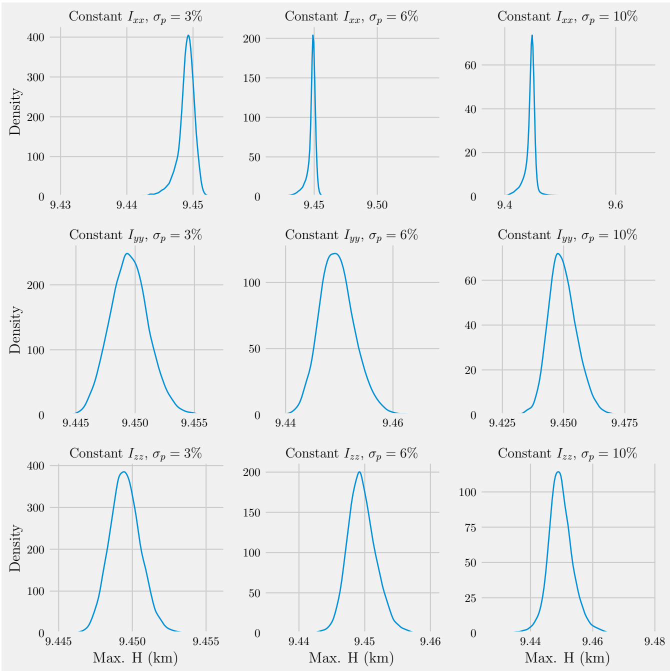

FIGURE 4.48: Max. altitude density estimates from constant unc. and $v_w = +2$ m/s case with 10,000 runs.

All angle of attack trajectories show a stability tendency similar to the nominal simulation. The approximate maximum angle of attack of about +4.7 deg right after launch as presented in Fig. 4.49. The angle of attack trajectories are shown to be close to zero for the rest of the flight. For all of the uncertainties, a slight oscillation is noticeable after reaching apogee.

It can be seen from Fig. 4.50 that for the sideslip trajectories the change in the oscillation phase and amplitude grows in magnitude as σ_p increases. Particularly with $\sigma_p = 10\%$, some trajectory outliers can be identified as their trajectories drift to the positive region around apogee. The outliers are more profound with the I_{xx} uncertainty. The number of outliers has increased due to the increased

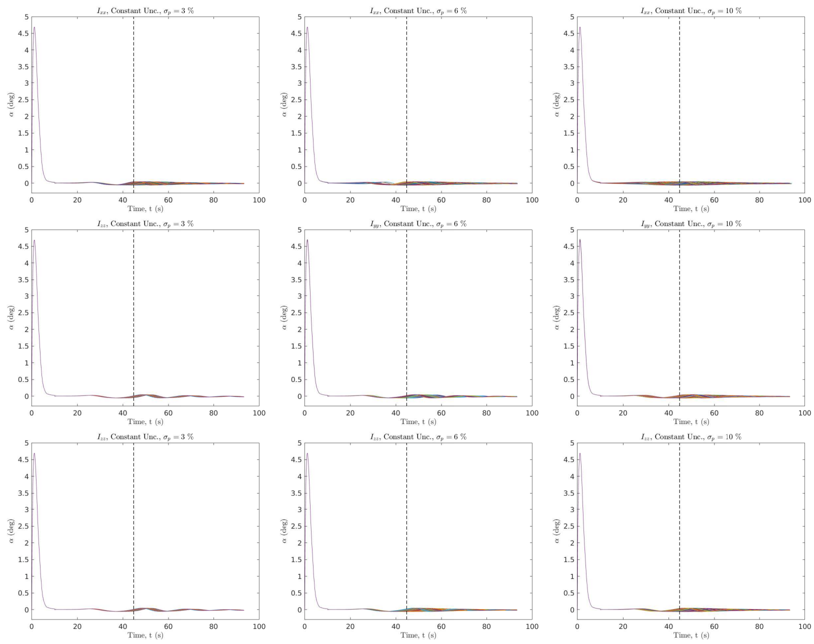

FIGURE 4.49: Angle of attack comparison from constant unc. and $v_w = +2$ m/s case with 10,000 runs, dashed line represents the approximated apogee timings.

number of simulations but the trajectories are still similar to the 500 runs (Fig. 4.20). However, there are now some trajectories that start to drift to the positive direction right after burnout. Across moments of inertia, the trajectories with I_{yy} and I_{zz} uncertainties share similar profiles. For all trajectories, no clear sign of asymptotic stability is shown. However, the sideslip angle is kept between -1 deg $< \beta <$ 1 deg throughout the whole flight.

4.3.10 Case 8: 10,000 Runs, Noise Unc. and $v_w = +2$ m/s

From Fig. 4.51 similar clusters of impact points can be seen from I_{yy} and I_{zz}. The nominal impact point is shown to be inside the highest probability density areas except for the 6% and 10% I_{xx} uncertainties. From Fig. 4.52, multi-modalities can be seen more profound in the final x density when compared to the same case with 500 runs (Fig. 4.34). However, there is still no multi-modality observed for the final y density as shown in Fig. 4.53.

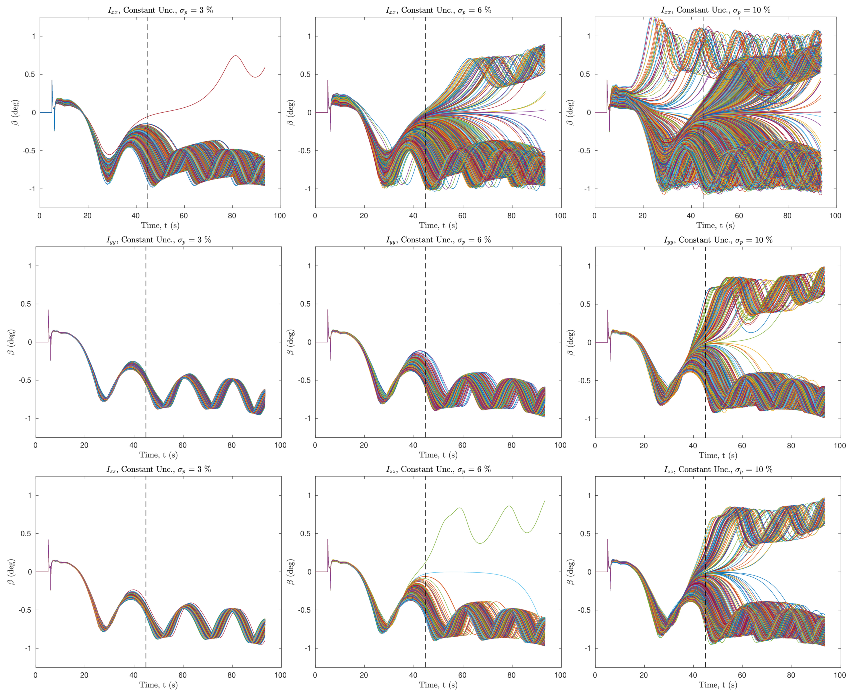

FIGURE 4.50: Sideslip angle comparison from constant unc. and $v_w = +2$ m/s case with 10,000 runs, dashed line represents approximated apogee timings.

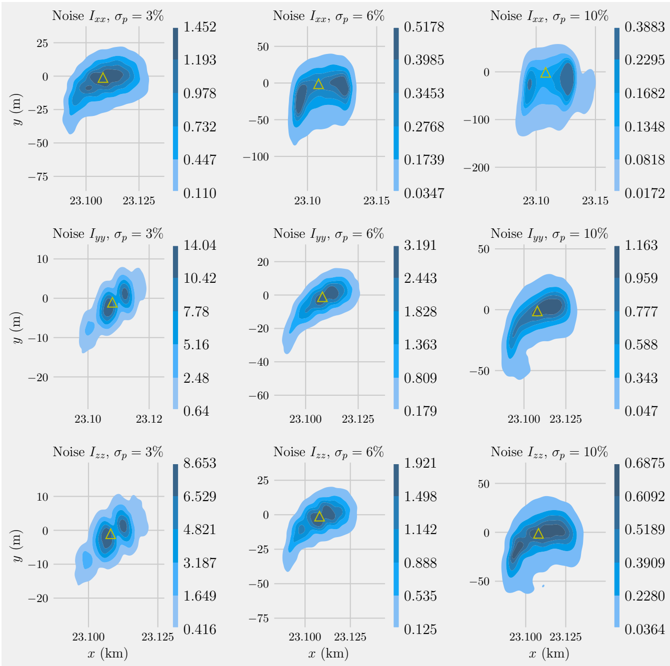

FIGURE 4.51: Final xy position results for noise unc. with $v_w = +2$ m/s and 10,000 runs, yellow triangle indicates the nominal final xy.

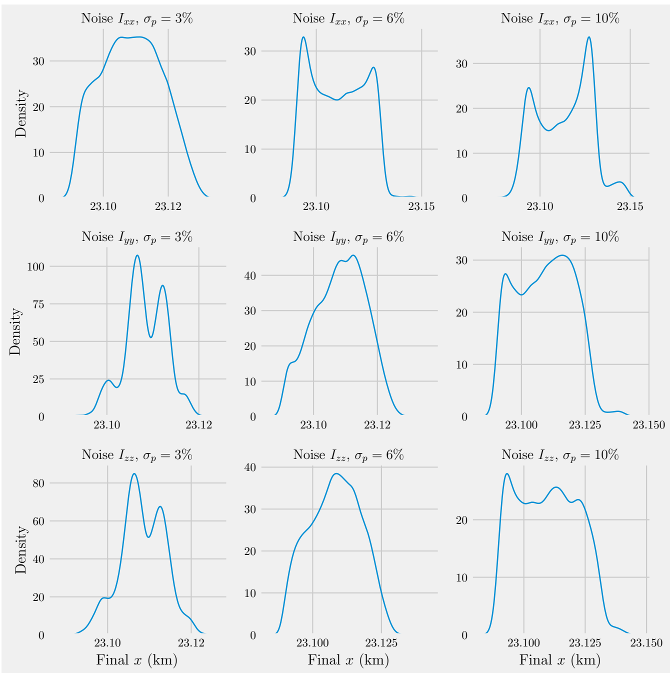

FIGURE 4.52: Final x density estimates from noise unc. and $v_w = +2$ m/s case with 10,000 runs.

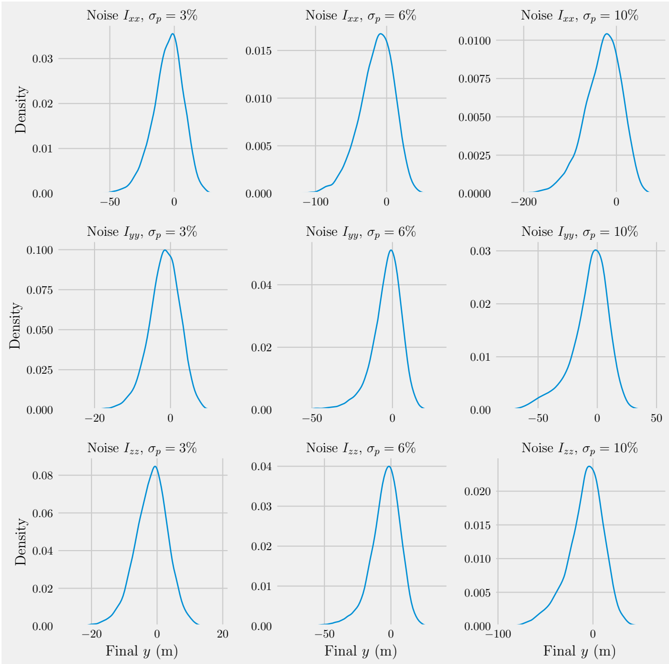

FIGURE 4.53: Final y density estimates from noise unc. and v_w = +2 m/s case with 10,000 runs.

Tab. 4.11 displays similar values when compared to the results of the 500 runs (Tab. 4.8). The mean and standard deviations of all indicators for I_{yy} and I_{zz} uncertainties with respect to each σ_p display similar values. Compared to the nominal value, the final x averages across all uncertainties differ only by a small amount with the largest deviation of (+)5 meters occurring on 10% and 10% I_{xx} uncertainties. The same thing can also be said for the maximum altitude with the largest deviation of (-)1 for all uncertainties. As illustrated in Fig. 4.54, the distributions of the maximum altitude show a resemblance to a normal distribution.

The increase in σ_p leads to the decrease of the averages of the final y value. This decrease is more evident with the I_{xx} uncertainties. The standard deviation for all of the indicators increases as σ_p increases. Relative to the I_{yy} and I_{zz} uncertainties, the standard deviations of I_{xx} uncertainties have about 1.5 times the values with the same σ_p uncertainty for all indicators except for the final y values where it is about double the values.

All angle of attack trajectories show a stability tendency similar to the nominal simulation. The approximate maximum angle of attack of about +4.7 deg right

Indicator	Mean and std. dev.	Nominal Sim.	Noise Uncertainty								
			I_{xx}, σ_p (%)			I_{yy}, σ_p (%)			I_{zz}, σ_p (%)		
			3	6	10	3	6	10	3	6	10
Final x	μ (km)	23.108	23.109	23.110	23.113	23.108	23.108	23.109	23.108	23.108	23.110
	σ (m)	0	9	13	15	4	8	11	5	9	12
Final y	μ (m)	-1	-5	-14	-30	-2	-4	-6	-2	-4	-8
	σ (m)	0	12	25	40	4	10	16	5	11	19
Max. R	μ (km)	23.108	23.109	23.110	23.113	23.108	23.108	23.109	23.108	23.108	23.110
	σ (m)	0	9	13	15	4	8	11	5	9	12
Max. H	μ (km)	9.450	9.449	9.449	9.449	9.449	9.449	9.449	9.449	9.449	9.449
	σ (m)	0	3	6	11	1	2	5	1	2	4

TABLE 4.11: Average and standard deviation summary from noise unc. and $v_w = +2$ m/s case with 10,000 runs.

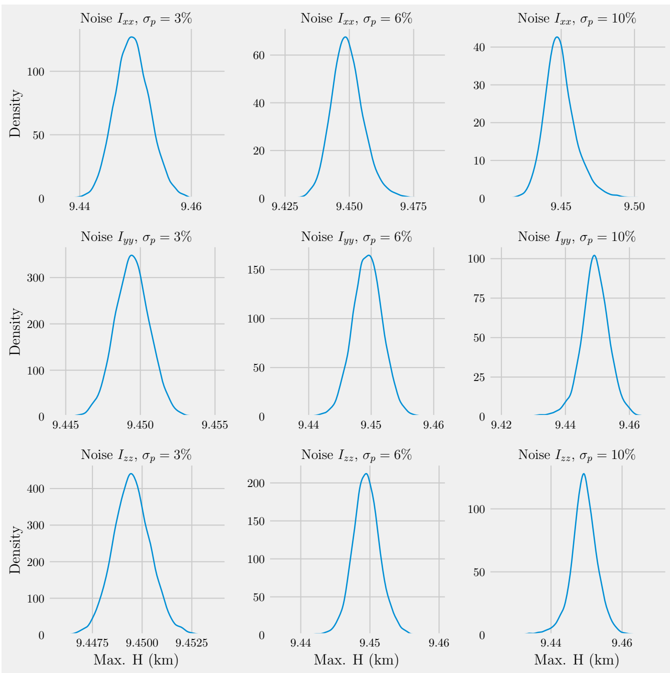

FIGURE 4.54: Max. altitude density estimates from noise unc. and $v_w = +2$ m/s case with 10,000 runs.

after launch as presented in Fig. 4.55. The angle of attack trajectories are shown to be close to zero for the rest of the flight. For all of the uncertainties, a slight oscillation is noticeable after reaching apogee.

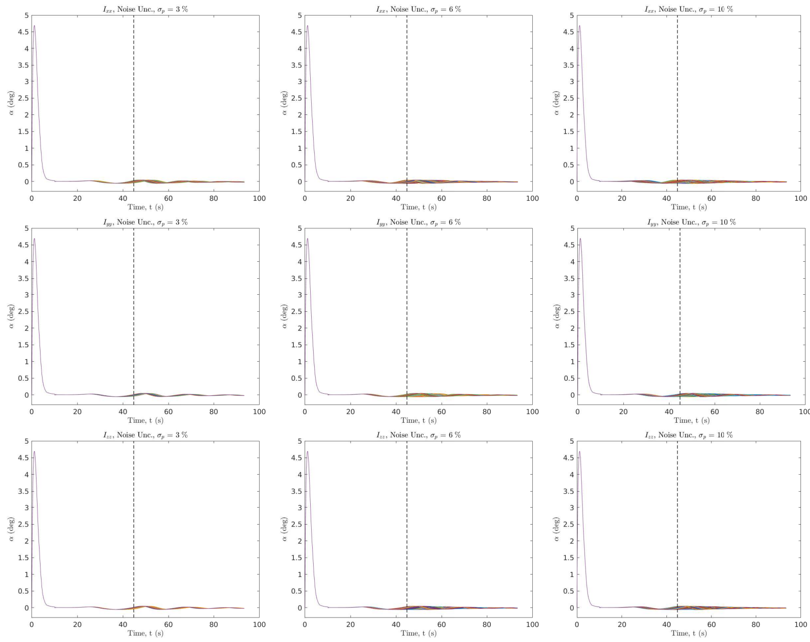

FIGURE 4.55: Angle of attack comparison from noise unc. and $v_w = +2$ m/s case with 10,000 runs, dashed line represents the approximated apogee timings.

It can be seen from Fig. 4.56 that for the sideslip trajectories the change in the oscillation phase and amplitude grows in magnitude as σ_p increases. Particularly with 10% I_{yy} and I_{zz} uncertainties, some trajectory outliers can be identified as their trajectories drift to the positive region around apogee. The number of outliers has increased due to the increased number of simulations but the trajectories still similar to the 500 runs (Fig. 4.38). Across moments of inertia, the trajectories with I_{yy} and I_{zz} uncertainties share similar profiles. For all trajectories, no clear sign of asymptotic stability is shown. However, the sideslip angle is kept between -1 deg $< \beta <$ 1 deg throughout the whole flight.

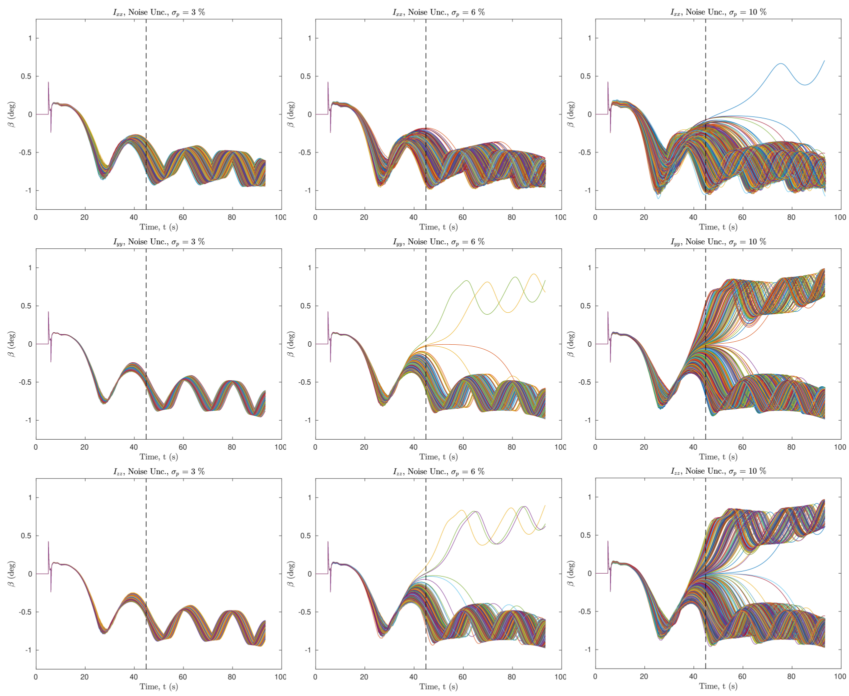

FIGURE 4.56: Sideslip angle comparison from noise unc. and $v_w = +2$ m/s case with 10,000 runs, dashed line represents approximated apogee timings.

CHAPTER 5
SUMMARY, CONCLUSION, RECOMMENDATION

5.1 Summary

In this thesis, LAPAN's RX-200C will be chosen as the model of interest. The primary objective of this thesis is the sensitivity analysis of the rocket's dynamics under moments of inertia uncertainties; specifically in terms of the impact point and the preliminary stability analysis. The Monte Carlo method is performed to reveal patterns due to variations in the moments of inertia.

The rocket's aerodynamic coefficients are generated using Missile DATCOM. he following steps are done in MATLAB and Simulink to support the numerical simulation:

- Mass profile estimation;
- Thrust profile generation
- Atmosphere and gravity modeling;
- Dynamics modeling;
- Moments of inertia uncertainty.

The moments of inertia uncertainty is generated based on the normal distribution in which two types of uncertainty, constant and noise uncertainty, are considered. Considered in the simulations are also four magnitudes of step sidewind velocity disturbance and three standard deviations. For each simulation run, only one of moments inertia will be exposed to uncertainty to isolate their individual influences. Each case will be run 500 times. In addition, the simulation with v_w

= 2 m/s will also be run 10,000 times. The results are visualized using MATLAB and Python through the Seaborn library.

The following indicators are used to analyze the simulation results:

- Nonparametric data analysis using kernel density estimation for univariate and bivariate distribution;
- Normal distribution parametric estimation;
- Visual interpretation of the trajectory of the angle of attack and sideslip angle.

5.2 Conclusion

The conclusion of this thesis will be categorized into several sections:

- Indicators' Averages

  When compared to the nominal values, the average final xy positions and maximum altitude only differ by a small amount for all of the cases except for simulations with $v_w = +3$ m/s where the final y averages differ more than 10 m.

- Indicator's Spread with Uncertainty and $v_w = 0$ m/s

  For a symmetrical rocket without thrust misalignment and sidewind disturbance the rocket will only move in the longitudinal plane. Maximum spread in range and altitude of 1.1 m and 2.5 m with 10% I_{yy} constant uncertainty.

  In this case, no value of I_{xx} or I_{zz} can affect the rocket's dynamics and no value of I_{yy} can induce any lateral-directional motion. Therefore, sidewind disturbance needs to be introduced to produce comparable results between the moments of inertia.

- Indicator's Spread with Uncertainty and Non-Zero Wind Disturbance

  As illustrated in Fig. 5.1, it can be concluded for all indicators that:

  - The uncertainty in the indicators increases as the the moments of inertia's uncertainty σ_p increases.

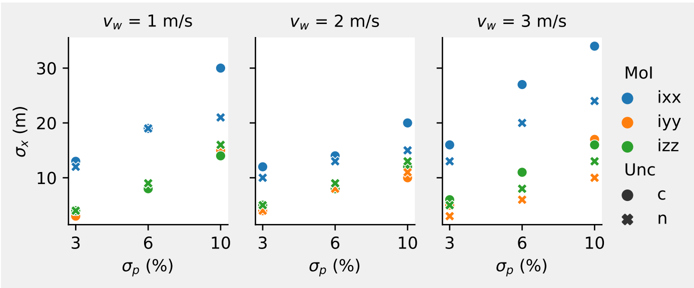

(A) Final x.

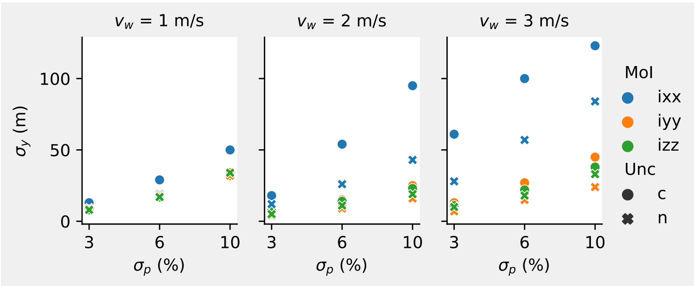

(B) Final x.

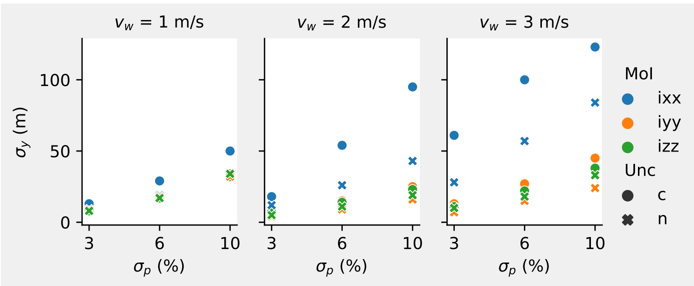

(C) Maximum altitude.

FIGURE 5.1: Indicators' spread comparison over various variables.

- I_{yy} shares I_{zz} the same spread characteristics;
- I_{xx} creates the the largest spread;
- The constant uncertainty creates the larger spread when compared to the noise uncertainty.

Further, the comparison between the indicators' maximum spread shows that for:

- Final x (σ_x):
  - I_{xx}: 34 m (Constant, 10% I_{xx} Unc. with $v_w = 3$ m/s)
  - I_{yy} & I_{zz}: 17 m (Constant, 10% I_{yy} Unc. with $v_w = 3$ m/s)
- Final y (σ_y):
  - I_{xx}: 123 m (Constant, 10% I_{xx} Unc. with $v_w = 3$ m/s)
  - I_{yy} & I_{zz}: 45 m (Constant, 10% I_{yy} Unc. with $v_w = 3$ m/s)
- Max. H (σ_H):
  - I_{xx}: 53 m (Constant, 10% I_{xx} Unc. with $v_w = 3$ m/s)
  - I_{yy} & I_{zz}: 11m (Noise, 10% I_{zz} Unc. with $v_w = 1$ m/s)

- Trajectory Distributions

  The distributions of the final y positions and maximum altitude over all of the cases resemble a normal distribution. However, multi-modalities can be found in the distributions of the final x positions, especially:

  - In simulations where $v_w = +2$ m/s;
  - All I_{xx} uncertainties.

  For all of the cases, I_{yy} and I_{zz} appear to produce similar distribution characteristics.

- 500 vs 10,000 Monte Carlo Simulations

  The 10,000 Monte Carlo runs were performed for the simulations with $v_w = +2$ m/s where multi-modalities occur the most. Although the distributions of the final xy are more distinguishable with 10,000 runs (e.g. Fig. 5.2),

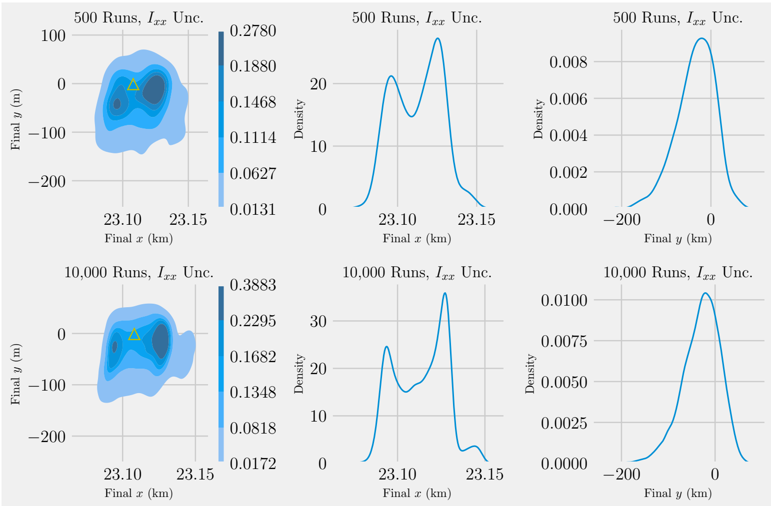

FIGURE 5.2: Impact point distribution from 10% Noise I_{xx} unc. between 500 and 10,000 Monte Carlo Runs

the conclusion that can be drawn is still the same as the 500 runs. The multi-modalities still exist and are found to be more noticeable.

There is also no difference in terms of the maximum altitude and the stability of the rocket. In other words, 500 Monte Carlo runs are good enough for the simulations with $v_w = +2$ m/s. However, this still might not be the case for $v_w = +1$ m/s and 3 m/s.

- Angle of Attack

  None of the uncertainties causes any significant change in the stability and trajectory of the angle of attack over all of the simulation cases. The maximum angle of attack of about 4.7 deg occurs right after launch. The rocket then maintains asymptotic stability close to zero in all of the simulation cases.

- Sideslip Angle

  As a whole, the sideslip angle trajectories follow the nominal trajectory profiles but with a change in the oscillation phase and amplitude.

  Over all of the cases, it can be concluded that:

  – As σ_p increases, the range of the oscillation phase and amplitude increases with:

    * Maximum Phase range: 20 s
    * Maxumum Amplitude range: 0.5 deg
  - There is no sign of asymptotic stability. However, the sideslip angle is contained between ±1 deg over the whole flight;
  - I_{yy} and I_{zz} appear to give the same effects to the sideslip angle trajectories.

There are also some trajectory outliers that may drift/flip into the opposite direction, when:

  - The number of outliers increases with σ_p;
  - With an increase in v_w:
    * I_{xx}: The number of outliers increases;
    * I_{yy} and I_{zz}: The number of outliers decreases.
  - Across uncertainty types:
    * I_{xx}: outliers occur often with constant uncertainty but hardly with noise uncertainty;
    * I_{yy} and I_{zz}: no difference between uncertainty types.

5.3 Recommendation

Based on the outcome of this thesis, several recommendations can be made:

- The effects of uncertainties on the rocket's structural integrity.
- Design a practical adaptive control system design that can compensate for the moments of inertia uncertainty or any uncertainty in general.
- A more realistic wind model and uncertainty model can be utilized to better simulate a real-world situation.
- Increasing the number of Monte Carlo simulations could give more insight and a better confidence level to the resulting data. However, a Monte Carlo simulation can sometimes be computationally demanding with the resulting

file size growing quickly. Although the required time to process all of the simulations will vary with the available computational power, the output file size will relatively stay the same across different machines. The size of a saved file containing 8 vector states from 10000 simulations with an approximate total flight time of 95 s with 0.02 s fixed time step is approximately 7 GB in size. Therefore, various means such as proper ODE solver, a more efficient code, or the utilization of cloud computing are recommended.

- A more objective indicator of a Monte Carlo simulation on the stability and distribution of the whole nonlinear flight can be beneficial. This can also be achieved by employing machine learning to detect and relate patterns between various parameters.

References

Amberg, B. (2008, February). *A range of different kernels.* Retrieved 2022-01-01, from https://commons.wikimedia.org/w/index.php?curid=5329895

Auman, L., Doyle, J., Rosema, C., Underwood, M., & Blake, W. (2008, August). *Missile Datcom User's Manual - 2008 Revision* (Tech. Rep.). ARMY AVIATION AND MISSILE RESEARCH DEVELOPMENT ENG CTR REDSTONE ARSENAL AL SYSTEM SIMULATION AND DEVELOPMENT DIRECTORATE. Retrieved 2022-01-01, from https://apps.dtic.mil/sti/citations/ADA503576 (Section: Technical Reports)

Blake, W. B. (1998). Missile Datcom: User's Manual - 1997 FORTRAN 90 Revision..

Bloomberg. (2022). *Rocket Startups Craft Bespoke Launchers to Join New Space Race - Bloomberg.* Retrieved 2022-01-01, from https://www.bloomberg.com/news/articles/2021-03-31/rocket-startups-craft-bespoke-launchers-to-join-new-space-race

Company, F. (2022). *The 10 most innovative space companies of 2021.* Retrieved 2022-01-01, from https://www.fastcompany.com/90600324/space-most-innovative-companies-2021

Comparison of orbital launch systems - Wikipedia. (2022). Retrieved 2022-01-01, from https://en.wikipedia.org/wiki/Comparison_of_orbital_launch_systems

Cornelisse, J., Schöyer, H., & Wakker, K. (1979). *Rocket Propulsion and Spaceflight Dynamics.* Pitman. Retrieved from https://books.google.co.id/books?id=HpJTAAAAMAAJ

Drleft. (2010, September). *English: Comparison of a histogram and a kernel density estimate.* Retrieved 2022-01-01, from https://commons.wikimedia.org/w/index.php?curid=57332968

Flight, N. S. (2019, December). *Rocket Lab launches 10th Electron* *flight - critical step towards booster recovery.* Retrieved 2022-01-01, from https://www.nasaspaceflight.com/2019/12/rocket-lab-booster-recovery-10th-electron-flight/

Fuel fraction. (2020, May). Retrieved 2022-01-01, from https://en.wikipedia.org/w/index.php?title=Fuel_fraction&oldid=958876766 (Page Version ID: 958876766)

Ingalls, N. (2006, September). *JSC2006-E-40672 (18 Sept. 2006) — The Soyuz TMA-9 spacecraft launches from the Baikonur Cosmodrome in Kazakhstan Sept. 18, 2006 carrying a new crew to the International Space Station. The Soyuz lifted off at 10:09 a.m. Baikonur time with astronaut Michael E. Lopez-Alegria, Expedition 14 commander and NASA space station science officer; cosmonaut Mikhail Tyurin, Soyuz commander and flight engineer representing Russia's Federal Space Agency; and spaceflight participant Anousheh Ansari, who will spend nine days on the station under a commercial agreement with the Russian Federal Space Agency.* Retrieved 2022-01-01, from https://commons.wikimedia.org/w/index.php?curid=1187328

Jenkins, P. N. (1984, April). *Missile Dynamics Equations for Guidance and Control Modeling and Analysis* (Tech. Rep.). ARMY MISSILE COMMAND REDSTONE ARSENAL AL GUIDANCE AND CONTROL DIRECTORATE. Retrieved 2022-01-01, from https://apps.dtic.mil/sti/citations/ADA151529 (Section: Technical Reports)

Marx, E. (2014, September). *English: Sectional view of the missile Aggregat 2 / V 2.* Retrieved 2022-01-01, from https://commons.wikimedia.org/w/index.php?curid=35249660

MITTR. (2022). *Startup Phantom Space wants to be the Henry Ford of rockets | MIT Technology Review.* Retrieved 2022-01-01, from https://www.technologyreview.com/2021/05/26/1025350/phantom-space-startup-jim-cantrell/

NYTimes. (2022). *Advancements in Space Technology Drive Investor Interest - The New York Times.* Retrieved 2022-01-01, from https://www.nytimes.com/2021/07/07/technology/space-start-ups.html

PSU, E. R. (2022). *2.2.7 - The Empirical Rule | STAT 200.* Retrieved 2022-01-01, from https://online.stat.psu.edu/stat200/lesson/2/2.2/2.2.7

Pusat Teknologi Roket. (2022a). Retrieved 2022-01-01, from http://pustekroket.lapan.go.id/index.php/subblog/pages/2014/16/Fokus-Pengembangan-Roket-Sonda

Pusat Teknologi Roket. (2022b). Retrieved 2022-01-01, from http://pustekroket.lapan.go.id/index.php/home

Seaborn documentation. (2022). Retrieved 2022-01-01, from https://seaborn.pydata.org/

Stevens, B. L., Lewis, F. L., & Johnson, E. N. (2016). *Aircraft Control and Simulation: Dynamics, Controls Design, and Autonomous Systems.* (OCLC: 1159622747)

Tewari, A. (2007). *Atmospheric and Space Flight Dynamics: Modeling and Simulation with MATLAB® and Simulink®.* Birkhäuser Boston. Retrieved from https://books.google.co.id/books?id=0MQSCvCunvoC

U.S. Standard Atmosphere, 1976 (Tech. Rep. No. NOAA-S/T-76-1562). (1976, October). Retrieved 2022-01-01, from https://ntrs.nasa.gov/citations/19770009539 (NTRS Document ID: 19770009539 NTRS Research Center: Legacy CDMS (CDMS))

Vukelich, S. R. (1981, October). *Development Feasibility of Missile Datcom* (Tech. Rep.). MCDONNELL DOUGLAS ASTRONAUTICS CO ST LOUIS MO. Retrieved 2021-09-27, from https://apps.dtic.mil/sti/citations/ADA127378 (Section: Technical Reports)

Wikipedia. (2021, December). *Comparison of orbital launcher families.* Retrieved 2022-01-01, from https://en.wikipedia.org/w/index.php?title=Comparison_of_orbital_launcher_families&oldid=1063025111 (Page Version ID: 1063025111)

Appendices

APPENDIX A
TECHNICAL DRAWING AND MASS PROFILE ESTIMATION METHODS

Technical Drawing

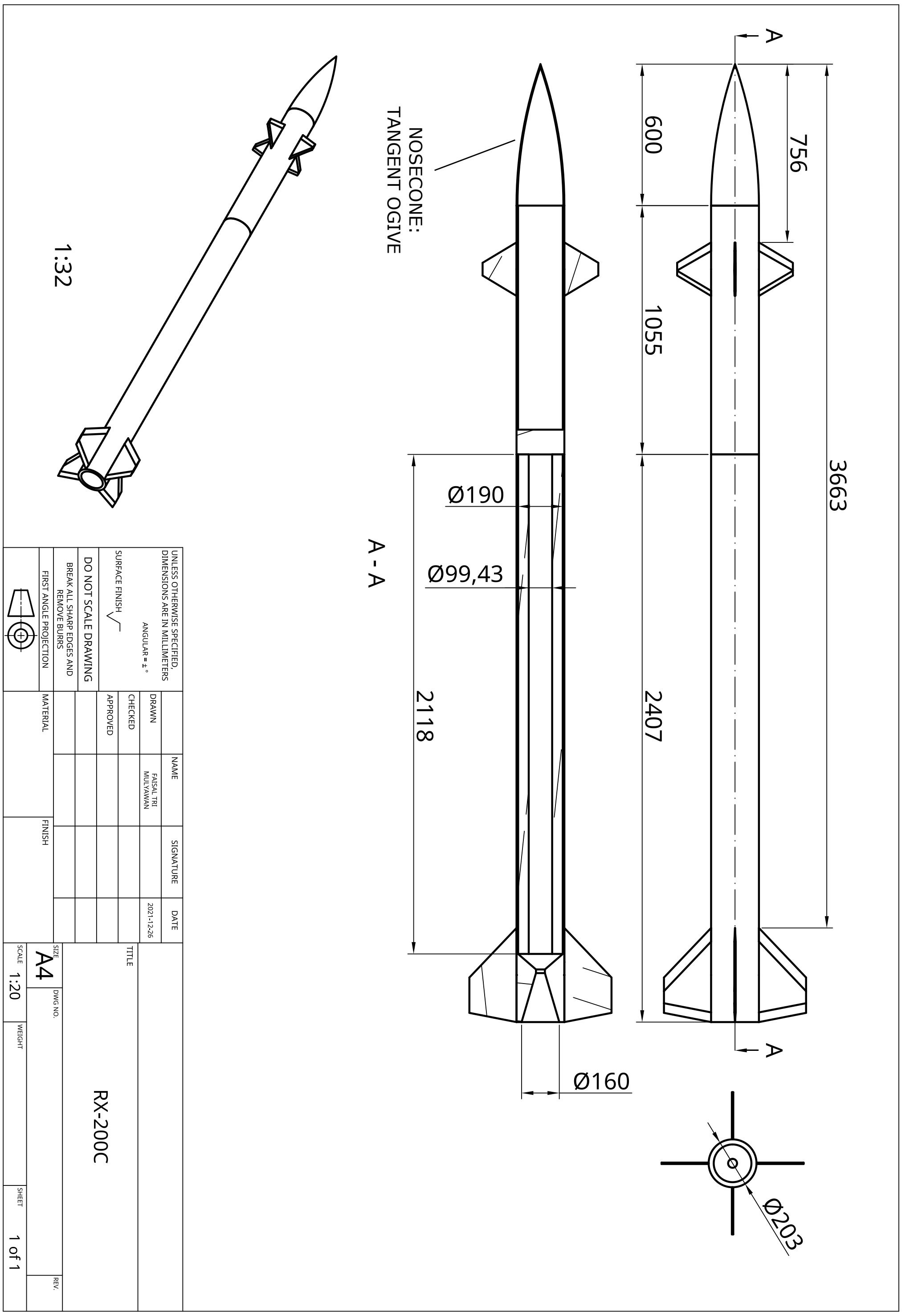
1:32
NOSECONE:
TANGENT OGIVE
A - A
A
600
756
1055
3663
2407
2118
Ø190
Ø99,43
Ø160
Ø203
UNLESS OTHERWISE SPECIFIED:
DIMENSIONS ARE IN MILLIMETERS
SURFACE FINISH
DO NOT SCALE DRAWING
BREAK ALL SHARP EDGES AND
REMOVE BURRS
FIRST ANGLE PROJECTION
DRAWN
CHECKED
APPROVED
MATERIAL
FINISH
NAME
FAISAL TRI
MULYAWAN
SIGNATURE
DATE
TITLE
RX-200C
SIZE
A4
DWG NO.
SCALE
1:20
WEIGHT
SHEET
1 of 1
REV.

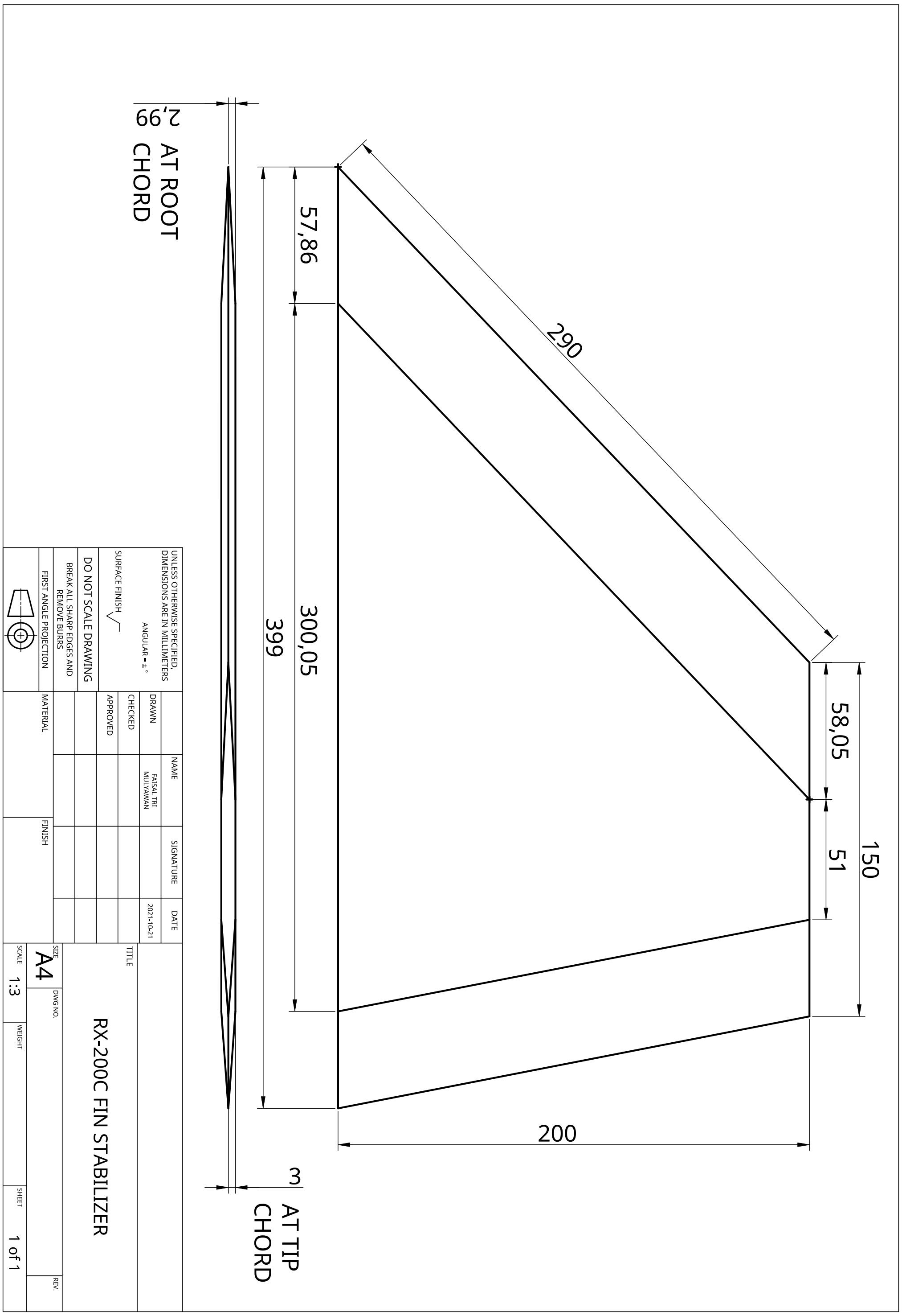
2,99
AT ROOT CHORD
57,86
290
300,05
399
58,05
51
150
200
3
AT TIP CHORD
UNLESS OTHERWISE SPECIFIED, DIMENSIONS ARE IN MILLIMETERS
SURFACE FINISH
DO NOT SCALE DRAWING
BREAK ALL SHARP EDGES AND REMOVE BURRS
FIRST ANGLE PROJECTION
NAME
SIGNATURE
DATE
DRAWN
CHECKED
APPROVED
MATERIAL
FINISH
FAISAL TRI MULYAWAN
2021-10-21
TITLE
RX-200C FIN STABILIZER
SIZE
A4
DWG NO.
REV.
SCALE
1:3
WEIGHT
SHEET
1 of 1

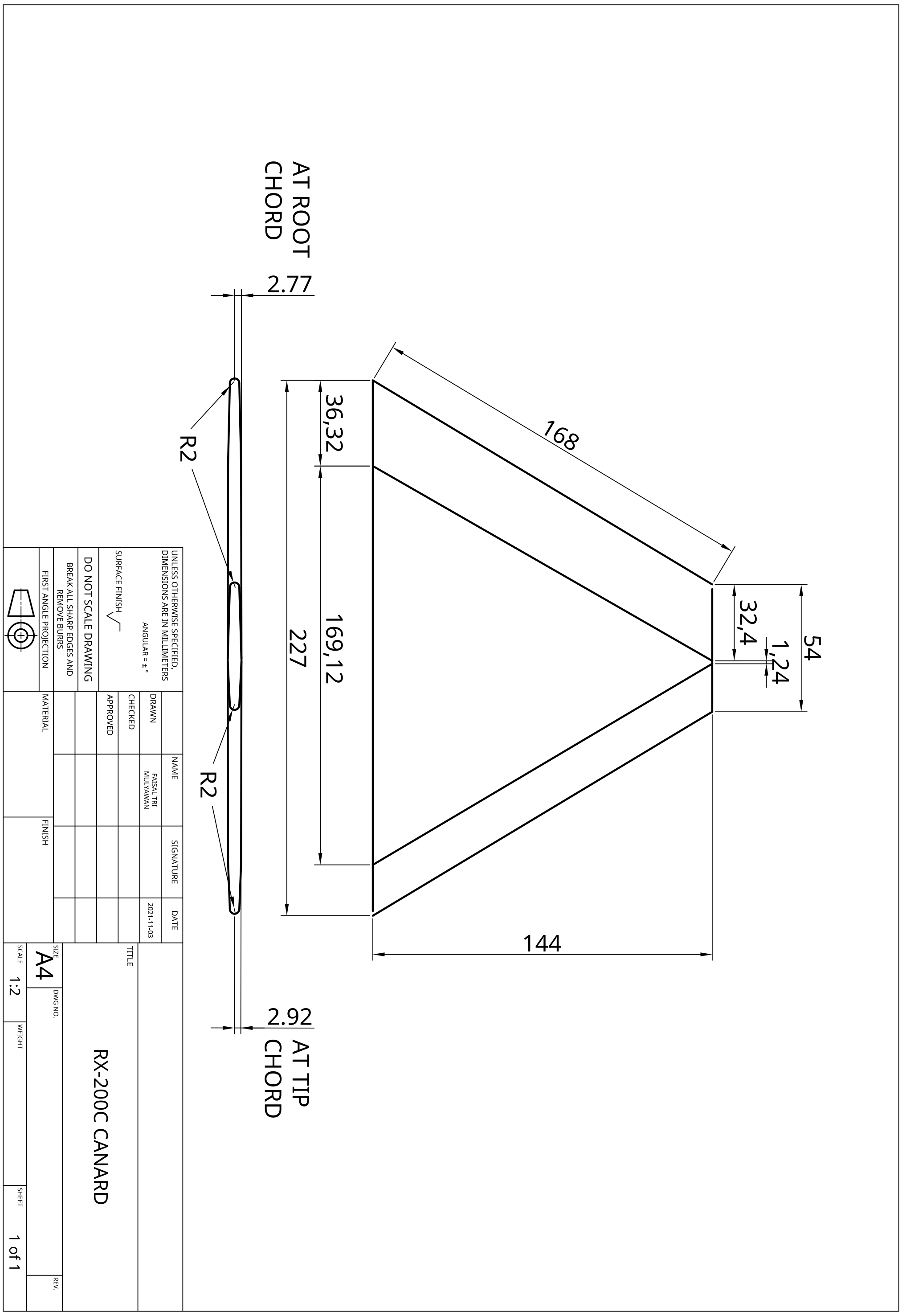
AT ROOT CHORD
2.77
R2
36,32
168
227
169,12
54
32,4
1,24
144
R2
2.92
AT TIP CHORD
UNLESS OTHERWISE SPECIFIED:
DIMENSIONS ARE IN MILLIMETERS
SURFACE FINISH
DO NOT SCALE DRAWING
BREAK ALL SHARP EDGES AND REMOVE BURRS
FIRST ANGLE PROJECTION
DRAWN
CHECKED
APPROVED
MATERIAL
NAME
FAISAL TRI MULYAWAN
SIGNATURE
DATE
FINISH
TITLE
RX-200C CANARD
SIZE
A4
DWG NO.
SCALE
1:2
WEIGHT
SHEET
1 of 1
REV.

Mass Estimation

The mass equation is linearly approximated by:

$$m(t) = \left(\frac{m_e - m_f}{t_{\text{burn}}}\right) t + m_f \tag{A.1}$$

with

$$m_e = m_f - m_{fuel} \tag{A.2}$$

where

- m_f, m_e, and m_{fuel} $\triangleq$ Wet mass, dry mass, and fuel mass of the rocket, respectively;
- t_{burn} $\triangleq$ Motor burn time.

Center of Gravity Estimation

The center of gravity equation is linearly approximated by:

$$x_{cg}(t) = \left(\frac{x_{cg_e} - x_{cg_f}}{t_{\text{burn}}}\right) t + x_{cg_f} \tag{A.3}$$

with

$$x_{cg_e} = \frac{m_f x_{cg_f} + \left(-m_{fuel} x_{cg_{fuel}}\right)}{m_f + (-m_{fuel})} \tag{A.4}$$

where

- x_{cg_e} and x_{cg_f} $\triangleq$ Rocket's center of gravity position at burnout and fully-fueled condition;
- m_{fuel} and $x_{cg_{fuel}}$ $\triangleq$ Initial fuel's mass and center of gravity position.

The center of gravity of the fuel is shown in Fig. A.1 where we have assumed the fuel to be a homogeneous thick-walled hollow cylinder that has its center of gravity at half its length and radius.

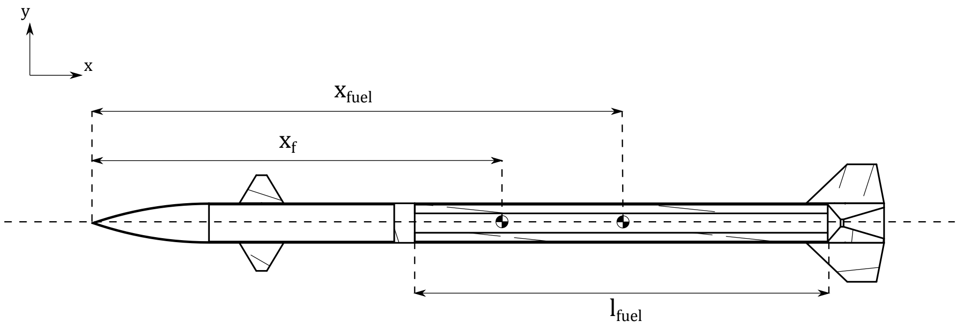

FIGURE A.1: Illustration of the center of gravity positions.

Inertia Estimation

Inertia Definition

The inertia tensor of a rigid body about its center of gravity $G1$ can be defined as:

$$\mathbf{I} = \begin{bmatrix} I_{xx} & -I_{xy} & -I_{xz} \\ -I_{xy} & I_{yy} & -I_{yz} \\ -I_{xz} & -I_{yz} & I_{zz} \end{bmatrix} \tag{A.5}$$

with

$$\begin{aligned} I_{xx} &= \int_m (y^2 + z^2) dm \\ I_{yy} &= \int_m (x^2 + z^2) dm \\ I_{zz} &= \int_m (x^2 + y^2) dm \end{aligned} \tag{A.6}$$

and

$$\begin{aligned} I_{xy} = I_{yx} &= \int_m xydm \\ I_{xz} = I_{zx} &= \int_m xzdm \\ I_{yz} = I_{zy} &= \int_m yzdm \end{aligned} \tag{A.7}$$

where

- I_{xx}, I_{yy}, and $I_{zz} \triangleq$ The mass moment of inertia in x-, y-, and z-axis, respectively;
- I_{xz}, I_{xy}, and $I_{yz} \triangleq$ The products of inertia in xz-, xy-, and yz-plane, respectively.
- $m \triangleq$ The mass of the rigid body;
- x, y, and $z \triangleq$ The position of the rigid body relative to G in x, y, and z-axis.

Due to the integral addition property of the moment inertia from Eq. A.6, the moment of inertia of a fully-fueled rocket can be rewritten as (i.e. for I_{xx_f})

$$\begin{aligned} I_{xx_f} &= \left(\int_m (y^2 + z^2) dm \right)_f \\ &= \left(\int_m (y^2 + z^2) dm \right)_e + \left(\int_m (y^2 + z^2) dm \right)_{fuel} \\ &= I_{xx_e} + I_{xx_{fuel}} \end{aligned} \tag{A.8}$$

where the subscripts f, e, and $fuel$ indicate the inertia of the fully-fueled rocket, burnout rocket, and rocket fuel. Solving for I_{xx_e}

$$I_{xx_e} = I_{xx_f} - I_{xx_{fuel}} \tag{A.9}$$

Following the previous derivations from the inertia definition on Eq. A.5 the inertia I_{xx_e} in Eq. A.9 is taken about the point $G1$ which is the center of gravity of the fully-fueled rocket. The same exact calculations can also be done to the products of inertia which leads us to the generalization

$$[\mathbf{I}_e]_{G1} = \mathbf{I}_f - [\mathbf{I}_{fuel}]_{G1} \tag{A.10}$$

The burnout inertia I_e about its center of gravity can then be redefined using parallel axis theorem as

$$\mathbf{I}_e = [\mathbf{I}_f]_{G2} - [\mathbf{I}_{fuel}]_{G2} \tag{A.11}$$

where we moved the reference point for the inertia tensors to the burnout rocket's center of gravity point $G2$.

Fuel's Inertia

The formula for the fuel's inertia about its center of gravity assuming the fuel to be a homogenous thick-walled hollow cylinder with a radius r, length l, and mass m is given by

$$I_{fuel} = \begin{bmatrix} \frac{1}{2}m(r_2^2 + r_2^2) & 0 & 0 \\ 0 & \frac{1}{12}m(3(r_1^2 + r_2^2) + l^2) & 0 \\ 0 & 0 & \frac{1}{12}m(3(r_1^2 + r_2^2) + l^2) \end{bmatrix} \tag{A.12}$$

Parallel Axis Theorem

Knowing the inertia tensor of a rigid body about its center of gravity, we can recalculate the inertia of the rigid body about any arbitrary point using the parallel axis theorem. It is noted that the second coordinate axes must be parallel relative to the initial axes. Calculating an inertia tensor about a new point $G2$, the parallel axis theorem for the moment of inertia is then given by

$$\begin{aligned} [I_{xx}]_{G2} &= I_{xx} + m((\Delta y)^2 + (\Delta z)^2) \\ [I_{yy}]_{G2} &= I_{yy} + m((\Delta x)^2 + (\Delta z)^2) \\ [I_{zz}]_{G2} &= I_{zz} + m((\Delta x)^2 + (\Delta y)^2) \end{aligned} \tag{A.13}$$

where Δx, Δy, and Δz are the distance between point 1 & 2 on x, y, and z-axis with m the rigid body's mass. Next, the parallel axis theorem for the products of inertia is given by

$$\begin{aligned} [I_{xy}]_{G2} &= [I_{yx}]_{G2} = I_{xy} + m\Delta x\Delta y \\ [I_{xz}]_{G2} &= [I_{zx}]_{G2} = I_{xz} + m\Delta x\Delta z \\ [I_{yz}]_{G2} &= [I_{zy}]_{G2} = I_{yz} + m\Delta y\Delta z \end{aligned} \tag{A.14}$$

Interpolation

The inertia equation is linearly approximated by

$$\mathbf{I}(t) = \left(\frac{\mathbf{I}_e - \mathbf{I}_f}{t_{\text{burn}}} \right) t + \mathbf{I}_f \tag{A.15}$$

APPENDIX B
MATLAB SCRIPTS AND MISSILE DATCOM FILES

DATCOM x_{cg} Iterator Script

Rocket Data Initialization

Monte Carlo Script: Constant Uncertainty

Monte Carlo Script: Noise Uncertainty

Missile DATCOM Input File

Missile DATCOM Output File

Turnitin Report

NUMERICAL INVESTIGATION OF MOMENTS OF INERTIA'S UNCERTAINTY EFFECTS ON LAPAN RX-200C ROCKET

by Faisal Tri Mulyawan

NUMERICAL INVESTIGATION OF MOMENTS OF INERTIA'S UNCERTAINTY EFFECTS ON LAPAN RX-200C ROCKET

ORIGINALITY REPORT

6%	5%	3%	2%
SIMILARITY INDEX	INTERNET SOURCES	PUBLICATIONS	STUDENT PAPERS

PRIMARY SOURCES

1	apps.dtic.mil Internet Source	<1%
2	repository.tudelft.nl Internet Source	<1%
3	"Chapter 9 Planetary Atmosphere", Springer Science and Business Media LLC, 2007 Publication	<1%
4	etd.ohiolink.edu Internet Source	<1%
5	www.intechopen.com Internet Source	<1%
6	H. Le, P. Konečný. "Effect of Some Disturbance Factors on the Motion Stability of Unguided Rockets", Advances in Military Technology, 2020 Publication	<1%
7	uavbook.byu.edu Internet Source	<1%

8	hdl.handle.net Internet Source	<1 %
9	repository.asu.edu Internet Source	<1 %
10	Submitted to Fakultat fur Maschinenwesen der Technischen Universitat Munchen Student Paper	<1 %
11	epdf.pub Internet Source	<1 %
12	Submitted to Oakham School Student Paper	<1 %
13	Bong Wie. "Space Vehicle Dynamics and Control, Second Edition", American Institute of Aeronautics and Astronautics (AIAA), 2008 Publication	<1 %
14	"ICD-10: Internationale statistische Klassifikation der Krankheiten und verwandter Gesundheitsprobleme. 10. Revision", Springer Science and Business Media LLC, 1994 Publication	<1 %
15	mit-ocw.eng.chula.ac.th Internet Source	<1 %
16	aerosrv.atl.calpoly.edu Internet Source	<1 %
17	docplayer.net Internet Source	

		<1 %
18	dspace.mist.ac.bd:8080 Internet Source	<1 %
19	scholarsarchive.byu.edu Internet Source	<1 %
20	ux1.math.us.edu.pl Internet Source	<1 %
21	www.ece.virginia.edu Internet Source	<1 %
22	Allerton. "Aircraft Dynamics", Principles of Flight Simulation Allerton/Principles of Flight Simulation, 10/09/2009 Publication	<1 %
23	Submitted to The University of Manchester Student Paper	<1 %
24	mafiadoc.com Internet Source	<1 %
25	www.docstoc.com Internet Source	<1 %
26	S. Mendez, E. Gibaud, F. Nicoud. "An unstructured solver for simulations of deformable particles in flows at arbitrary Reynolds numbers", Journal of Computational Physics, 2014 Publication	<1 %

27	dokumen.pub Internet Source	<1 %
28	Yusuf Kartal, Patrik Kolaric, Victor Lopez, Atilla Dogan, Frank Lewis. "Backstepping approach for design of PID controller with guaranteed performance for micro-air UAV", Control Theory and Technology, 2019 Publication	<1 %
29	Submitted to Escuela Politecnica Nacional Student Paper	<1 %
30	"German Development of the Swept Wing 1935–1945", American Institute of Aeronautics and Astronautics (AIAA), 2010 Publication	<1 %
31	Submitted to University of Bristol Student Paper	<1 %
32	repositorio.unb.br Internet Source	<1 %
33	scholar.afit.edu Internet Source	<1 %
34	Submitted to Middle East Technical University Student Paper	<1 %
35	open.library.ubc.ca Internet Source	<1 %
36	vtechworks.lib.vt.edu	

	Internet Source	<1%
37	www.spiedigitallibrary.org Internet Source	<1%
38	Submitted to University of Glasgow Student Paper	<1%
39	onlinelibrary.wiley.com Internet Source	<1%
40	www.control.auc.dk Internet Source	<1%
41	Ryo Nakabayashi, Daisuke Sugiyama. "Development of methodology of probabilistic safety assessment for radioactive waste disposal in consideration of epistemic uncertainty and aleatory uncertainty", Journal of Nuclear Science and Technology, 2016 Publication	<1%
42	Submitted to Emirates Aviation College, Aerospace & Academic Studies Student Paper	<1%
43	hires.physics.utah.edu Internet Source	<1%
44	www.cfd-online.com Internet Source	<1%
45	Submitted to Defense University Student Paper	

		<1%
46	diva-portal.org Internet Source	<1%
47	www.econstor.eu Internet Source	<1%
48	Submitted to North West University Student Paper	<1%
49	d-nb.info Internet Source	<1%
50	libris.bahcesehir.edu.tr Internet Source	<1%
51	mdpi-res.com Internet Source	<1%
52	tel.archives-ouvertes.fr Internet Source	<1%
53	www.gradesaver.com Internet Source	<1%
54	etd.lib.metu.edu.tr Internet Source	<1%
55	repository.dl.itc.u-tokyo.ac.jp Internet Source	<1%
56	www.oak.go.kr Internet Source	<1%

57	Xie Haibin, Lin Longxin, Shen Lincheng. "Design and realization of simulation system of bionic underwater vehicle", 2008 27th Chinese Control Conference, 2008 Publication	<1 %
58	digitalcommons.lsu.edu Internet Source	<1 %
59	dspace.lib.cranfield.ac.uk Internet Source	<1 %
60	es.scribd.com Internet Source	<1 %
61	etd.aau.edu.et Internet Source	<1 %
62	id.123dok.com Internet Source	<1 %
63	lup.lub.lu.se Internet Source	<1 %
64	open.uct.ac.za Internet Source	<1 %
65	vdocuments.site Internet Source	<1 %
66	www.scholarpublishing.org Internet Source	<1 %

67	Ana Carpio, Oliver Dorn, Miguel Moscoso, Frank Natterer, George C. Papanicolaou, Maria Luisa Rapún, Alessandro Teta. "Inverse Problems and Imaging", Springer Science and Business Media LLC, 2008 Publication	<1 %
68	Frederick O. Smetana. "Introduction to the Control of Dynamic Systems", American Institute of Aeronautics and Astronautics (AIAA), 1994 Publication	<1 %
69	J.M. Rodrigues, C. Guedes Soares. "Froude-Krylov forces from exact pressure integrations on adaptive panel meshes in a time domain partially nonlinear model for ship motions", Ocean Engineering, 2017 Publication	<1 %
70	etheses.whiterose.ac.uk Internet Source	<1 %
71	lib.unisayogya.ac.id Internet Source	<1 %
72	moam.info Internet Source	<1 %
73	pure.au.dk Internet Source	<1 %
74	purehost.bath.ac.uk Internet Source	

<1 %

75 service.tsi.telecom-paristech.fr
Internet Source <1 %

76 silo.pub
Internet Source <1 %

77 www.dtic.mil
Internet Source <1 %

78 www.ncgeo.nl
Internet Source <1 %

79 Brian Fabien. "Kinematics", Analytical System Dynamics, 2009
Publication <1 %

80 Jack D. Mattingly. "Elements of Propulsion: Gas Turbines and Rockets", American Institute of Aeronautics and Astronautics (AIAA), 2006
Publication <1 %

81 Nesreen Ghaddar, Kamel Ghali, Bassel Jreije. "Ventilation of Wind-Permeable Clothed Cylinder Subject to Periodic Swinging Motion", ASME/JSME 2007 Thermal Engineering Heat Transfer Summer Conference, Volume 1, 2007
Publication <1 %

82 Nina Mahmoudian, Craig Woolsey. "Underwater glider motion control", 2008 47th <1 %

IEEE Conference on Decision and Control, 2008
Publication

83	"Atmospheric and Space Flight Dynamics", Springer Science and Business Media LLC, 2007 Publication	<1 %
84	S. Simani, M. Bonfe. "Modelling and identification of residual generator functions for fault detection and isolation of a small aircraft", 2004 43rd IEEE Conference on Decision and Control (CDC) (IEEE Cat. No.04CH37601), 2004 Publication	<1 %

Exclude quotes	Off	Exclude matches	Off
Exclude bibliography	On		

Curriculum Vitae

	Basic Information
Name	Faisal Tri Mulyawan
Place of Birth	Jakarta
Date of Birth	21 March 1994
Address	Jalan Alam Nirwana no.19, Bandung
Year	Education
2017 - present	International University Liaison Indonesia
2009 - 2012	SMA Pribadi Bilingual Boarding School Bandung
Year	Organizational Experiences
2017 2020	IULI Basketball Club Staff Member
2017 - 2018	Member of AVE Student Association, Academic Division
Year	Work Experiences
2020	Student intern at Pustekroket Lapan
2018	Garuda Maintenance Facility, On-Job-Training